Spin Precession in Spin-Orbit Fields under Wire Confinement and Drift

Inauguraldissertation

zur Erlangung der Würde eines Doktors der Philosophie
vorgelegt der
Philosophisch-Naturwissenschaftlichen Fakultät
der Universität Basel

von
Patrick Altmann
aus Deutschland

Basel 2016

Genehmigt von der Philosophisch-Naturwissenschaftlichen Fakultät auf Antrag von

Prof. Dr. Richard Warburton (Fakultätsverantwortlicher)
Dr. Gian Salis (Dissertationsleiter)
Prof. Dr. Werner Wegscheider (Korreferent)

Basel, den 21.Juni.2016

Prof. Dr. Jörg Schibler
Dekan

Summary

This thesis reports on the effects of wire confinement and drift on the electron spin dynamics in gallium arsenide quantum wells. The spin dynamics in such systems is governed by spin-orbit interaction. The motivation for this work is explained in Chapter 1.

Chapter 2 will provide the reader with background information on semiconductor quantum wells and what role spin-orbit interaction plays in such systems. It will particularly specify the relevant mechanisms that act on spins and introduce sufficient theoretical background for the reader to understand the results presented in the later chapters. The methodology is explained in Chapter 3. Scanning Kerr microscopy as the main experimental technique, as well as methods for data evaluation will be depicted.

Chapter 4 focuses on the impact of wire confinement. Two studies are presented that evaluate measured spin dynamics for increasing wire confinement for two different symmetries of the spin-orbit interaction. The data is compared to theoretical models and we find that wire confinement affects the spin dynamics differently in the two cases. While in one the impact is a suppression of diffusion, in the other it is an enhancement of the spin lifetime by an order of magnitude.

The interplay between drift motion and diffusive motion is the subject of Chapter 5. It is demonstrated that, under drift, quasistationary electrons experience a temporal spin precession in the absence of an external magnetic field. The corresponding frequency scales linearly with the drift velocity. This unexpected finding is explained theoretically as a consequence of nonlinear terms of the spin-orbit interaction, for which drift leads to a spin precession angle twice that of spins that diffuse the same distance. In an outlook section, measurements are presented that show that under certain conditions a higher-order regime is accessible in which the spin precession depends nonlinearly on the drift velocity.

Based on this nonlinear dependence, which is also predicted by a theoretical model, a novel scheme for spin amplification is developed in Chapter 6. The proposed concepts also profit from the findings of Chapter 4.

Zusammenfassung

Diese Dissertationsarbeit beschreibt, wie sich Drahteinengungen und Drift auf die Elektronspindynamik in Gallium Arsenid basierten Quantentrögen auswirken. Diese Spindynamik ist im Allgemeinen von Spinbahnwechselwirkung bestimmt. Die Motivation für diese Arbeit wird in Kapitel 1 dargelegt.

In Kapitel 2 finden sich Hintergrundinformationen über halbleiterbasierte Quantentröge und die Rolle der Spinbahnwechselwirkung in diesen Systemen. Vor allem die relevanten Mechanismen, die sich auf Elektronenspins auswirken, werden eingeführt, sowie eine ausreichende theoretische Grundlage aufgebaut, so dass dem Leser die Ergebnisse in den darauffolgenden Kapiteln verständlich werden. Die Methodik wird in Kapitel 3 beschrieben. Neben Raster-Kerr-Mikroskopie als Hauptmesstechnik werden Methoden zur Datenauswertung dargelegt.

Kapitel 4 beschäftigt sich mit dem Einfluss von Drahteinengung. Zwei Studien werden vorgestellt, die die Auswirkung von zunehmender Drahteinengung auf die Spindynamik für zwei verschiedene Symmetrien der Spin-Bahn Wechselwirkung messen. Die Ergebnisse werden mit theoretischen Modellen verglichen. In dem einen Fall führt sie zu einer Unterdrückung von diffusiver Ausdünnung und in dem anderen Fall führt sie zu einem Anstieg der Spinlebenszeit von einer Grössenordnung.

Das Zusammenspiel von Drift und diffusiver Bewegung ist das Thema in Kapitel 5. Es wird gezeigt, dass quasistationäre Elektronen unter Drift in Abwesenheit eines externen Magnetfelds eine zeitliche Spinpräzessionsfrequenz aufweisen. Die entsprechende Frequenz hängt linear von der Driftgeschwindigkeit ab. Dieser nicht vorhergesagte Befund wird durch ein theoretisches Model als eine Konsequenz von nichtlinearen Termen der Spinbahnwechselwirkung identifiziert. Weitere Messungen demonstrieren, dass unter bestimmten Vorraussetzungen ein Regime zugänglich ist, in dem die Präzessionsfrequenz nichtlinear von der Driftgeschwindigkeit abhängt.

Basierend auf dieser nichtlinearen Abhängigkeit, die weiter auch von einem theoretischen Modell vorhergesagt wird, werden in Kapitel 6 neuartige Konzepte zur Spinverstärkung entwickelt. Die vorgestellten Entwürfe profitieren auch von den Erkenntnissen aus Kapitel 4.

Contents

Symbol/Abbreviation	Explanation
SOI	spin-orbit interaction
$\mathbf{k}$	electron momentum wave vector
E_F	Fermi energy
k_B	Boltzmann constant
T	temperature
$\hbar$	reduced Planck constant
x, y, z	three orthogonal spatial directions
m^*	effective electron mass
k_F	Fermi wave vector, $k_\mathrm{F} = \sqrt{2m^*E_\mathrm{F}}/\hbar$
n_s	electron sheet density
g	electron g-factor
μ_B	Bohr magneton
$\boldsymbol{\sigma} = (\sigma_x, \sigma_y, \sigma_z)$	vector of Pauli matrices
γ	bulk Dresselhaus parameter
α	Rashba parameter
β_1, β_3	linear and cubic Dresselhaus parameter in a quantum well
θ	angle in the xy plane with the respect to the x axis
$\mathbf{B}_\mathrm{SO}$	effective spin-orbit magnetic field
μ	electron mobility
q	spatial spin precession wavenumber
ω	temporal spin precession frequency
l_SO	spin-orbit length
D_s	spin diffusion constant
τ_DP	Dyakonov-Perel spin dephasing time
τ_2D	spin dephasing time of a two-dimensional intrinsic precession pattern in the isotropic limit
PSH	persistent spin helix
τ_PSH	spin dephasing time of a PSH
τ_0	minimum decay rate of a spin mode
q_0	wavenumber for which the decay rate of a spin mode is minimal
σ_0	σ-width of the convolved Gaussian intensity profiles of pump and probe spots
J_0	zeroth order Bessel function
1D, 2D	one-dimensional, two-dimensional
w	width of the wire
v_dr	drift velocity
k_dr	drift wave vector
k_di	diffusion wave vector

List of abbreviations and symbols

Chapter 1

Motivation

Spin-orbit interaction (SOI) is a relativistic effect that has many important consequences for solid state physics and atomic physics in general, and for specific concepts like the spin Hall effect, the quantum Hall effect, valleytronics and topological insulators in particular. In III-V semiconductors, like GaAs, the SOI is especially interesting because those crystals lack inversion symmetry. This gives rise to the so-called Dresselhaus SOI. In quantum well structures, electrons are confined in a two-dimensional (2D) layer and have high mobility and conductivity. In such quantum wells, another kind of SOI, namely the so-called Rashba SOI arises. The interplay of Dresselhaus and Rashba SOI is one focus of this thesis. We will look at systems with either only Dresselhaus SOI or with equal Rashba and Dresselhaus SOI in different kinds of experiments. We will see that the spin dynamics strongly depends on the anisotropy of the SOI. The main purpose of this work is to investigate the impact of wire confinement and to study the interplay of drift transport and diffusive transport on the electron spin dynamics.

Closely related to SOI is the concept of semiconductor spintronics. Spintronics is a neologism that stems from the words spin and electronics. This expresses the intention to use the spin of electrons in addition to or instead of their charge for applications that are performed by electronic devices. This field of research has seen a lot of activity into various directions from the late 1990s on. But until today, semiconductor spintronics, in contrast to its metal counterpart, has not, yet, had its breakthrough into commercial applications. The main hurdles that still remain are spin dephasing and the lack of spin amplification. Both points will be addressed in this thesis.

While wire confinement is shown to suppress spin decay, drift of diffusive electrons in nonlinear spin-orbit fields is identified as a novel approach for spin manipulation. Based on both findings, a new concept for spin amplification is developed.

Chapter 2

Physical Fundamentals

The work in this thesis focuses on 2D electron gases in remotely-doped (001)-oriented GaAs/AlGaAs quantum wells. In this chapter, we shall explain why this system is the most interesting one for our purpose and we shall give sufficient understanding of the material system such that the results in Chapters 4, 5 and 6 are comprehensible.

2.1 Semiconductor quantum wells and spin-orbit interaction

While SOI is a phenomenon that plays an important role in almost every solid state system, III-V semiconductors represent certainly a class of crystals that is particularly interesting in this respect. A lack of inversion symmetry of the crystal structure leads to the so-called Dresselhaus SOI [1]. Particularly the interplay between Dresselhaus and Rashba SOI [2, 3] opens up a big field and is of central importance to the studies presented in Chapters 4 and 5. This Rashba SOI arises from structural inversion asymmetry as it is easily realized in quantum wells. By design of such a quantum well structure, the strength of both the Dresselhaus and the Rashba SOI can be tuned. The choice of GaAs instead of another III-V semiconductor is not only because the size of its bandgap is perfectly suited for the convenient use of Ti:Sapphire lasers (see Chapter 3). It is also because the similarity of the lattice constants of GaAs and AlGaAs minimizes strain in the quantum well [4]. A suppression of strain is favorable not only because this facilitates growth, but also because strain would cause additional spin-orbit effects [5] that we prefer to exclude. Grown by molecular beam epitaxy with atomic precision by the Wegscheider group at ETHZ, the ultra-clean semiconductor heterostructures enabled this work. In the following, we will focus on crystals that are grown along the [001]-crystallographic direction. This is because the Dresselhaus and Rashba fields then lye in the quantum-well plane which on the one hand

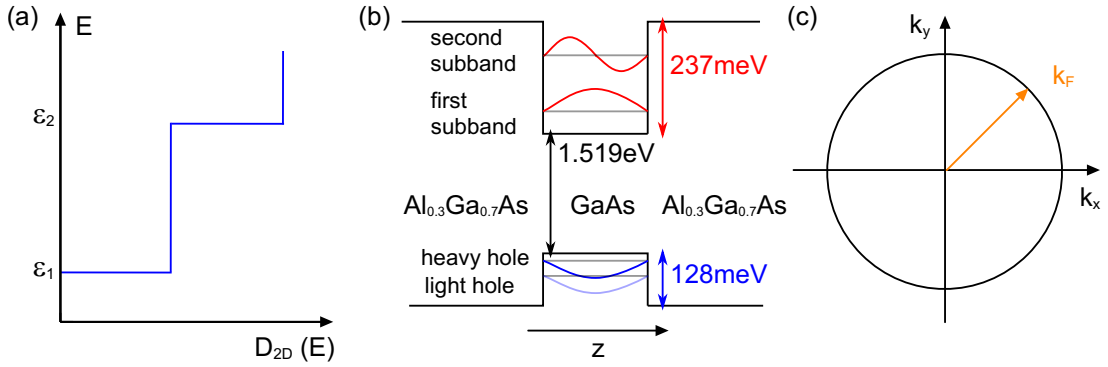

Figure 2.1: (a) Density of states for a 2D system. (b) Schematic energy diagram of a quantum well structure realized in GaAs/$Al_{0.3}Ga_{0.7}As$ with the most important energy values. (c) Sketch of the Fermi circle of a quantum well, where z is the growth axis. In the degenerate limit ($k_BT \ll E_F$), all relevant electrons are at the Fermi energy.

enables the persistent spin helix state (Section 2.3.2) and on the other hand is perfectly suited for the use of Kerr microscopy (Section 3.2).

General properties of a two-dimensional electron gas

A quantum well is formed, for instance, by a layer of GaAs sandwiched between AlGaAs [Fig. 2.1(b)]. Because of the different sizes of the bandgap and the type-I alignment of conduction and valence band [6], there is a confinement potential both for electrons and holes. In the following, we want to understand the particularities of this arrangement in terms of the electronic properties.

While electrons in a quantum well structure can freely move in the xy-plane, confinement along the $z \,||\, [001]$ direction restricts the kinetic energy for motion along z to the so-called subband energies, ϵ_n, where n is a positive integer. The total energy of an electron in a quantum well, given its effective mass m^* and its wave vector $\mathbf{k}$ is therefore

$$E_n(k_x, k_y) = \frac{\hbar^2 k_x^2}{2m^*} + \frac{\hbar^2 k_y^2}{2m^*} + \epsilon_n \,. \tag{2.1}$$

The reduced Planck constant is denoted by $\hbar$. The density of states for each subband is $D_{2D} = m^*/(\pi\hbar^2)$ [Fig. 2.1(a)]. In the degenerate limit ($E_F > k_BT$), all relevant electrons are those at the Fermi energy, denoted by E_F. In the following, we will assume one occupied subband, i.e. that $\epsilon_1 < E_F < \epsilon_2$.

Because of quantization along z, a useful representation of a degenerate 2D electron gas is given by the Fermi circle as sketched in Fig. 2.1(c). While the electrons are free to move in the xy-plane, all have the same size of the momentum vector defined by $k_x^2 + k_y^2 = k_F^2$, $k_F = \sqrt{\frac{2m^* E_F}{\hbar^2}}$ being the Fermi momentum vector

(zero temperature limit). In case of one occupied subband, the number of electrons per area is given by $n_\mathrm{s} = D_\mathrm{2D} E_\mathrm{F}$. This leads to the following relation, which will be used frequently in Chapters 4 to 6,

$$k_\mathrm{F} = \sqrt{2\pi n_\mathrm{s}}\,. \tag{2.2}$$

Spin-orbit interaction

SOI is a fundamental relativistic effect [7], which translates an electric field ($\mathbf{E}$) into an effective magnetic field ($\mathbf{B}_\mathrm{eff}$) from the point of view of a reference frame moving with velocity v. This connection was already described before the introduction of relativity by Lorentz [8].

$$\mathbf{B}_\mathrm{eff} = -\frac{1}{c^2\sqrt{1-v^2/c^2}}\,\mathbf{v}\times\mathbf{E} \tag{2.3}$$

The letter c denotes the speed of light. From this equation and $H = g\mu_\mathrm{B}\mathbf{B}\cdot\boldsymbol{\sigma}/2$ it follows under the assumption that $v \ll c$ and for an electron g-factor $g = 1$, that

$$H_\mathrm{SO}^\mathrm{Pauli} = -\frac{\hbar^2}{4m_0^2c^2}\boldsymbol{\sigma}\cdot(\nabla V_0)\times\mathbf{k}\,, \tag{2.4}$$

where V_0 is the effective Coulomb potential of the crystal, m_0 is the bare electron mass and $\boldsymbol{\sigma} = (\sigma_x, \sigma_y, \sigma_z)$ is the vector of Pauli matrices with

$$\sigma_x = \begin{pmatrix} 0 & 1 \\ 1 & 0 \end{pmatrix},\ \sigma_y = \begin{pmatrix} 0 & -i \\ i & 0 \end{pmatrix},\ \sigma_z = \begin{pmatrix} 1 & 0 \\ 0 & -1 \end{pmatrix}. \tag{2.5}$$

Equation (2.4) is referred to as the Pauli spin-orbit term. It is used to incorporate SOI into $k\cdot p$ calculations of the band structure of semiconductors [9]. Dresselhaus considered this term when he derived the SOI in zinc blende crystals [1], where SOI arises from inversion asymmetry of the crystal structure. The strength of this interaction scales with the bulk Dresselhaus parameter γ and is, for $x\|\|[100]$ and $y\|\|[010]$, given by

$$H_\mathrm{D}^\mathrm{bulk} = \gamma\left[\sigma_x k_x(k_y^2-k_z^2) + \sigma_y k_y(k_z^2-k_x^2) + \sigma_z k_z(k_x^2-k_y^2)\right]. \tag{2.6}$$

This kind of interaction is absent in crystals with inversion symmetry like Si or Ge, which have diamond structure. But also there, structural inversion asymmetry, present in 2D systems, leads to SOI scaling with the Rashba parameter α [2, 3].

$$H_\mathrm{R}^\mathrm{2D} = \alpha(k_y\sigma_x - k_x\sigma_y) \tag{2.7}$$

A quantum well, as described earlier in this section, is such a 2D system. The size of α is a measure for the electric field that drops along the growth axis of the

quantum well and can either be positive or negative depending on the orientation of the field with respect to the positive z axis [10]. It can be designed by the doping profile or tuned via an electric gate [11].

For a (001)-oriented quantum well, the Dresselhaus SOI is obtained from Eq. (2.6) by replacing k_z by $\langle k_z \rangle = 0$ and k_z^2 by the expectation value $\langle k_z^2 \rangle$.

$$H_{\mathrm{D}}^{\mathrm{2D}} = -\gamma \langle k_z^2 \rangle (k_x \sigma_x - k_y \sigma_y) - \gamma \left(k_y^2 k_x \sigma_x - k_x^2 k_y \sigma_y \right) \tag{2.8}$$

We see that the Dresselhaus SOI in a quantum well splits up into a term that is linearly proportional to k and one that is proportional to k^3. The role of the latter becomes clearer when one writes Eq. (2.8) in spherical coordinates, i.e. $(k_x, k_y) = (k \cos\theta, k \sin\theta)$ [12, 13].

$$\begin{aligned} H_{\mathrm{D}}^{\mathrm{2D}} =& -\gamma \langle k_z^2 \rangle k (\sigma_x \cos\theta - \sigma_y \sin\theta) \\ &+ \frac{\gamma k^2}{4} k (\sigma_x \cos\theta - \sigma_y \sin\theta) - \frac{\gamma k^2}{4} k (\sigma_x \cos 3\theta - \sigma_y \sin 3\theta) \\ =& \beta^* k (\sigma_x \cos\theta - \sigma_y \sin\theta) + \beta_3 k (\sigma_x \cos 3\theta - \sigma_y \sin 3\theta) \end{aligned} \tag{2.9}$$

Here, we defined the linear Dresselhaus parameter $\beta_1 = -\gamma \langle k_z^2 \rangle$ and the cubic Dresselhaus parameter $\beta_3 = -\gamma k^2/4$. Because the bulk Dresselhaus parameter γ has the unit eV m^3, the unit of α, β_1 and β_3 is eV m. The magnitude of β_1 is mainly defined by the width of the quantum well because this defines $\langle k_z^2 \rangle$. The strength of β_3 instead depends on the size of k. For a degenerate 2D electron gas $k = k_{\mathrm{F}}$ and β_3 might be tuned via the electron sheet density [see Eq. (2.2)]. Because the value of γ is negative, β_1 and β_3, other than α, are always positive.

From Eq. (2.9), we see that the cubic Dresselhaus SOI splits into two terms. One has the same symmetry as the linear Dresselhaus SOI which motivates the introduction of $\beta^* = \beta_1 - \beta_3$. The other term introduces a spherical dependence of 3θ. A major part of Chapters 4, 5 and 6 is about disentangling and understanding in which different ways those terms harmonic in θ and those harmonic in 3θ act on the spin dynamics.

As we will see in Section 2.3, the superposition of Rashba and Dresselhaus spin-orbit fields causes an anisotropy of the strength of the SOI with respect to the electron k vector. For positive α, the interaction is strongest for k along the [110] direction and for negative α along the $[1\bar{1}0]$ direction. The preferred coordinate system for such a case is, thus, defined by $x||[1\bar{1}0]$, $y||[110]$. The expression for the full spin-orbit Hamiltonian in this rotated coordinate system reads

$$H_{\mathrm{SO}}^{\mathrm{2D}} = \alpha(\sigma_x k_y - \sigma_y k_x) + \beta_1(\sigma_y k_x + \sigma_x k_y) + 2\beta_3 \left(k_y \frac{k_x^2 - k_y^2}{k^2}\sigma_x + k_x \frac{k_y^2 - k_x^2}{k^2}\sigma_y \right) . \tag{2.10}$$

By comparing $H_{\mathrm{SO}} = {}^1\!/_2\, g\mu_B \boldsymbol{\sigma} \cdot \boldsymbol{B}_{\mathrm{SO}}$ [14] with Eq. (2.10), one can see that the way SOI acts on the spin is like an effective magnetic field

$$\mathbf{B}_{\mathrm{SO}}(\mathbf{k}) = \frac{2}{g\mu_B} \begin{pmatrix} \left[\alpha + \beta_1 + 2\beta_3 \frac{(k_x^2 - k_y^2)}{k^2}\right] k_y \\ \left[-\alpha + \beta_1 + 2\beta_3 \frac{(k_y^2 - k_x^2)}{k^2}\right] k_x \end{pmatrix} , \tag{2.11}$$

where g is the electron g-factor and μ_B is the Bohr magneton. With this expression, we have closed the loop of the discussion of SOI back to Eq. (2.3).

By rewriting Eq. (2.11) in spherical coordinates, we obtain $\mathbf{B}_{\mathrm{SO}} = \mathbf{B}_{\mathrm{SO}}^{(1)} + \mathbf{B}_{\mathrm{SO}}^{(3)}$ [15, 12, 13] with

$$\mathbf{B}_{\mathrm{SO}}^{(1)}(\mathbf{k}) = \frac{2k}{g\mu_B} \begin{pmatrix} [\alpha + \beta^*] \sin\theta \\ [-\alpha + \beta^*] \cos\theta \end{pmatrix} , \tag{2.12}$$

and

$$\mathbf{B}_{\mathrm{SO}}^{(3)}(\mathbf{k}) = \frac{2k}{g\mu_B} \begin{pmatrix} \beta_3 \sin 3\theta \\ -\beta_3 \cos 3\theta \end{pmatrix} , \tag{2.13}$$

with θ being the angle between $\mathbf{k}$ and $x||[1\bar{1}0]$. As explained in the following sections, $\mathbf{B}_{\mathrm{SO}}^{(1)}$ defines the intrinsic precession pattern while $\mathbf{B}_{\mathrm{SO}}^{(3)}$ is mainly responsible for spin dephasing. In Chapter 4 we will demonstrate that wire confinement suppresses spin dephasing due to $\mathbf{B}_{\mathrm{SO}}^{(1)}$, but not the one due to $\mathbf{B}_{\mathrm{SO}}^{(3)}$. But cubic SOI not only has detrimental effects, as we will see in Chapter 5, where it is responsible for the surprising current-induced spin precession of quasistationary electrons.

It is intuitive to imagine the impact of SOI on spins as effective magnetic fields. It is important to notice that these fields depend on the k-vector. In the previous section, we learned that in the degenerate limit, a 2D electron gas is described by the Fermi circle (see Fig. 2.1). This gives us the possibility to visualize the different contributions of the Rashba and linear and cubic Dresselhaus terms. In Fig. 2.2, we plot these fields schematically for a (001)-grown quantum well according to Eqs. (2.12) and (2.13) for a negative g-factor. The precession of spins about these spin-orbit fields is a semi-classical picture that is sufficient to describe and calculate the different regimes of spin dynamics that we will study in this thesis.

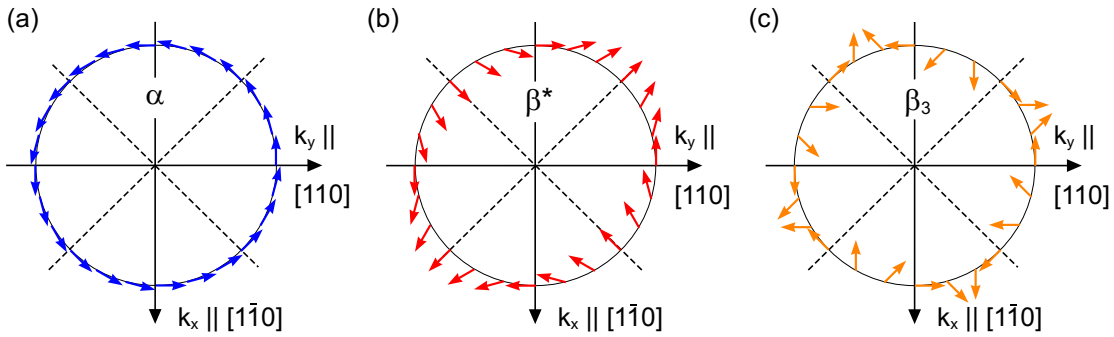

Figure 2.2: Spin-orbit fields according to Eqs. 2.12 and 2.13 visualized on the Fermi circle of a degenerate 2D electron gas for a negative g-factor. (a) Rashba field assuming $\alpha > 0$. The field is isotropic because the magnitude is the same for every k vector. But the direction of the spin-orbit field is different for every k vector. (b) Linear Dresselhaus field proportional to the reduced Dresselhaus parameter $\beta^* = \beta_1 - \beta_3$. Also this field is isotropic. (c) Part of the cubic Dresselhaus field according to Eq. 2.13. Because of the 3θ dependence, the vector of the spin-orbit field rotates three times faster than for the linear Dresselhaus field.

2.2 Spin diffusion and spin dephasing

For sufficiently low temperatures ($k_B T \ll E_F$), it can be assumed that all relevant electrons in a 2D electron gas have the wave vector k_F [Fig. 2.1(c)].[1] Although the direction of motion within the quantum well plane is free, the velocity is the same for every electron. Because of SOI, as we have learned in the previous section, an electron in a given k-state experiences an effective magnetic field. The spin $\mathbf{s}$ of the electron will precess about this field following

$$\frac{\mathrm{d}\mathbf{s}}{\mathrm{d}t} = \frac{g\mu_B}{\hbar}\mathbf{s} \times \mathbf{B}_{\mathrm{SO}}(\mathbf{k})\,. \tag{2.14}$$

At this step, we want to point out an important conceptual difference between spin precession in $\mathbf{B}_{\mathrm{SO}}$ and in an external magnetic field $\mathbf{B}_{\mathrm{ext}}$. In the following example, we assume a spin oriented out-of-plane that is perpendicular to the magnetic field. While for an external magnetic field, the precession phase acquired by a spin solely depends on the time it spends in this magnetic field ($\phi = \frac{g\mu_B}{\hbar} B_{\mathrm{ext}} t$), for B_{SO} because of its k dependence [Eqs. (2.12) and (2.13)] we obtain the following relation.

[1] If the Fermi gas is subjected to drift, this statement is no longer true. We will consider this case in Chapter 5.

$$\begin{aligned}\phi &= \frac{g\mu_B}{\hbar} B_{\mathrm{SO}} t \\ &= \frac{2kt}{\hbar}\left[\begin{pmatrix}[\alpha+\beta^*]\sin\theta\\ [-\alpha+\beta^*]\cos\theta\end{pmatrix} + \begin{pmatrix}\beta_3\sin 3\theta\\ \beta_3\cos 3\theta\end{pmatrix}\right] \\ &= \frac{2m}{\hbar^2} vt\left[\begin{pmatrix}[\alpha+\beta^*]\sin\theta\\ [-\alpha+\beta^*]\cos\theta\end{pmatrix} + \begin{pmatrix}\beta_3\sin 3\theta\\ \beta_3\cos 3\theta\end{pmatrix}\right] \\ &= \frac{2m}{\hbar^2}\Delta r\left[\begin{pmatrix}[\alpha+\beta^*]\sin\theta\\ [-\alpha+\beta^*]\cos\theta\end{pmatrix} + \begin{pmatrix}\beta_3\sin 3\theta\\ \beta_3\cos 3\theta\end{pmatrix}\right] \propto \Delta r \end{aligned} \tag{2.15}$$

Here we used $k = mv/\hbar$. This is a very important result because it shows that the precession angle acquired in a spin-orbit field, rather than on the time passed, depends on Δr, the distance traveled. We can express the out-of-plane component of a spin for an electron with a defined k vector as $\cos(qr + \omega t)$. From Eq. (2.15), we see that SOI leads to a finite spatial precession vector q, but not to a temporal precession frequency ω. This is in contrast to the effect of an external magnetic field, which leads to a finite $\omega = g\mu_{\mathrm{B}} B_{\mathrm{ext}}/\hbar$ with $q = 0$. This difference has already been observed in one of the first spatially resolved transient spin measurements [5, 16]. We will come back to this point for the discussion of Eq. (2.23). The spin-orbit length is defined by $l_{\mathrm{SO}} = 2\pi/q$ and denotes the distance an electron needs to travel for a 2π rotation of its spin. Above discussion holds for the ballistic (no scattering) and degenerate limit. The impact of scattering is considered in the following.

Introduction to diffusion

The discussion until now only holds for ballistic systems. Now we want to look at diffusive systems, i.e. systems in which the electrons experience scattering. The transport mobility of quantum wells as they are studied in this thesis is limited by phonon scattering at temperatures above 100 K and by background impurity scattering at temperatures below 100 K [6]. We will work in a range from 10 to 40 K. The relevant mechanism for spin diffusion is electron-electron scattering as will be explained in the following paragraph.

It is very common to determine the diffusion constant from a measurement of the mobility μ of the 2D electron gas. The momentum relaxation time τ_p is the time between two scattering events and is related to the mobility via $\tau_p = m^*\mu/e$ (Drude model) [6]. The diffusion constant is then obtained via the Einstein relation at low temperatures by $D = v^2\tau_p/2$ where v, in the degenerate limit, is equal to the Fermi velocity [6]. The spin diffusion constant D_{s} is sensitive to electron-electron scattering [17, 18]. In a transport measurement, one is insensitive to

electron-electron scattering [17, 18]. If electron-electron scattering is the dominant scattering mechanism, it is, thus, false to calculate the spin diffusion constant from the transport mobility. The impact of electron-electron scattering on spin transport was first described by the so-called spin Coulomb drag [19, 20], which interprets the impact of Coulomb scattering among electrons of opposite spins as a frictional force. This friction results in a spin diffusion constant which is reduced compared to the charge diffusion constant. The spin diffusion constants we determine in Chapters 4 and 5 are even smaller than what is anticipated by spin Coulomb drag (see, for instance, Eq. (1) in Ref. [20]). This has been found by several research groups and Yang et al. have argued that the Spin Coulomb Drag formalism does not hold anymore once the temperature is higher than the Fermi temperature [21]. In fact, the sample temperature in the studies presented in the following chapters never exceeds the Fermi temperature and it is an open question if electron-electron scattering alone is sufficient to explain the low spin diffusion constant.

How does spin-orbit interaction lead to spin dephasing?

We will restrict the discussion to systems where the mean-free path $l_{\mathrm{mfp}} \ll l_{\mathrm{SO}}$. This is commonly referred to as the weak SOI regime. After each scattering event, an electron has a new k vector and its spin sees a different $\mathbf{B}_{\mathrm{SO}}(\mathbf{k})$. Because the sequence of k vectors is random in a diffusive system, each electron spin in a 2D electron gas precesses about a random sequence of precession axes. Dyakonov and Perel were the first to point out that this can lead to spin dephasing [22]. They calculated the spin dephasing time τ_{DP} for a homogeneous out-of-plane spin excitation without spatial correlations. In a (001)-oriented quantum well as described above, it is given by

$$\tau_{\mathrm{DP}}^{-1} = 8\frac{D_s m^{*2}}{\hbar^4}\left(\alpha^2 + \beta^{*2} + \beta_3^2\right) \ . \tag{2.16}$$

Expressions for the dephasing rates of in-plane spins are given in Ref. [14]. Other decay mechanisms for a spin polarization exist [13, 23, 24], but none of them is relevant for the studies presented in this thesis.[2]

After the presentation of the first spatially resolved Kerr measurements [25], it became evident that the spin dynamics of a local spin excitation is different from that of a homogeneous spin excitation. Particularly, the dephasing time is enhanced.

If spatial correlations between the electrons are considered, the Dyakonov-Perel formalism is no longer valid and spin dephasing occurs via the following

[2] This statement is justified, for instance, by the good agreement between the measured spin dephasing times and the expected theoretical values in Fig. 4.3(c).

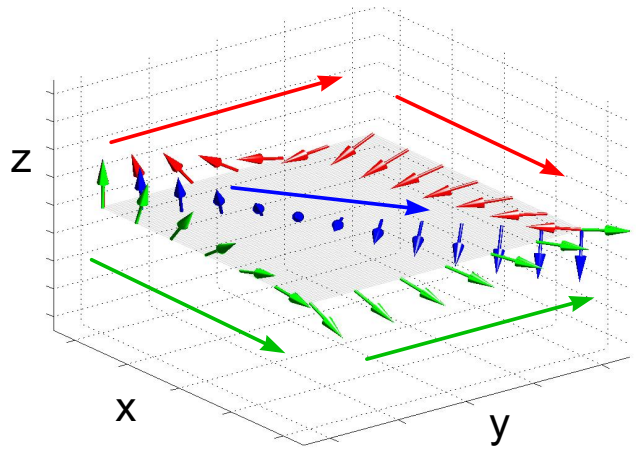

Figure 2.3: Sketch of the trajectories and corresponding spin precession of three different spins in a linear Dresselhaus spin-orbit field. We see that, when all three reunite in the right corner after taking different trajectories, their spins point into different directions. More explanation is found in the main text.

mechanism. In Fig. 2.3, we show the spin precession of three electrons (coded in red, blue and green color) in a linear Dresselhaus field. All spins start in the left corner and are oriented along z. The electrons take different paths. The red spin reaches the right corner via the upper corner and the green spin goes via the lower corner. The blue one takes a straight path and is thus our ballistic reference. The first thing that becomes obvious is that the orientation of all three spins is different once they reunite in the right corner. This is because on their trajectories, they precess about the spin-orbit fields defined by their k vectors. Once the direction of motion changes (change of k vector after a scattering event), the precession axis changes, too. It is interesting to note that the red and green trajectories in Fig. 2.3 are described by the same k vectors, just in reversed order. The spin-orbit fields about which the spins precess are hence also the same. But rotations about different precession axes do not commute and this is the main cause for spin dephasing in spatially resolved diffusive spin-orbit coupled systems.

2.3 What are spin modes?

In an experiment, instead of a single electron, we typically measure a time-dependent spin density in space $\boldsymbol{\rho}(\mathbf{r}, t)$. In the following, we describe mathematically how a local spin excitation evolves, if electrons spread diffusively and their spin dynamics is governed by the effective magnetic field of Eq. (2.11). We will always assume to be in the weak SOI limit, i.e. in the limit that spins only rotate small angles between two scattering events ($\Omega\,\tau_p \ll 1, \Omega = g\mu_\mathrm{B}B_\mathrm{SO}/\hbar$). It is advantageous to

evaluate spin precession in Fourier space [26, 27, 23, 28, 29]. The following spin diffusion equation can be derived by standard perturbation theory [30, 27, 23] or from a semiclassical spin kinetic equation [13]:

$$\left[-i\omega + D_\mathrm{s}(q_x^2 + q_y^2 + q_0^2\tilde{\mathbf{D}})\right]\hat{\boldsymbol{\rho}} = 0\,, \tag{2.17}$$

where $q_0 = \frac{2m^*}{\hbar^2}(\alpha+\beta^*)$. The impact of SOI on the spin dynamics is encoded in the matrix $\tilde{\mathbf{D}}$, where we neglect spin-charge coupling and use the parameters $r_1 = (\alpha-\beta^*)/(\alpha+\beta^*)$ and $r_2 = \beta_3/(\alpha+\beta^*)$ [31].

$$\tilde{\mathbf{D}} = \begin{pmatrix} r_1^2 + r_2^2 & 0 & -ir_1\frac{2q_x}{q_0} \\ 0 & 1+r_2^2 & -i\frac{2q_y}{q_0} \\ ir_1\frac{2q_x}{q_0} & i\frac{2q_y}{q_0} & 1+r_1^2+2r_2^2 \end{pmatrix} \tag{2.18}$$

This equation is based on the $x||[1\bar{1}0]$, $y||[110]$ coordinate system. The diagonal elements of this matrix yield the Dyakonov-Perel dephasing rates. The nondiagonal terms arise from correlations between the momentum and the spin-orbit field and drive the spin modes.

By determining the eigenvectors $\hat{\boldsymbol{\rho}}_n(q_x, q_y)$ and eigenvalues λ_n of $\tilde{\mathbf{D}}$, one obtains for each pair (q_x, q_y) three spin modes $n = 1, 2, 3$ that solve Eq. (2.17)

$$\hat{\boldsymbol{\rho}}_n(q_x, q_y)\exp\left(-i\omega_n t + iq_x x + iq_y y\right)\,,$$

and that decay exponentially with a rate

$$i\omega_n = D_\mathrm{s}(q_x^2 + q_y^2 + q_0^2\lambda_n)\,. \tag{2.19}$$

The time evolution of an arbitrary spin polarization $\boldsymbol{\rho}(x, y, t)$ in real space can then be expressed in terms of these spin modes by using the Fourier integral

$$\boldsymbol{\rho}(x,y,t) = \int_{-\infty}^{\infty}\int_{-\infty}^{\infty}\sum_{n=1}^{3} a_n\hat{\boldsymbol{\rho}}_n\exp\left(-i\omega_n t + iq_x x + iq_y y\right)\mathrm{d}q_x\mathrm{d}q_y\,. \tag{2.20}$$

Here, $a_n(q_x, q_y)$ are the amplitudes of the excited eigenmodes. In the following, we want to describe the real-space evolution of a local spin excitation for certain symmetry points of the SOI in a (001)-oriented quantum well. For a δ-shaped spin excitation in real space, all values of q are equally excited. Solving the spin diffusion equation under this assumption and performing the transformation of Eq. (2.20), $\boldsymbol{\rho}(x, y, t)$ is the Green's function of the spin diffusion equation. We refer to this as the intrinsic spin pattern, because this precession pattern is directly related to the three spin modes.

2.3.1 Bessel function in an isotropic case

We speak of isotropic SOI if the strength of the effective magnetic field is equal at every k vector on the Fermi circle. This is the case for only Rashba or only linear Dresselhaus SOI. In Chapter 4, we will deal with a system that is close to the latter case. Because of the radial symmetry of the SOI, also the intrinsic precession pattern is radially symmetric and depends on $r = \sqrt{x^2 + y^2}$. For vanishing Rashba SOI and considering terms of the cubic Dresselhaus SOI up to an order of β_3^2 ($\beta_3 < \beta^*$), the z component of a δ-peak spin excitation evolves like [26, 27, 32]

$$S_z(t,r) = \frac{A_0}{\sqrt{t}}\,\mathbf{J}_0\left[\sqrt{\frac{15}{16}}\frac{2m^*}{\hbar^2}\beta^*\left(1-\frac{\beta_3^2}{15\beta^{*2}}\right)r\right]\exp\left(\frac{-t}{\tau_{2\mathrm{D}}}\right), \tag{2.21}$$

where A_0 is an amplitude factor, $\mathbf{J}_0$ is the zeroth order Bessel function and

$$\tau_{2\mathrm{D}}^{-1} = 8\frac{D_\mathrm{s}m^{*2}}{\hbar^4}\left[\frac{7}{32}\beta^{*2}+\frac{11}{16}\beta_3^2\right]. \tag{2.22}$$

Above equations hold in the limit $t/\tau_{2\mathrm{D}} \gg r/l_{\mathrm{SO}}$, i.e. at later times and not too far from the point of excitation. Because of the limit of long times, the decay rate is dominated by the global minimum of the mode spectrum of Eq. (2.19). It is important to realize that $\tau_{2\mathrm{D}}$ is enhanced compared to τ_{DP} [Eq. (2.16)]. For only linear Dresselhaus SOI, the spin dephasing time is enhanced by 32/7. Interestingly, the nonexponential decay term in Eq. (2.21) shows a $t^{-1/2}$ behavior, although in two dimensions the diffusive dilution of the spin carrying electrons goes with t^{-1}. Equation (2.21) further shows that, although we imagine SOI as effective magnetic fields, these fields do not lead to a precession in time but in space.

2.3.2 Spin helix at $|\alpha| = |\beta^*|$

At $|\alpha| = |\beta_1|$ and $\beta_3 = 0$, the symmetry of the spin-orbit fields is special. Figure 2.4 shows the superposition of Rashba and Dresselhaus field to a uniaxial spin-orbit field. In this example, $\alpha > 0$. For all states on the Fermi circle $\mathbf{B}_{\mathrm{PSH}} || \hat{x}$ and $B_{\mathrm{PSH}} \propto k_y$.[3] The intrinsic spin pattern for such a case is referred to as the persistent spin helix (PSH) because it is described by an infinite spin lifetime (excluding other decay mechanisms) and a helical rotation of the spins in the y-z plane [33, 34, 35, 36, 37]. If $\beta_3 > 0$, the spin helix condition is met at $|\alpha| = |\beta^*|$ and the spin lifetime is finite.

The dynamics of a δ-peak spin excitation close to the PSH regime is described by [31]

[3] The roles of x and y are reversed if $\alpha = -\beta_1$.

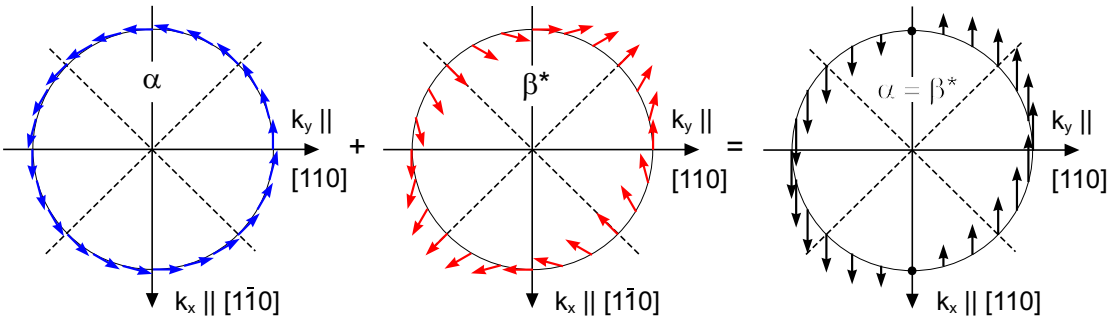

Figure 2.4: The superposition of a Rashba field and a Dresselhaus field of equal strength results in a spin-orbit field which is parallel to x at every k vector (assuming $\alpha > 0$ and $g < 0$). Furthermore, the strength of B_{SOI} is proportional to k_y. Because of this special symmetry, the intrinsic precession pattern of the system is long lived and helical. It is commonly referred to as the persistent spin helix. It is characterized by a strong precession of the spin when the electron moves along y and no precession when moving along x.

$$S_z(y,t) = \frac{A_0}{2D_s t}\cos\left(q_0 y\right)\exp\left(-\frac{y^2}{4D_s t}\right)\exp\left(-\frac{t}{\tau_{\mathrm{PSH}}}\right), \tag{2.23}$$

with

$$\tau_{\mathrm{PSH}}^{-1} = 2D_s\frac{m^{*2}}{\hbar^4}\left[(\alpha-\beta^*)^2 + 3\beta_3^2\right]. \tag{2.24}$$

We are again focusing on the z-component of the spin density. For $\alpha = \beta_1$ and $\beta_3 = 0$, $\tau_{\mathrm{PSH}} \to \infty$.

Via the gate tunability of the Rashba SOI [11], also the PSH state can be tuned [38]. By this it is even possible to switch between the PSH state at $\alpha = \beta^*$ and the inverse PSH state at $\alpha = -\beta^*$ [39]. In a recent experiment, it was shown that, because of its long lifetime, a PSH is well suited for spin transport under drift [40].

Chapter 3

Experimental technique

In this chapter, we want to introduce scanning Kerr microscopy as the method of choice and explain why it is perfectly suited to study SOI in quantum wells by spatially and temporally resolving the spin dynamics. This technique is based on optical orientation to excite spins and Faraday/Kerr rotation to detect spins and we shall first recapitulate the history of these effects.

3.1 Faraday/Kerr rotation and optical orientation

When Michael Faraday conducted the research that should lead to the discovery of what is now known as the Faraday effect he was not looking for a way to measure spin dynamics. It was purely the interest to find the origin of light that propelled his efforts. The question at the time was if light itself has a connection to magnetism and electricity. Faraday's motivation to show such a connection had to withstand a decade of unsuccessful experiments in which he tried to show an effect of a magnetized material onto the polarization of light after reflection from this material. Finally, he found that the axis of polarization of light was rotated after transmission through glass or other transparent material under the application of an external field, the field being parallel the the ray of light. When he published this finding in 1846 [41], he was convinced that this meant nothing less than: *"Thus it is established (...) a true, direct relation and dependence between light and the magnetic and electric forces; and thus a great addition made to the facts and considerations which tend to prove that all natural forces are tied together, and have one common origin."* [41]

The final answer to Faraday's question on the origin of light was given by Maxwell. When the Maxwell equations were presented in 1865 [42], they led to the prediction of electromagnetic waves. According to his calculations, the velocity of those waves is given by $v = {}^{1}/_{\sqrt{\mu_0 \epsilon_0}}$, where μ_0 is the vacuum permeability

and ϵ_0 the vacuum permittivity. The value of $v = 310740000\ \mathrm{m\,s^{-1}}$ had been deduced by Weber and Kohlrausch about ten years earlier [43] from electrostatic and electromagnetic measurements or as Maxwell put it: *"The only use made of light in the experiment was to see the instruments."* [42] Maxwell compared v to the speed of light, the best known value of which at the time was given by the rotating mirror experiment by Foucault [44]. In this experiment, light is sent through an aperture onto a rotating mirror. This mirror deflects the light onto a fixed mirror that in turn reflects back onto the rotating mirror. In the meantime, the mirror has rotated by a certain angle, such that the light is not reflected back to the light source but is registered on the aperture with a slight offset. Foucault determined $c = 298000000\ \mathrm{m\,s^{-1}}$ (only a 0.6 % deviation from today's accepted value). The value of v was so similar to the speed of light, that Maxwell concluded *"that light is an electromagnetic disturbance (...) according to electromagnetic laws"* [42], answering the question, which motivated Faraday's original experiment.

The completion of the reflection experiment for magnetic materials, which Faraday previously failed to realize, was presented by Kerr in 1877 and the observed phenomenon is now known as the magneto-optical Kerr effect [45]. It describes how the polarization of a linearly polarized beam of light is affected after reflection from a magnetized material. One effect is that the polarization axis is rotated and the other is that the polarization becomes slightly elliptic. Obviously the magneto-optical Kerr effect and the Faraday effect are closely related. While for a long time the distinction had been that the Faraday effect refers to diamagnetic materials while the magneto-optical Kerr effect refers to para- or ferromagnetic materials [46], it is now convention to refer to the Faraday effect when looking at transmitted light and to the magneto-optical Kerr effect when working in reflection.

A hundred years after their discovery the focus has moved beyond the sole description of the effects, as becomes clear from a statement by Bennett and Stern [46]: *"[W]e are not only interested in the Faraday effect by itself, but we also are interested in the application of the Faraday effect as a means by which we may acquire further information about solids"*. By the time it became clear that, for non-magnetic materials, the measurement of Faraday rotation under the application of an external magnetic field could be used to study certain aspects of the materials' electronic structure. The 1960s have seen a large number of studies utilizing the Faraday effect to investigate aspects of the bandstructure, such as the electron g-factor [47] and the effective masses [48]. A summary of this early activity is given in Ref. [47] and a summary of the theoretical understanding at the time is given in Ref. [46]. With the same technique, the effects of dopants on the bandstructure were determined in Ge, GaAs, GaSb, InAs, and ZnTe [49]. This kind of activity continued well into the 1990s when a profound understanding

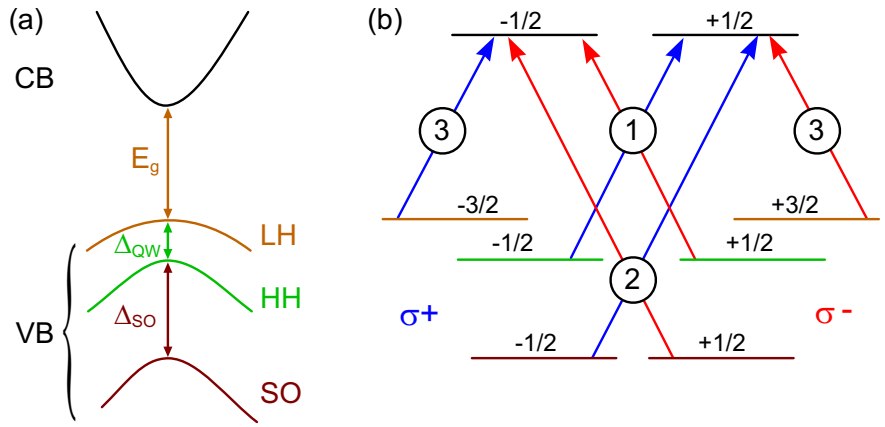

Figure 3.1: (a) Sketch of the bandstructure of a zinc-blende crystal at the Γ-point. Conduction band (CB) and valence band (VB) are separated by the bandgap E_g. The valence band states are p-type and consist of light-hole (LH), heavy hole (HH) and split-off (SO) band. The energetic splitting between the SO and the HH band is due to SOI. In a quantum well, the LH and HH bands are split by Δ_{QW} but they are degenerate at Γ in the bulk. (b) Transition probabilities for σ^+- and σ^--polarized light. Each level is labeled by its m_j quantum number. For σ^+ (σ^-), only transitions with $\Delta m_l = +1$ (-1) are allowed. Numbers in circles denote relative transition probabilities. Energetically selecting transitions only from the LH (HH and LH) band in a quantum well (bulk) leads to a maximal spin polarization of 100 % (50 %) of photo-generated charge carriers. The figure is adapted from Ref. [54].

of different contributions to the Faraday/Kerr rotation had been developed [50], which allowed to identify plasma [51], interband and spin contributions [52]. In recent years, the magneto-optical Kerr effect is increasingly used for studies of superconductors [53].

Now we want to describe the phenomenon of optical orientation. The first optical pumping of spins in a semiconductor was demonstrated in Si in 1968 [55]. In the following, we will adopt the explanation of optical orientation given by Meier et al. [54, 56]. Figure 3.1 shows a schematic energy diagram for the lowest conduction band and the uppermost valence band states in a zinc-blende crystal at the Γ-point. The wave-function in the conduction band has s-symmetry, while the one in the valence band has p-symmetry. At $k = 0$, SOI further splits the p-states into a heavy-hole, a light-hole and a split-off band. While the first is characterized by a m_j quantum number of $\pm 3/2$, the latter two have $m_j = \pm 1/2$. For $\sigma^{\pm}$-polarized light, the optical selection rule dictates $\Delta m_l = \pm 1$. This allows the optical transitions indicated in Fig. 3.1. The relative transition probabilities (indicated by the numbers in the circles) are calculated via the matrix elements of the dipole moment. If all transitions are excited, one obtains an equal number of spin +1/2 and -1/2. Only if we can energetically select the transitions from

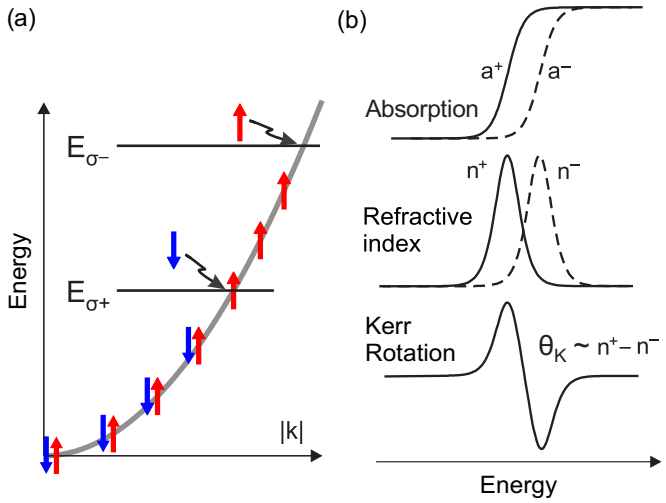

Figure 3.2: (a) Energetic dispersion for conduction band electrons along an in-plane k vector [cf. Eq. (2.1)]. $E_{\sigma+}$ ($E_{\sigma-}$) is the quasi Fermi energy of spin up (spin down) electrons. (b) Because $E_{\sigma+} \neq E_{\sigma-}$ there is a different onset of absorption for σ^+ and σ^- light with respect to the photon energy. The absorption curves translate into the refractive indices n^+ and n^- via the Kramers-Kronig relation. As a result, the polarization axis of linearly polarized light is rotated after reflection by the Kerr angle θ_K. The figure is cited from Ref. [61] with kind permission of the author.

the light-hole and heavy-hole band, excluding the one from the split-off band, we can achieve a net build-up of up to 50% spin polarization. In a quantum well, additionally the light-hole and heavy-hole bands are split at $k = 0$, such that we can energetically select a single transition which makes possible to inject up to 100% spin polarized electrons. On the detection side, for a long time, the main methods were photoemission [54] and luminescence spectroscopy [57].

Although optical orientation and Faraday/Kerr rotation co-existed for decades, they have not been brought together until the 1990s. In 1994 Baumberg et al. presented the first transient Faraday rotation measurement of optically induced electron spins in magnetic ZnSe quantum wells [58]. This technique was later also applied to GaAs [25, 59] and CdTe [60].

For the case of a direct-gap semiconductor quantum well, we want to give a more phenomenological explanation of the magneto-optical Kerr effect. If there is an imbalance for electrons with spins oriented along or against the wave-vector of the incident light, we can assign different Fermi energies to both spin species [Fig. 3.2(a)]. Together with the mentioned selection rules, this explains the different absorption edges experienced by light with σ^+- and σ^--polarization [Fig. 3.2(b)]. Via the Kramers-Kronig relation, the absorption coefficient is coupled to the refractive index [62, 63]. Thinking of linearly polarized light as composed of equal amounts of σ^+- and σ^--polarized light, we realize that the latter two experience

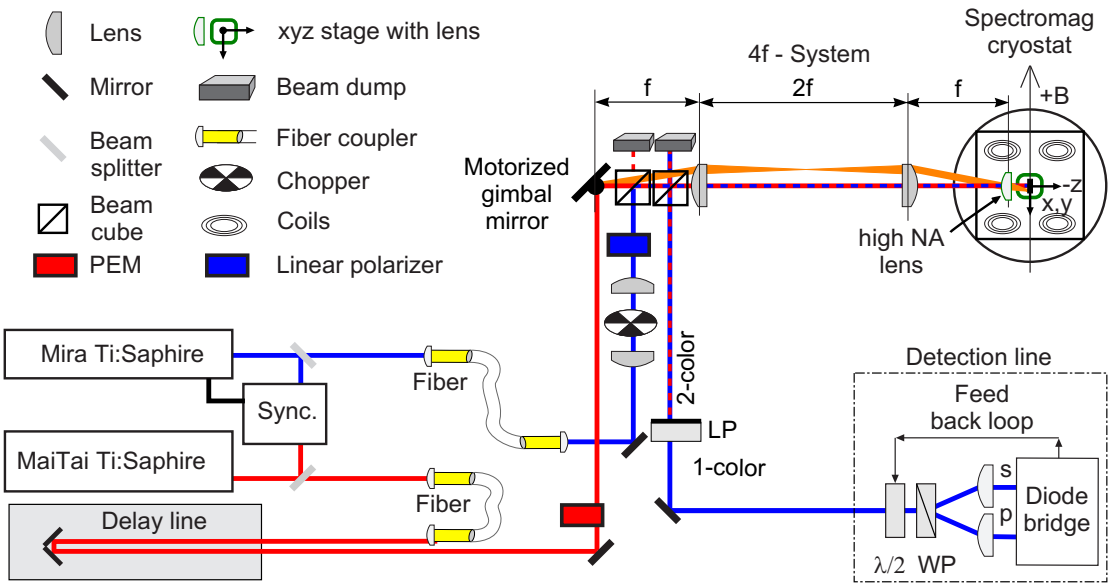

Figure 3.3: Schematic sketch of the measurement setup. A detailed description is found in the main text. This figure is adapted from Ref. [61].

different refractive indices if the photon energy is tuned to the region between the absorption edges. This leads to a phase-shift between σ^+- and σ^--components in the reflected beam and by that to a rotation of the linear polarization by the Kerr angle θ_K.

One must bear in mind that the optical creation of electron spins also creates spin-polarized holes. Thus, the lifetime of the electron spin excitation can be limited by the electron-hole recombination time. This is different in n-doped systems. It was demonstrated that in the presence of resident charge carriers, the spin lifetime surpasses the radiative lifetime [64]. This is explained by that the hole looses its spin information within 1 ps and recombines without spin selectivity with any resident or optically injected electron. This means that, in the limit of spin polarization small compared to the background carrier concentration, the number of spin polarized electrons is not reduced by recombination with holes. It was further argued [65, 66] that optical spin injection in a remotely doped quantum well may involve the formation of a trion.

3.2 Our scanning Kerr setup

The work presented in this thesis has greatly profited from the scanning Kerr microscopy setup which was built during the PhD work of M. Walser and has seen only minor changes since. While in the following we will give a detailed description of the measurement scheme (see Fig. 3.3), we refer to Ref. [61] for further reading.

We apply a pump-probe technique, where the role of the pump is to inject spins into a semiconductor quantum well by optical orientation and the role of the probe is to detect the spin density at a defined time delay via the magneto-optical Kerr effect (see previous section). Because of limited space in the cryostat, both laser beams are collinear from the first beam cube after the motorized gimbal mirror on. It is, hence, not possible to filter the pump pulse spatially by simply blocking it and the filtering of the pump beam is accomplished by a suitable long-pass filter (LP). For this reason we work with pump and probe pulses at different wavelengths. While the probe is tuned to maximize the Kerr signal, the pump is slightly higher in energy. To generate both laser beams, we use two Ti:Sapphire lasers (Coherent Mira 900 and Spectra-Physics MaiTai) that are synchronized by a Coherent Synchrolock unit. Both beams are fed through a single-mode fiber, not only for practical reasons, but also for beam shaping as such fibers emit a Gaussian mode. While the probe reaches the gimbal mirror via a linear polarizer, the pump reaches it via a mechanical delay line and a photo-elastic-modulator (PEM). The latter is an optical element which modulates at 50 kHz between σ^+- and σ^--polarized light. This modulation is not only useful for lock-in detection, it also helps to reduce spurious signal from other electro-optical effects. The probe beam is further modulated by a mechanical chopper to facilitate a 2-lock-in scheme as explained in the next paragraph. The probe beam is then centered by a mirror and a beam cube onto the focusing lens inside the cryostat. For the pump beam, more effort has to be undertaken to enable a scanning of the pump spot on the sample surface without a clipping of the pump beam on the focusing lens or the cryostat windows. For this, we implemented a 4-f system. This consists of a lens in 1-f distance from the gimbal mirror and another one in 1-f distance from the focusing lens. Both lenses have a distance of 2-f to each other. This alignment has the effect that, when scanning the mirror, the pump will always hit the focusing lens centrally, without a change in collimation, and the only effect of the scanning being that the angle under which the pump hits the focusing lens changes. Thus, a scanning of the pump is possible without clipping and by this maintaining a Gaussian beam profile. The reflection of both beams from the sample is collected in a confocal way by the focusing lens. By a second beam cube the reflection is guided to the detection line before which the pump beam is blocked by a suitable longpass filter. At the heart of the detection line is a balanced photo-diode bridge. This is a very suitable scheme for the detection of Kerr rotation. The principle is that the still dominantly linear probe beam is split by a Wollaston prism into s- and p-polarized beams each of which is then focused on a single photo-diode. A feedback loop automatically adjusts a $\lambda/2$-plate before the Wollaston prism until the signal for both diodes is equal. The feedback loop is too slow for the 50 kHz modulation of the pump and so the Kerr signal is detected in the difference voltage.

We further apply a 2-lock-in technique. This is not necessary when the pump beam is completely blocked. However, residual pump light easily leads to artifacts in the signal. Therefore, we use a first lock-in (Signal Recovery 7265) to detect at the modulation frequency of the PEM (50 kHz) with a typical integration time of 160 or 320 μs. The 'Fast-X-Out' signal of the first lock-in is then fed to a second lock-in that detects at the chopper frequency (typically 160 to 500 Hz) with an integration time ranging from 50 to 500 ms. This way it is made sure that we only measure signals that stem from the probe and are sensitive to the handiness of the circular polarization of the pump beam.

The focusing lens inside the cryostat has a diameter and a focal length of 10 mm at a numerical aperture of 0.545. With this we achieve Gaussian spot profiles of about $\sigma = 0.8$ μm at typical wavelengths of around 800 nm. For the resolution of the spin dynamics, the convolution of both, pump and probe spots, is relevant and leads to a minimal $\sigma = 1.1$ μm in this respect. Although it was not applied for the measurements presented in this thesis, one possibility to increase the spatial resolution is the use of a solid immersion lens as presented in Appendix A.3.

The lens is mounted in the cage of the cryostat insert, which further encloses the sample holder with its electrical connections (relevant for the measurements in Chapter 5) on top of a stack of attocube piezo slip-stick drives. These drives allow the positioning of the sample with respect to the laser spots by the x and y axes, while the z axis allows for positioning the sample in the focal plane.

The cryostat is a Oxford Spectromag system where the sample is loaded on the sample stick into the variable temperature insert (VTI). The VTI is connected to a liquid helium bath via a capillary and a needle valve. Under normal operation, the VTI is pumped by a rotary pump and the temperature is controlled by the flow of liquid helium via the needle valve and a heater at the bottom of the VTI. The sample is, thus, in the exchange gas with a good temperature coupling. With this scheme, temperatures from 1.4 to 300 K are possible. Magnetic fields up to 7 T are applicable by superconducting split-ring coils. The orientation of the field is horizontal as indicated in Fig. 3.3.

3.3 How to deal with finite spot sizes?

In Chapter 2, we provided expressions of the intrinsic precession pattern in the isotropic limit and for the PSH symmetry. Mathematically this is the Green's function of the spin diffusion equation. Numerically, it can be calculated by a Monte-Carlo simulation of the evolution of a δ-excitation. As described in the previous section, we can achieve a convoluted σ-size of the pump and probe spots of ≈ 1.1 μm and in the following, we want to discuss the consequences of this finite size onto the measured spin dynamics.

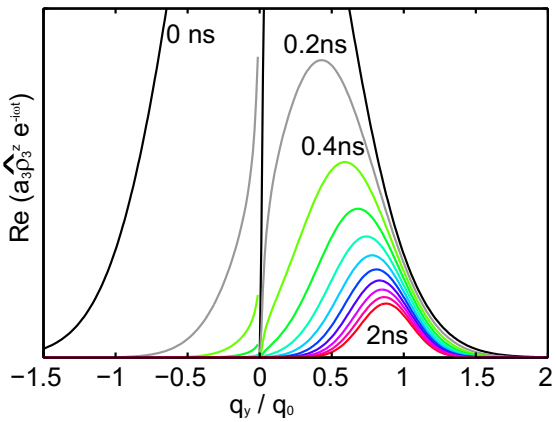

Figure 3.4: Time evolution of the z component of spin mode 3 in q space after an out-of-plane spin excitation of finite width in a one-dimensional system. At each q, the amplitude decreases with an exponential decay. The decay time at each q is approximately given by Eq. (3.1) and decreases with the distance of q from q_0. This leads to a gradual shift of the maximum towards q_0. More details are found in Ref. [31].

3.3.1 Theoretical treatment

We have learned in Section 2.3 that a δ-shaped spin excitation in space evolves into the intrinsic precession pattern because it excites all wavenumbers in Fourier space equally. If, instead, the initial excitation is described by a Gaussian function of finite width σ_0, the initial excitation in Fourier space is also a Gaussian function of width $1/\sigma_0$. This means that the excitation is initially strongest at $q = 0$.

In the following, we consider a system close to the PSH symmetry. Figure 3.4 shows the time evolution of spin mode 3 after a local out-of-plane spin excitation of finite width in a one-dimensional (1D) case (see Ref. [31] for details). Because the decay rate around q_0 is described by [cf. Eq. (2.19)]

$$1/\tau(q) = 1/\tau_0 + D_s(q - q_0)^2 \,, \tag{3.1}$$

the amplitude of spin mode 3 decays faster, the more q deviates from q_0 where it has the maximum lifetime τ_0. This leads to a gradual shift of the center to $q = q_0$. Interestingly, the shape of $\tilde{S}_z(q)$ remains Gaussian at all times.[1] This shift from $q = 0$ to $q = q_0$ means that the observed wavenumber in an experiment with finite sized pump and probe spots only gradually approaches the wavenumber of the spin mode [31].

For a situation close to the PSH symmetry, we can give an approximate solution of the spin diffusion equation taking into account a finite sized initial spin excitation. There, the evolution of a Gaussian spin excitation of S_z at $t = 0$ with

[1] This is not the case away from the PSH symmetry.

a finite width σ_0 is described by [31]

$$S_z(x,y,t) = S_z(0,0,0)\frac{\sigma_0^2}{\sigma^2(t)}\exp\left(-\frac{x^2+y^2}{2\sigma^2(t)} - D_s q_0^2 \frac{\sigma_0^2}{\sigma^2(t)}t - \frac{t}{\tau_0}\right) \times \begin{pmatrix} 0 \\ \sin q(t)y \\ \cos q(t)y \end{pmatrix}, \tag{3.2}$$

with

$$\sigma^2(t) = \sigma_0^2 + 2D_s t\,, \tag{3.3}$$

and

$$q(t) = \left(1 - \frac{\sigma_0^2}{\sigma^2(t)}\right) q_0\,. \tag{3.4}$$

This is a generalization of Eq. (2.23) and τ_0 is identical to τ_{PSH}. We see not only that the wavenumber becomes time-dependent, but also that there is an additional decay term, $\exp\left(-D_s q_0^2 \frac{\sigma_0^2}{\sigma_0^2+2D_s t}\right)$. Figure 3.5 shows experimental proofs of both predictions. Figure 3.5(a) compares measured $q(t)$ for $\sigma_0 = 1$ μm and $\sigma_0 = 2.2$ μm. The temporal evolution in both cases is perfectly described by Eq. (3.4). The impact of the additional decay term is nicely seen in Fig. 3.5(b), which plots the amplitude decay of $S_z(0,0,t)$ for both cases. In this semilogarithmic plot, we see that the actual spin dephasing time τ_0 is only dominant at later times. The beginning is dominated by diffusive dilution, $\frac{\sigma_0^2}{\sigma_0^2+2D_s t}$, and the additional decay term. We see that not only the signal decays more quickly when the laser spots become larger, also the observed spin dynamics becomes more and more masked by the convolution with the laser intensity profiles. We will come back to this point in Section 3.3.3.

Interestingly, Eq. (3.2) for large laser spots ($\sigma_0 \to \infty$), $\alpha = \beta^*$ and $\beta_3 = 0$ predicts an exponential decay with a decay rate $\frac{8m^{*2}D_s}{\hbar^4}2\alpha^2$, which is identical to the Dyakonov-Perel limit [cf. Eq. (2.16)].

The model of Eq. (3.2) will be used to analyze the impact of wire confinement on the spin dynamics close to the PSH symmetry in Section 4.4.

3.3.2 Fourier transformation approach

We have learned in Section 2.3 that a δ-excitation excites spin modes that have a certain decay rate at every wavenumber q. One mode has the lowest decay rate at a certain q_0 and is the spin mode we are usually interested in. In the previous section, we saw that the experimental limitation to finite sizes of the initial spin excitation leads to artifacts and masks the actual spin dynamics. Thus, we are looking for ways to accurately analyze a spatially and temporally resolved spin map.

The analytical model of Eq. (3.2) is valid only for a system close to the PSH

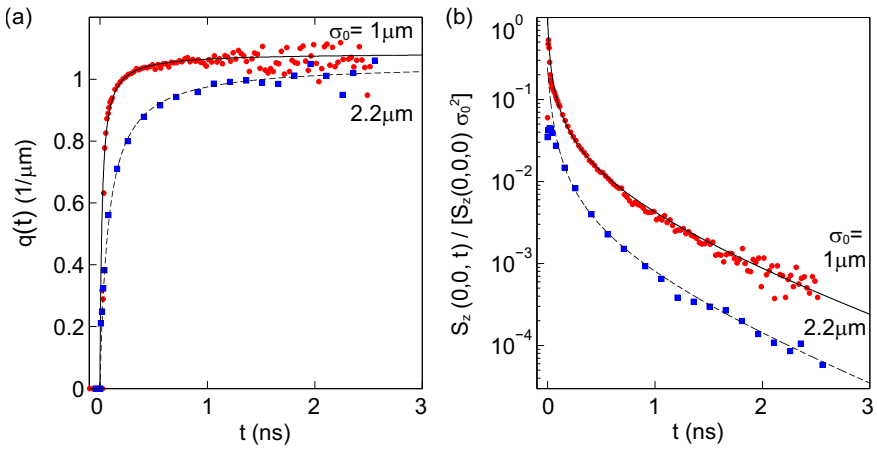

Figure 3.5: Dynamics of a local spin excitation of size $\sigma_0 = 1$ μm (dots) and 2 μm (squares). The experimentally observed dynamics (symbols) is compared with a theoretical model (curves). In (a) the time dependence of the wave number $q(t)$ is shown, and in (b) the spin polarization amplitude $S_z(0,0,t)/(S_z(0,0,0)\sigma_0^2)$ is shown.

condition. For isotropic SOI, such a model is missing. The approach presented in this section makes use of Eq. (2.20), which describes how the real space representation of the spin modes is connected to the eigenvectors of the spin-orbit matrix $\tilde{\mathbf{D}}$ [Eq. (2.18)]. The idea is that the real space data is Fourier transformed into $\tilde{S}_z(q,t)$, which gives access to $\sum_{n=1}^{3} a_n \hat{\boldsymbol{\rho}}_n$. The advantage lies in the fact that each $\hat{\boldsymbol{\rho}}_n$ is simply described by an exponential decay. For a localized out-of-plane spin excitation, mainly modes 2 and 3 are excited [31] so that the Fourier transformation of $S_z(x,y,t)$ is expected to show a double-exponential decay [27, 31]. Because under normal operation, only traces of the spin dynamics along one spatial direction are recorded, such a Fourier transformation must assume either one-dimensionality or radial symmetry as we will see in the following.

Isotropic SOI

Figure 3.6(a) shows synthetic data of $S_z(y,t)$ generated with Eq. (2.21). For a situation close to the isotropic case, one can assume radial symmetry of $S_z(x,y,t) = S_z(r,t)$. Thus, the real space data, $S_z(y,t)$, as seen in Fig. 3.6(a) can be transformed into its Fourier representation $\tilde{S}_z(q,t)$ as seen in Fig. 3.6(b) via this formula:

$$\tilde{S}_z(q,t) = \int_{-\infty}^{\infty} \pi |y| \mathrm{J}_0(qy) S_z(y,t) \mathrm{d}y \ . \tag{3.5}$$

J_0 is the zeroth-order Bessel function. As expected, the temporal decay of $\tilde{S}_z(q)$ is slowest at $q = \pm q_0$. Figure 3.7(a) plots this decay at q_0 and, indeed, it is well described by a double exponential decay (green line). This gives access to the

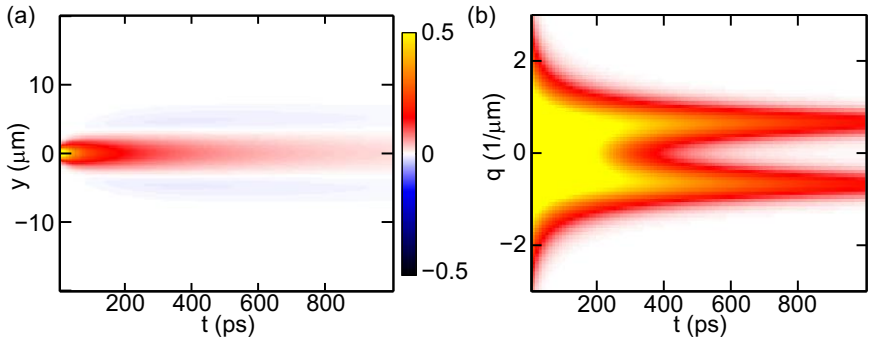

Figure 3.6: (a) Colormap of $S_z(y,t)$ as defined by Eq. (2.21) for isotropic SOI. (b) The Fourier spectrum $\tilde{S}_z(q,t)$ of (a) obtained via Eq. (3.5) shows a decaying amplitude at every q, with different decay rates and a maximum lifetime at $q = \pm q_0$.

dephasing time of the longer lived spin mode by fitting the decay rate at each q as shown in Fig. 3.7(b). Around q_0, the obtained rates agree perfectly with Eq. (3.1). Fitting such a dispersion relation, thus, gives access to the diffusion constant and the spin dephasing time.

Persistent spin helix

For a situation close to the PSH symmetry, one can not assume radial symmetry of S_z. Thus, we can not perform a Fourier-transformation from a scan along a single spatial axis via Eq. (3.5). In a wire structure (see Chapter 4), it is appropriate to assume one-dimensionality and we can apply the following formula to obtain $\tilde{S}_z(q,t)$.

$$\tilde{S}_z(q,t) = \int_{-\infty}^{\infty} \cos(qy) S_z(y,t) \mathrm{d}y \ . \tag{3.6}$$

Figure 3.8(a) shows $S_z(y,t)$ for a spin helix in a wire and Fig. 3.8(b) the $\tilde{S}_z(q,t)$ as obtained by Eq. (3.6). The analysis of this data is then performed analogously to the 2D case for isotropic SOI. Alike, the dispersion relation of the decay rate of the longer lived spin mode is obtained [Fig. 3.8(c)] and around q_0 is well approximated by Eq. (3.1) giving access to q_0, τ_0 and D_s.

The analysis of the Fourier components is perfectly applicable for the study presented in Section 4.3 because it is valid for a Bessel-type spin mode in two dimensions as well as for a helical spin mode in a wire.

3.3.3 Convolution approach

Another possibility to consider the impact of finite spot sizes is to numerically convolve the spin dynamics as described in Section 2.3 with a Gaussian profile. The

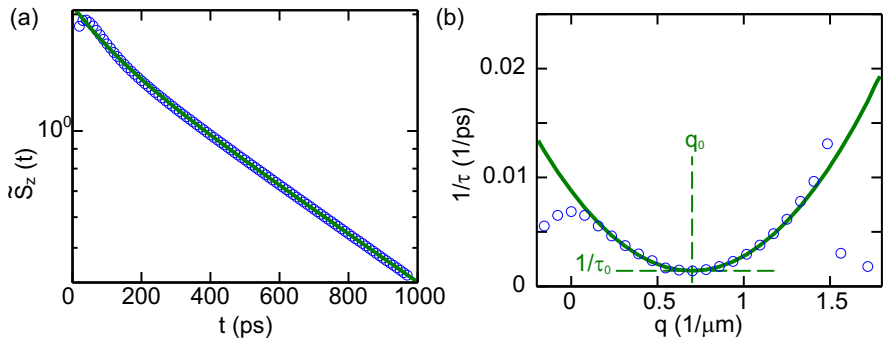

Figure 3.7: (a) $\tilde{S}_z(q \approx q_0, t)$ for the data shown in Fig. 3.6(b). At every q, the decay of $\tilde{S}_z(q,t)$ is well described by a double-exponential fit (green line). (b) The decay rate $1/\tau(q)$ of the longer lived spin mode has a minimum, $1/\tau_0$, at q_0. The green line is defined by Eq. (3.1).

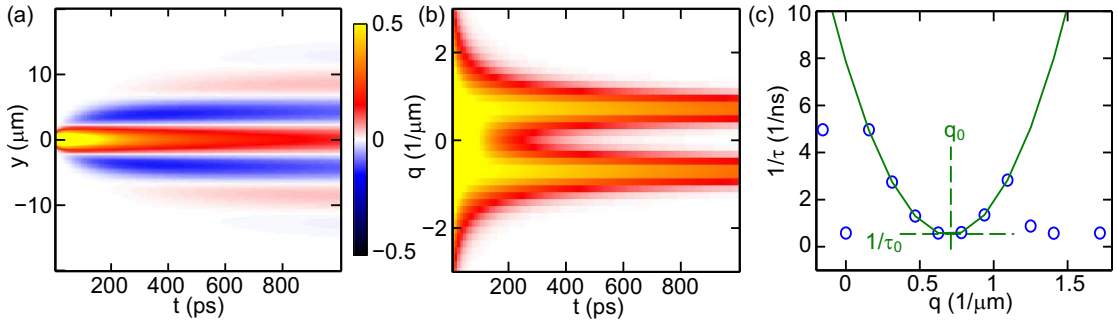

Figure 3.8: (a) Colormap of $S_z(y,t)$ as defined by Eq. (2.23) for $\alpha = \beta^*$. The PSH is described by a cosine oscillation in real space. (b) $\tilde{S}_z(q,t)$ for the data in (a) obtained via Eq. (3.6). (c) The decay rate $1/\tau(q)$ of the longer lived spin mode has a minimum, $1/\tau_0$, at q_0. The green line is defined by Eq. (3.1).

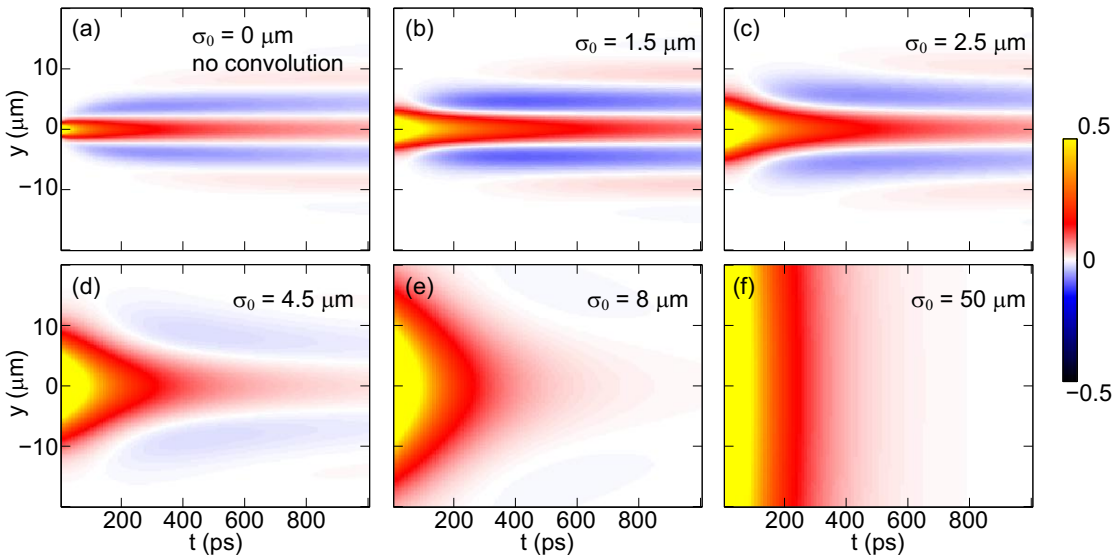

Figure 3.9: Temporal evolution of $S_z(y,t)$ after convolution with different σ-widths mimicking the effect of the laser spots. (b) to (f) are generated by a 1D convolution of the data of panel (a) with Gaussian functions of σ-widths of 1.5, 2.5, 4.5, 8 and 50 μm, respectively.

width of this profile itself is defined by the convolution of the pump and the probe spot. Interestingly, the role of pump and probe in this sense are interchangeable. It has the same effect to excite spins with a spatial uncertainty of σ_{pump} or to detect them with an uncertainty σ_{probe}. Thus, the Gaussian that has to be used for the convolution has the width $\sigma_0 = \sqrt{\sigma_{\text{pump}}^2 + \sigma_{\text{probe}}^2}$.

One-dimensional spin dynamics

As we will see in Chapter 4, the Green's function of the spin diffusion equation in the case of a wire always yields a spin helix. The difference between this 1D case and Eq. (2.23) is that the prefactor $1/2D_s t$ has to be replaced by $1/\sqrt{2D_s t}$ because of 1D diffusion. Like this, we analytically generate the evolution of $S_z(y,t)$ for such a situation and show it in Fig. 3.9(a). For numerical reasons, we assume an initial width of the Gaussian envelope of $\sigma_0 = 0.2$ μm.

Figures 3.9(b) to (f) are generated by a 1D convolution of the data of panel (a) with Gaussian functions of σ-widths of 1.5, 2.5, 4.5, 8 and 50 μm, respectively. The observed spin dynamics changes drastically along this line. While for the smaller spot sizes, the intrinsic precession pattern is still observable, albeit with artifacts, at $\sigma_0 = 50$ μm, no sign of the PSH can be found. All what is observed, is a fast decay of the amplitude.

That the observed wavenumber becomes time dependent, as we already learned

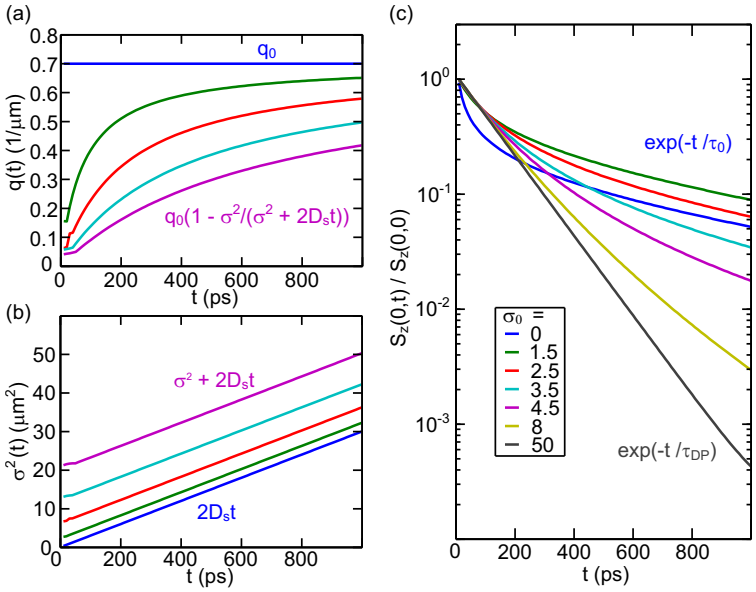

Figure 3.10: (a) Temporal evolution of $q(t)$ for different σ-widths of the laser spots. (b) Temporal evolution of $w^2(t)$ for different σ-widths of the laser spots. (c) Amplitude decay $S_z(0,t)$ for different σ-widths of the laser spots. The legend in (c) is valid for all three subfigures.

from Eq. (3.2), is also clearly visible in these maps. When we fit this wavenumber at every time step for all σ-widths, we see [Fig. 3.10(a)] that the observed $q(t)$ approaches q_0 only asymptotically and within a measurement time of 1 ns is still only 50 % of the actual value for $\sigma_0 = 4.5$ μm. We see that, although the spot size is smaller than the spin-orbit length of $l_{\mathrm{SO}} = 2\pi/q_0 = 9$ μm, the impact onto the observed spin dynamics is severe. These findings are in perfect agreement with the predictions of Eq. (3.2). Also the width of the Gaussian envelope after convolution follows the prediction of $\sigma^2(t) = \sigma_0^2 + 2D_s t$ [Fig. 3.10(b)].

A very interesting transition can be observed in Fig. 3.10(c) where the amplitude decay $S_z(0,t)/S_z(0,0)$ for all spot sizes is compared. Without convolution, the decay is in the beginning dominated by diffusive dilution. For a δ-peak the term $\frac{\sigma_0^2}{\sigma_0^2+2D_s t}$ must actually go towards infinity for $t \to 0$ and is only reaching a finite value because we chose an initial $\sigma_0 = 0.2$ μm for numerical reasons. At later times, the term decays slower and the exponential function becomes dominant. As soon as we do the convolution, the initial decay is a result of both, the diffusive dilution and the additional decay term. The time from which on the decay actually follows $\exp(-t/\tau_0)$ shifts to later times the larger σ_0. In this example, with $\sigma_0 = 50$ μm the dynamics is already in the limit of very large laser spots, where we observe the decay of the spin excitation with the Dyakonov-Perel rate as predicted by Eq. (3.2).

Two-dimensional spin dynamics

For a 2D situation, it is necessary to make a 2D convolution of $S_z(x, y, t)$ with the 2D Gaussian spot profile to correctly mimic the spin decay observed in an experiment. As we typically only scan along one spatial direction in the experiment, we have to make an assumption on the symmetry of the spin dynamics to generate the 2D pattern of $S_z(x, y)$. For isotropic SOI, radial symmetry can be assumed. In the PSH limit, $S_z(x, y)$ can be synthesized by considering that spins precess only along one spatial direction and not along the perpendicular one.

While it is certainly possible, the 2D convolution is disadvantageous in terms of computing time. Thus, for the studies presented in Section 4.3 we preferred the analysis in Fourier space as explained in the previous section.

Also in Chapter 5 the system is 2D with the SOI being close to the PSH symmetry. For the analysis there, we chose to use a 1D convolution approach as described above. This is only valid, if the spin texture is a constant function perpendicular to the scanning axis within the laser spot size. This is approximately true in the limit that $2D_s t \gg \sigma_0^2$, and the 1D approximation is acceptable. Therefore, we use the 1D convolution approach instead of the 2D convolution approach because of the much shorter computing time and fit the data only for $t > 300$ ps.

3.4 Comment on large laser spots

In the previous section, we have seen that the spot size plays a significant role for the resolution of the intrinsic precession pattern. In an optical experiment as described in Section 3.2, the size of pump and probe spots set the relevant length scale. In a situation where the spins are electrically injected and/or detected, the dimensions of the contacts and mesa structure are relevant. In either case, one has to consider how well defined the point of excitation or detection is. If it is possible to excite and resolve the intrinsic precession pattern with a resolution better than l_{SO}, it is possible to measure the intrinsic spin lifetime τ_0, the wavenumber of the spin mode q_0 and the spin diffusion constant D_s. This is enough information to directly determine the strength and anisotropy of the SOI parameters α and β^*. If, however, the spatial resolution is poor, the intrinsic precession pattern can not be resolved and we measure in the Dyakonov-Perel limit (cf. Fig. 3.9). The determined lifetime is then the Dyakonov-Perel time τ_{DP} as explained in Section 2.2. The strength of the SOI can then not be determined without the additional knowledge of D_s. Sometimes D_s is calculated from the transport mobility, which is incorrect as explained in Section 2.2.

3.5 Alternative methods for the determination of spin-orbit parameters

In the previous section, we have noted that, without sufficient spatial resolution, an experiment accesses the spin dynamics in the Dyakonov-Perel limit and the spin-orbit parameters can not be determined. In the following, two alternative methods shall be briefly presented, which circumvent the lack of spatial resolution by superposing an external magnetic field to the spin-orbit fields.

3.5.1 Drift-induced spin precession

This section summarizes the method presented and applied in Refs. [67, 11, 68, 69]. One uses laser spots that are large enough to assume the Dyakonov-Perel limit, i.e. a spin excitation decays exponentially with the Dyakonov-Perel time τ_{DP} (see Section 2.2) and additionally the probe spot is large enough that the diffusive dilution within in the measurement time is negligible ($2D_{\mathrm{s}}\tau_{\mathrm{DP}} \ll \sigma^2_{\mathrm{probe}}$).
Without accounting for SOI, spins oriented along z will collectively precess about an in-plane B_{ext} as a function of time with a frequency

$$\omega_{\mathrm{ext}} = \frac{g\mu_{\mathrm{B}}}{\hbar} B_{\mathrm{ext}} \,. \tag{3.7}$$

Assuming isotropic scattering, diffusion results in an averaging of the experienced spin-orbit fields that for a large ensemble of spins leads to spin decay but not to a precession of the net spin polarization, because $\langle \mathbf{B}_{\mathrm{SO}} \rangle = \int_0^{2\pi} d\theta\, \mathbf{B}_{\mathrm{SO}}(\mathbf{k}) = 0$. If, however, the Fermi sea is subjected to drift, a displacement of the Fermi circle by the drift vector $\mathbf{k}_{\mathrm{dr}} = (k_{\mathrm{dr},x}, k_{\mathrm{dr},y})$ can lead to a non-zero drift-induced effective magnetic field. For the case of Dresselhaus SOI and for drift along the [110]-direction [cf. Eq. (2.11)]:

$$\langle \mathbf{B}_{\mathrm{SO}}(\mathbf{k}_{\mathrm{dr}}) \rangle = \int_0^{2\pi} d\theta\, \mathbf{B}_{\mathrm{SO}}(\mathbf{k} + \mathbf{k}_{\mathrm{dr}}) = \frac{2(\beta_1 - 2\beta_3)}{g\mu_{\mathrm{B}}} \begin{pmatrix} k_{\mathrm{dr},x} \\ -k_{\mathrm{dr},y} \end{pmatrix} . \tag{3.8}$$

Although it is in principle possible to resolve a spin precession about $\langle \mathbf{B}_{\mathrm{SO}}(\mathbf{k}_{\mathrm{dr}}) \rangle$ [70], this drift-induced spin-orbit field is small for moderate k_{dr} and it is helpful to apply an external magnetic field $\mathbf{B}_{\mathrm{ext}}$ in the quantum well plane [cf. Fig. 3.11(a)]. Typically, a field of $\mathbf{B}_{\mathrm{ext}} = 1$ T is enough for GaAs based quantum wells to observe several precession periods. The effect of $\langle \mathbf{B}_{\mathrm{SO}}(\mathbf{k}_{\mathrm{dr}}) \rangle$ is then a shift of the precession frequency. To be precise, under the condition that $\langle B_{\mathrm{SO}}(\mathbf{k}_{\mathrm{dr}}) \rangle \ll B_{\mathrm{ext}}$, the observed frequency shift can be approximated by

$$\Delta\omega(\mathbf{k}_{\mathrm{dr}}) \approx \frac{|g|\mu_{\mathrm{B}}}{\hbar} \frac{\langle \mathbf{B}_{\mathrm{SO}}(\mathbf{k}_{\mathrm{dr}}) \rangle \cdot \mathbf{B}_{\mathrm{ext}}}{|\mathbf{B}_{\mathrm{ext}}|} \,, \tag{3.9}$$

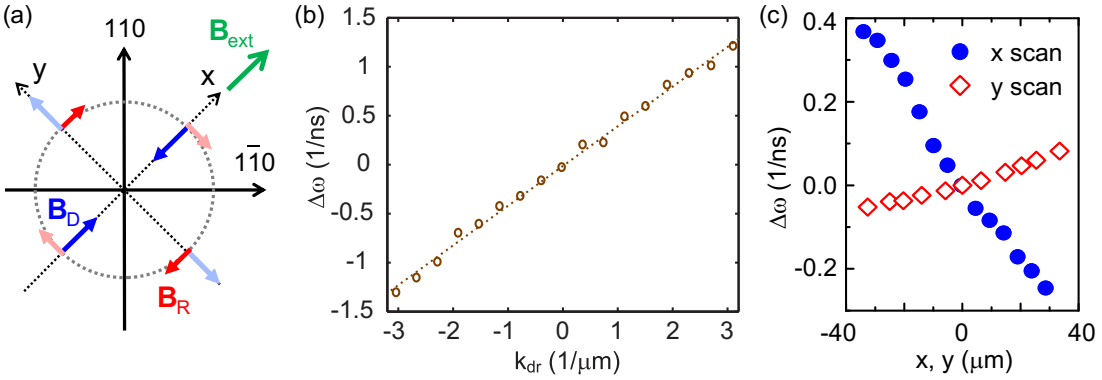

Figure 3.11: (a) The superposition of an external magnetic field to the spin-orbit field facilitates the determination of $\Delta\omega$ in both methods that are described in Sections 3.5.1 and 3.5.2. The orientation of B_{ext} must be such that it is parallel to the spin-orbit field of interest. (b) Fitted shift of the precession frequency $\Delta\omega$ in a drift experiment. The dependence on k_{dr} is linear as predicted by Eq. (3.9). This figure was adapted from Ref. [68] with kind permission of the authors. (c) In the all-optical approach, the spatial overlap is varied instead of a drift vector. Because of Eq. (3.10), the fitted $\Delta\omega$ exhibits a linear dependence on the overlap mismatch as predicted by Eq. (3.12).

i.e. it is sensitive to the projection of $\langle \mathbf{B}_{\text{SO}}(\mathbf{k}_{\text{dr}}) \rangle$ onto $\mathbf{B}_{\text{ext}}$. This gives the freedom to take advantage of the different symmetries of the Rashba and Dresselhaus components by choosing different geometries for $\mathbf{B}_{\text{ext}}$ and $\mathbf{k}_{\text{dr}}$ with respect to the crystallographic directions to independently map out the strength of the Rashba and Dresselhaus SOI [see Fig. 3.11(a)].
Typically the drift vector is varied as can be seen in Fig. 3.11(b). The spin-orbit strength is taken from the slope of the linear dependence of $\Delta\omega$ on k_{dr}.

The described method, hence, allows the experimental determination of the strength and symmetry of the SOI without a need to resolve the intrinsic precession pattern. Quantities that are directly related to the spin mode can not be accessed, particularly τ_0.

3.5.2 All-optical approach using medium-sized laser spots

While the above method does not require to focus the pump and probe laser beams, it is necessary to fabricate mesa structures and electrical contacts to the 2D electron gas. In the following, an alternative method [71] shall be sketched which is all-optical, i.e. without the need for sample processing, and only requires moderate spot sizes that may be larger than the spin-orbit length. The concept of this method is very similar to the one just described, however, the role of the drift motion of the electrons is now taken by diffusive motion. For a spin ensemble in a 2D electron gas, scattering, i.e. diffusive motion, does not lead to a net k-vector

of the ensemble. But if spins are measured in a certain distance and direction from the pump spot, the probe only samples a fraction of the injected ensemble of spin-polarized electrons, which at a given time has diffused towards this point. This means that, if pump and probe spot are separated by a distance r, the spins measured by the probe had an average velocity [71]

$$v_{\mathrm{di}} = \frac{2D_{\mathrm{s}}}{2D_{\mathrm{s}}t + \sigma_{\mathrm{eff}}^2} r \,, \tag{3.10}$$

where σ_{eff} is defined by the convolution of the Gaussian profiles of pump and probe spots:

$$\sigma_{\mathrm{eff}}^2 = \sigma_{\mathrm{pump}}^2 + \sigma_{\mathrm{probe}}^2 \,. \tag{3.11}$$

Thus, instead of varying an applied voltage to vary the drift vector, under this consideration it is sufficient to scan the relative displacement between the pump and probe spots to vary v_{di}. Besides that, the concept is the same as for the previous method. In an in-plane external magnetic field, the change in precession frequency, $\Delta\omega$, induced by SOI is analogously dependent on the projection of the diffusion-induced spin-orbit field on $\mathbf{B}_{\mathrm{ext}}$.

For a situation as sketched in Fig. 3.11(a), we obtain

$$\begin{aligned} \Delta\omega(x) &= -\frac{4m^* D_{\mathrm{s}} \beta^*}{\hbar^2 (2D_{\mathrm{s}}\tau_{\mathrm{s}} + \sigma_{\mathrm{eff}}^2)} x \,, \text{and} \\ \Delta\omega(y) &= -\frac{4m^* D_{\mathrm{s}} \alpha}{\hbar^2 (2D_{\mathrm{s}}\tau_{\mathrm{s}} + \sigma_{\mathrm{eff}}^2)} y \,. \end{aligned} \tag{3.12}$$

The time dependence of v_{di} sets the constraint that $\sigma_{\mathrm{eff}} \gg 2D_{\mathrm{s}}t$, such that v_{di} can be assumed to be constant within the measurement time. Then, also the observed temporal spin precession can be fitted by a single frequency although being an average of the frequencies within the observed time window. Because of the exponential decay of the spin polarization, earlier times are weighted more. It is therefore a good approximation to replace t in Eq. (3.10) by the fitted spin lifetime τ_{s}, which was done to obtain Eq. (3.12). In an experiment, one obtains curves like in Fig. 3.11(c) and β^* (α) is determined from the slope of the x-scan (y-scan).

Chapter 4

Effects of wire confinement on the spin dynamics

In the following chapter, we present measurements of spin dynamics of electrons confined in wire structures. The wire width is reduced in steps until a transition from two dimensions to one dimension is observed. The wire width remains large compared to the mean-free path of the electrons and 1D refers to the spin dynamics rather than the electronic system, which remains diffusive and 2D in our studies. Interestingly, the transition to one dimension is characterized by different manifestations depending on the symmetry of the SOI. Section 4.3 focuses on a quantum well where the SOI is approximately isotropic[1] and Section 4.4 looks at a sample in the PSH limit[2]. While in the first case, the transition is accompanied by an increase of the spin lifetime of about an order of magnitude, in the latter case, the PSH lifetime is hardly enhanced. In the PSH sample, however, we find evidence for a transition to 1D diffusion, which is not expected for the isotropic case. An overview over the impact of wire confinement on the spin dephasing time from the isotropic limit to the PSH symmetry is given in Section 4.5. For wire widths smaller than the ones in our study, first the ballistic and then the one-dimensionally quantized regime are entered, as we will discuss as an outlook in Section 4.6.

4.1 Expectations based on prior experimental and theoretical work

In Section 2.2, we explained how the diffusion of electrons leads to a dephasing of the electrons' spins. In Fig. 4.1(a), we recall the situation in a 2D system. As in

[1] These results have been published in Ref. [72].
[2] These results have been published in Ref. [73].

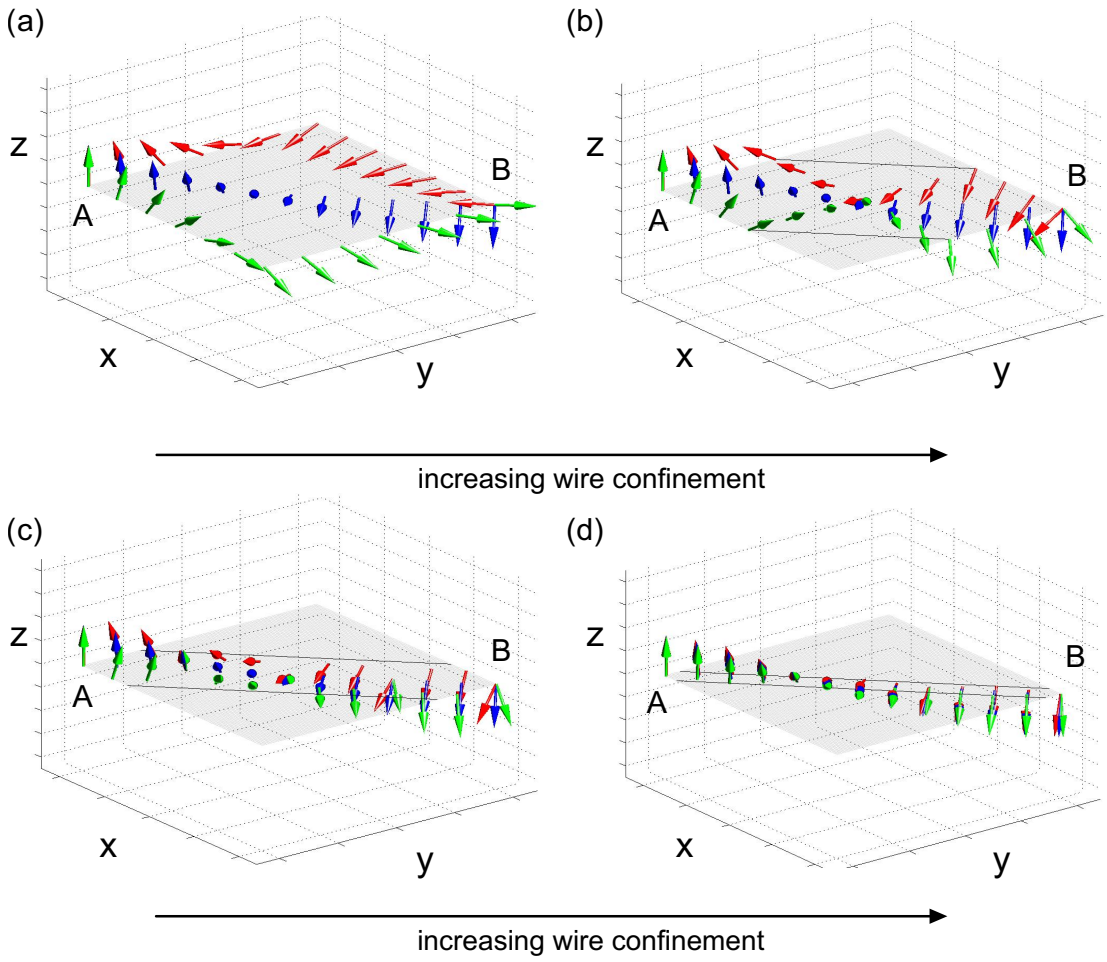

Figure 4.1: Comparison of three diffusive trajectories for increasing wire confinement. Plot (a) is identical to Fig. 2.3. Spins precess about the spin-orbit field defined by the k state of its electron. The precession sketched in this figure assumes Dresselhaus SOI.

Fig. 2.3, the electrons start at point A and go to point B on different trajectories. Every electron is assumed to occupy a k state on the Fermi circle. After a scattering event, the direction of motion and correspondingly the k vector is changed. The trajectory of the red spin is, thus, defined by a k vector along y before and a k vector along x after a scattering event. The opposite is true for the green spin. The blue spin reaches point B directly without a scattering event. As was discussed already in Section 2.2, the spin evolution is connected to the trajectory of the electron in real space via Eq. 2.11. In general, different trajectories lead to different states of the spins on the Bloch sphere even if the trajectories end at the same position. For this reason, the three spins are oriented into different directions at point B although they started with the same orientation at point A. In Fig. 4.1(b), we introduce sidewalls from which the electrons are reflected, i.e. we

assume specular scattering. We also take into account electron-electron scattering. Compared to Fig. 4.1(a), the orientation of the spins at point B is already more similar. The similarity increases for stronger confinement [Fig. 4.1(c)] and for the plot in Fig. 4.1(d), the evolution of the spins became almost identical. If the possible diffusive paths for an ensemble of electrons is constricted in a wire, the evolution of their spins is constricted to a ring on the Bloch sphere. This can be seen as an almost perfect rotation of all three spins in Fig. 4.1(d). With this rough sketch, we want to give an intuitive picture of why we expect wire confinement to result in an enhanced spin lifetime.

A more rigorous treatment of this situation was presented by Mal'shukov and Chao who considered wall boundaries for the solution of the spin diffusion equation [74]. The calculated spin lifetime, τ_{IM}, in a regime where the wire width w is smaller than the spin-orbit length ($l_{\mathrm{SO}} = 2\pi/q_0$) but larger than the mean-free path is given by [74, 75]

$$\tau_{\mathrm{IM}} = 48\tau_{\mathrm{DP}} \left(q_0 w\right)^{-2} \tag{4.1}$$

with τ_{DP} being the Dyakonov-Perel spin dephasing time as defined in Eq. (2.16). Furthermore, it was stated that a periodic rotation of a spin along the wire is expected [74]. Later this was identified theoretically as a helical intrinsic precession pattern in a wire [75]. Numerical simulations reproduced the scaling of the spin dephasing time with $(q_0 w)^{-2}$ [76].

The first experimental study dedicated to this scenario measured the wire-width dependence of the spin dephasing time in InGaAs wires by time-resolved Kerr rotation with large laser spots [77]. The spin dephasing time increased by less than a factor of three in wires, which were smaller than l_{SO} but still much wider than the electron mean-free path. But with laser spots large compared to l_{SO}, no access to the spin mode is possible (see Chapter 3.4). Additional theoretical work was needed to calculate the excitation and dephasing dynamics of spins in a wire excited and detected by large laser spots [75]. A qualitative agreement between an analytical description and the observed physics was achieved [75]. The spatial signature of the intrinsic precession pattern remained unresolved until in 2010 a first indication for a spin helix was found by a combined approach of optical excitation and electrical detection revealing an oscillatory spin amplitude along a wire [78].

Above considerations are focused on isotropic and linear SOI. Only very little work paid attention to how an anisotropy of the SOI changes the dynamics. In Chapter 2 we learned how the intrinsic precession pattern depends on the combination of Rashba and Dresselhaus SOI. It goes from a short-lived Bessel function in the isotropic limit to a long-lived helical state at the symmetry point of equal Rashba and Dresselhaus contributions. In wires, it was considered theoreti-

cally [79] that the resulting precession pattern would depend on the orientation of the wire with respect to the crystallographic axis, if the SOI is anisotropic. Experimentally, an optical study showed that the spin dephasing time can be different for wires along different crystallographic directions [80]. Because of the large laser spots used, this is only an indication for the anisotropy of the SOI but not for a suppressed spin dephasing time due to lateral confinement. Unfortunately, also the first spatially resolved measurement of spin dynamics in wire structures [81] did not provide additional insight. The recording of only three time steps does not give enough data for a reliable determination of the spin dephasing time. Further, the relation of Eq. (4.1) could not be tested because the wire width was not varied. The transition from a 2D precession pattern to a helical state in a wire has, thus, never been observed in an experiment. There is no experiment that varied the wire width to quantitatively confirm that the spin dephasing time increases with $(l_{\mathrm{SO}}/w)^2$.

4.2 Wire fabrication

Processing wire structures down to widths of a few micrometers is a comparably simple process. Photo-lithography and wet-chemical etching are used to fabricate wires from about 1 μm up to 80 μm. The used recipes are found in Appendix A.1. The downside of wet-chemical etching is that the process is isotropic, i.e. the side walls are not perpendicular to the sample plane but have an inclination of 30 to 40 degrees [82]. This means that the width of the structures in the quantum well plane needs to be determined by a suitable method, for instance by atomic force microscopy or by cross-sectional scanning electron microscopy. An additional difficulty is that the side wall introduces a potential, which entails a depletion region. In a transport study of InGaAs wires, this depletion region was estimated to be about 150 nm [83]. The total of 300 nm is negligible in structures of more than a few micrometer width, but needs to be considered in the narrowest wires presented in the following sections. In Section 4.4, we refer to the nominal width of the wires as defined by the lithography mask. In Section 4.3, we refer to the actual wire width as determined by scanning electron microscopy. The wire widths found are 1.3 μm smaller than the nominal widths.

Both GaAs quantum wells studied in this chapter have a width of 12 nm. The one of Section 4.3 was designed such that it is dominated by linear Dresselhaus SOI, i.e. is in the isotropic limit, while the one of Section 4.4 was designed to be close to the PSH condition. Further details on the samples can be found in Appendix A.2.

4.3 Isotropic spin-orbit interaction: transition to a helical state

In the case of isotropic SOI, i.e. for only linear Rashba or only linear Dresselhaus SOI, the spin dynamics is characterized by a short spin lifetime and the intrinsic precession pattern is described by a Bessel function (see Chapter 2.3.1).

In the following, we will measure the spatial evolution of a localized spin excitation in wire structures of various width by the method described in Section 3.2. The orientation of the wires is always parallel to the scan direction throughout this section. A measurement of spatially resolved spin dynamics in a channel in the 2D limit ($w = 19\,\mu\text{m} \gg l_{\text{SO}}$) is shown in Fig. 4.2(a). Spins are excited at $t = 0$ and at $x = y = 0$ and traced as a function of y and t. At $y = 0$, S_z simply decays in time. It reverses its sign after $t > 400$ ps for electrons that diffused along y by more than ≈ 4 μm, seen as a faint blue color in the Figure. The situation is different in the 700 nm-wide channel [Fig. 4.2(b)]. Here, spin decay is strongly suppressed and S_z reverses its sign multiple times along y. Note that the pattern is overlaid with the spin texture that survived from the previous pump pulse at $t = -12.6$ ns. Figure 4.2(c) shows measured data of $S_z(y)$ for the 19-μm and the 700-nm-wide channels taken at $t = 1.5$ ns. The comparison of the two curves clearly shows an enhanced S_z and strong oscillations along y in the narrow channel. This indicates a helical spin mode in the 1D case.

For a deeper analysis, it is advantageous to do the data analysis in Fourier space, as explained in Section 3.3.2. We Fourier-transform $S_z(x, y, t)$ to obtain Fourier components $S_z(q_x, q_y, t)$ at wave numbers q_x and q_y that according to theory decay biexponentially in time [27]. For channels narrower than 15 μm, the precession pattern exhibits a pronounced structure only along the channel direction, and it is therefore sufficient to analyze the 1D Fourier transformation along this direction. For a channel along the y direction, the Fourier transformation is given by Eq. (3.6). For wider channels, we obtain the 2D Fourier transformation from 1D scans of S_z by assuming a radially symmetric precession pattern. This is justified because we observe a similar dependence of S_z along the x and y directions, as seen from the values obtained for wavenumbers q_x^0 and q_y^0 later in the text. The Fourier transform is then given by Eq. (3.5).

Figures 4.2(d) and 4.2(e) show $S_z^{\text{2D}}(q_y, t)$ for the 19-μm wire and $S_z^{\text{1D}}(q_y, t)$ for the 700-nm wire, respectively. The rate with which the initially Gaussian distribution of $S_z(q_y, t)$ decays in time varies with q_y and is minimal at a finite wavenumber q_y^0. Figure 4.2(f) shows traces at $q_y \approx q_y^0$ for both wires. For $t > 500$ ps, we fit each trace with a single exponential decay to obtain the momentum-dependent lifetime $\tau(q_y)$ of the longer-lived spin mode [35, 27]. The decay rates, $1/\tau(q_y)$ are shown in Fig. 4.3(a). In both the 1D and the 2D case, $1/\tau$ vs q_y can

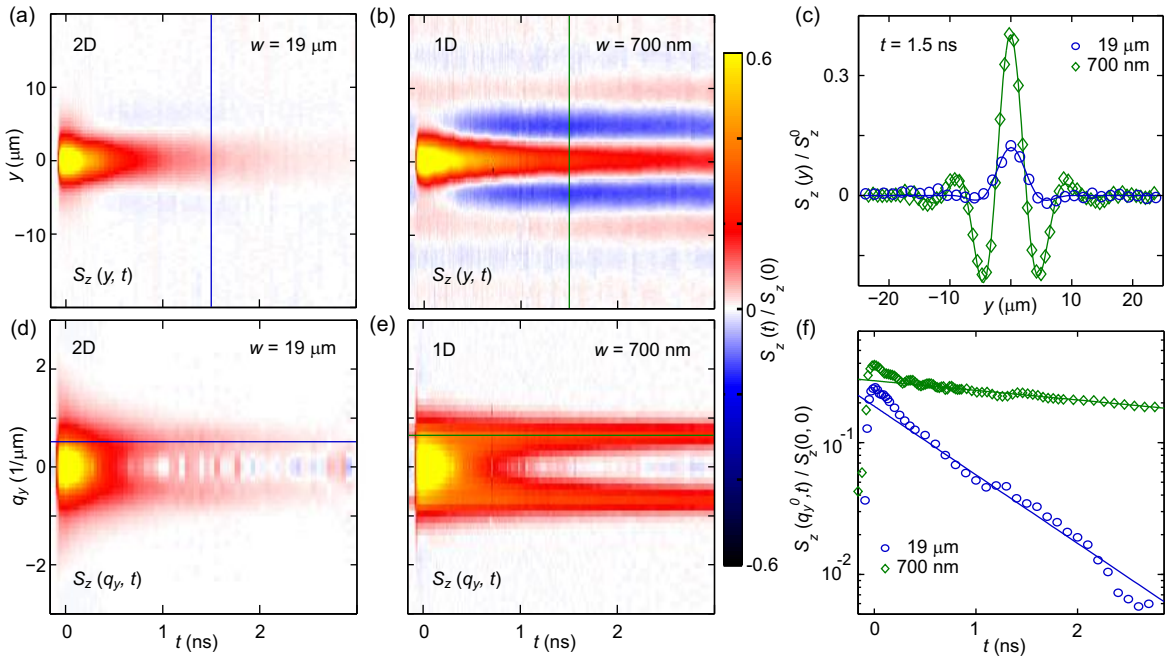

Figure 4.2: Direct mapping of spin precession and spin decay. (a)-(b) Spatial maps along the channel direction y of the out-of-plane spin density S_z for varying time delays t between the pump and probe laser pulses. The 19-μm-wide channel, (a), represents a 2D situation, whereas the 700-nm-wide channel, (b), is close to the 1D limit and exhibits a long-lived mode with oscillating $S_z(y)$ [sign encoded as red (+) and blue (-)]. The pattern from the preceding laser pulse (pulse period 12.6 ns) is still visible at negative delay. (c) Line-cuts through the data of (a) and (b) at $t = 1.5$ ns for comparison. (d) and (e) show the Fourier transform of $S_z(y)$ for the 19-μm and 700-nm channel, respectively. For $w = 700$ nm, the initially Gaussian spectrum quickly converges to a long-lived spin mode at finite $q_y = q_y^0$ (position indicated as blue and green horizontal lines). (f) Line-cuts through the data of (d) and (e) at $q_y \approx q_y^0$. At each q_y, the amplitude decays biexponentially, with the longer-lived mode visible at longer t.

be well approximated close to q_y^0 by the parabolic function of Eq. (3.1) [23, 27].

Figures 4.3(b) and 4.3(c) plot the values obtained for q^0 and τ^0, respectively, for channels along the y and x directions and of various widths. Values of τ^0 obtained with 2D and 1D Fourier transformations for all w are shown in Figure 4.4. Comparing q_x^0 and q_y^0 in Fig. 4.3(b), we observe a slight anisotropy characterized by $q_x^0 > q_y^0$. This means that the SOI is stronger for electrons that move along x and indicates a remaining Rashba field due to a slight asymmetry in the quantum well. The SOI coefficients, α and β, are obtained from q_y^0 and q_x^0 measured in the 1D limit by using the expressions

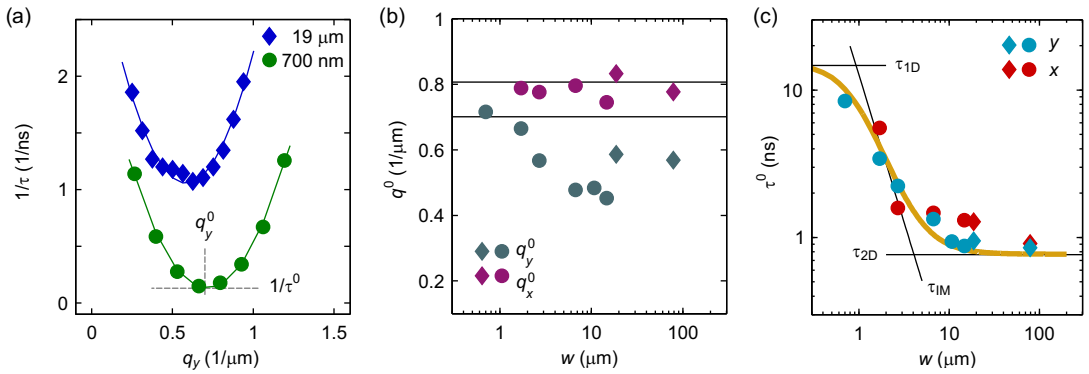

Figure 4.3: Fit results. (a) Decay rates for the 19-μm (diamonds) and 700-nm-wide (dots) channels along the y direction as a function of the wave number, q_y. Data is obtained from fitting to $S_z(q_y, t)$ an exponential decay for $t > 500$ ps, thus corresponding to the long-lived mode. Solid lines are parabolic fits of the decay rate versus q, from which the position, q_y^0, and the lifetime, τ^0, of the evolving spin mode are obtained. (b) Values for the spin mode wave numbers q_x^0 and q_y^0, shown for measurements at various channel widths, w, along the x and y direction. (c) Lifetime of spin modes, τ^0, as a function of w and for both channel directions. Solid black lines are the theoretically expected lifetimes. The yellow solid line is their interpolation. In all three plots, circles (diamonds) stand for fit values obtained from 1D (2D) Fourier transformations.

$$q_{\mathrm{y}}^0 = \left| \frac{2m^*}{\hbar^2} (\alpha + \beta^*) \right| \approx 0.7\ \mu\mathrm{m}^{-1}, \text{ and}$$
$$q_{\mathrm{x}}^0 = \left| \frac{2m^*}{\hbar^2} (\alpha - \beta^*) \right| \approx 0.8\ \mu\mathrm{m}^{-1}. \tag{4.2}$$

We find $D_{\mathrm{s}} = 50$ cm^2/s, $\alpha = -0.3 \times 10^{-13}$ eVm and $\beta_1 = 4.9 \times 10^{-13}$ eVm. Here, we assumed $\beta_3 = -\gamma\pi n_{\mathrm{s}}/2 = 0.6 \times 10^{-13}$ eVm (see Chapter 2). These values are based on the assumption that the Dresselhaus SOI is dominating over Rashba SOI. This is justified by the sample design, which intentionally minimized the electric field perpendicular to the quantum well. However, we can also provide an experimental proof for the assumption at the end of this section. The dependence of q_x^0 on w is rather flat, whereas q_y^0 decreases for increasing w. This is in agreement with the prediction that q_y^0 of the 2D spin mode is smaller for slightly anisotropic SOI than expected from Eq. (4.2) [27, 28]. Close to the PSH situation, the same effect leads to a suppression of precession along y. The lifetime, τ^0, however, behaves almost identically for both wire directions and increases by about one order of magnitude from $w = 19$ μm to 700 nm.

It was pointed out by theorists that wire confinement can only suppress the spin dephasing due to linear terms of the SOI [74, 84]. The cubic term, because of its 3θ dependence [cf. Eq. 2.13], will remain limiting in a wire within the diffusive

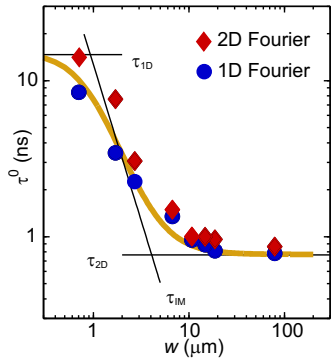

Figure 4.4: Comparison of radial and linear Fourier transformation. Experimental values of τ^0 as obtained by 2D (diamonds) and 1D (circles) Fourier transformations of $S_z(y,t)$. Also shown are the theoretical values of τ_{1D}, τ_{2D} and τ_{IM}, as well as their interpolation.

regime [74, 84]. As we will show in Section 4.5, the lifetime in the 1D limit, $\tau_{1\mathrm{D}}$, is the same as in the PSH case [31] and given by

$$\tau_{1\mathrm{D}}^{-1} = 6\frac{D_{\mathrm{s}} m^{*2}}{\hbar^4}\beta_3^2\,. \tag{4.3}$$

The theoretically expected values for $\tau_{2\mathrm{D}}$ (see Chapter 2.3.1), τ_{IM} and $\tau_{1\mathrm{D}}$ are plotted in Fig. 4.3(c) as black lines. As a guide to the eye, we plot $\tau_{2\mathrm{D}} + \left(\tau_{\mathrm{IM}}^{-1} + \tau_{1\mathrm{D}}^{-1}\right)^{-1}$ [yellow line in Fig. 4.3(c)]. The agreement of this interpolation with the experimental data is very good. Although τ^0 towards smaller w is not yet saturated, it is possible to project that cubic SOI will limit the lifetime.

The question remains which of Eqs. (3.6) or (3.5) to apply for wires in the transition between 2D and 1D, as none is strictly correct. Figure 4.4 shows τ^0 along the y-direction determined by both, 1D and 2D Fourier transformations. We see that the deviation between the two models in the intermediate regime is not significant. In Fig. 4.3, we plot the 2D transformation for $w \geq 15$ μm and the 1D transformation for narrower channels.

From q_x^0 and q_y^0 given in Eq. (4.2), we derived values for α and β_1 under the assumption that $\alpha < 0$. In the following an experimental proof for this assumption shall be given. For that, we apply an external magnetic field of $B_{\mathrm{ext}} = 1$ T perpendicular to the wire direction. Fig. 4.5 shows maps measured under this condition on wires along the x and y direction with an external magnetic field of 1 T applied along the y and $-x$ direction, respectively. Without SOI, the spins would only precess with a frequency $g\mu_{\mathrm{B}}B_{\mathrm{ext}}/\hbar$. This would result in perpendicular lines of constant spin precession phase in the plots of Fig. 4.5. Instead, we observe a precession pattern tilted with respect to the spatial axis [37]. This is caused by SOI. The spin-orbit field superposes to B_{ext}. Looking at Fig. 2.2, we see that, for

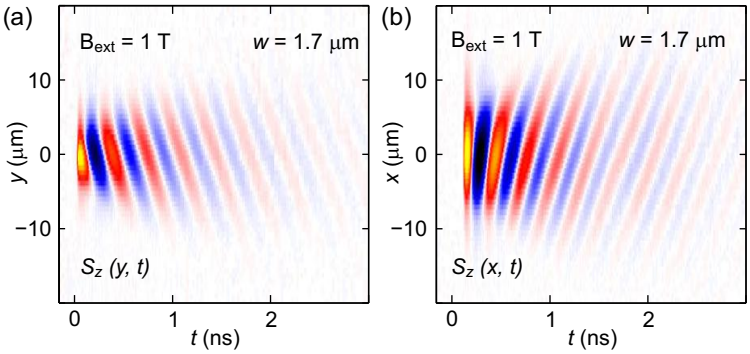

Figure 4.5: Spin maps at an external magnetic field. (a) $S_z(y,t)$ in a 1.7-μm-wide wire along the y direction at an external magnetic field of $B_{\text{ext}} = 1$ T along the $-x$ direction. The sample temperature is 30 K. (b) $S_z(x,t)$ in a 1.7-μm-wide wire along the x direction at an external magnetic field of $B_{\text{ext}} = 1$ T along the $+y$ direction. The sample temperature is 10 K. The magnetic field induces additional spin precession in time. The tilted lines of constant phase show the helical nature of the precession pattern. From the similar strength but opposite signs of the tilts in the (x,t) and the (y,t) planes, it is concluded that $|\beta^*| > |\alpha|$. However, the tilt in (b) is slightly stronger than in (a), which means that α is negative.

the symmetry chosen, the linear spin-orbit fields are parallel to B_{ext} for $\mathbf{k}$ parallel to the wire direction. Furthermore, the spin-orbit field for spins moving along the positive spatial direction is always opposite to the one for spins moving along the negative spatial direction. The precession of the spins in the superposition of B_{SOI} and B_{ext}, thus, causes the tilt observed. The analysis of the maps in Fig. 4.5 gives two results. One is that the slope of the tilt is slightly steeper in Fig. 4.5(b) than in Fig. 4.5(a). This means that $B_{\text{SOI}}(k_x) > B_{\text{SOI}}(k_y)$. Referring to Fig. 2.2, this is only possible if $\beta^* - \alpha > \alpha + \beta^*$, i.e. that $\alpha < 0$. The second result is that the slope in Fig. 4.5(a) is negative, while in Fig. 4.5(b) it is positive. If the SOI were dominated by Rashba SOI, the tilt would always have the same slope. In conclusion, the quantum well is dominated by Dresselhaus SOI and $\alpha < 0$. Another insight can be drawn from the data in Fig. 4.5. The external magnetic field rotates the in-plane spin component [$S_y(t)$ and $S_x(t)$, respectively] out-of-plane. Therefore, these measurements prove the helical nature of the precession pattern in the 1D limit [37].

In conclusion, we measured the evolution of a local spin excitation in a GaAs/AlGaAs quantum well dominated by linear Dresselhaus SOI. The lateral confinement leads to an increased correlation between the electron position and the spin precession angle. Using a real-space mapping of the time-resolved spin distribution, we observe a transition to a helical precession pattern accompanied by an enhanced lifetime for decreasing channel width. The transition occurs for a channel width close to the spin-orbit length. The analysis in Fourier space shows that the long-

lived components decay exponentially with a minimum rate at a finite q^0. Both, the precession length and the lifetime are in quantitative agreement with theory for the 2D limit, the 1D limit, and also for the intermediate regime.

4.4 Persistent spin helix regime: transition to one-dimensional diffusion

In the previous section, we have seen that wire confinement, for isotropic SOI, leads to a transition of the intrinsic precession pattern from a Bessel function to a helical state described by a cosine oscillation of the out-of-plane spin density. This is, however, not the only possible realization of such a long-lived helical spin state. The combination of Rashba and Dresselhaus SOI of equal strength leads to a uniaxial SO field, giving rise to the PSH state (see Section 2.3.2).

As in the wire case, the spin dephasing time is limited only by cubic-in-k terms of the SOI. Wire confinement is, thus, not expected to enhance the spin dephasing time any further in the case of perfect PSH symmetry. However, we know from Eq. (3.2) that there are also other terms that lead to a reduction of the local

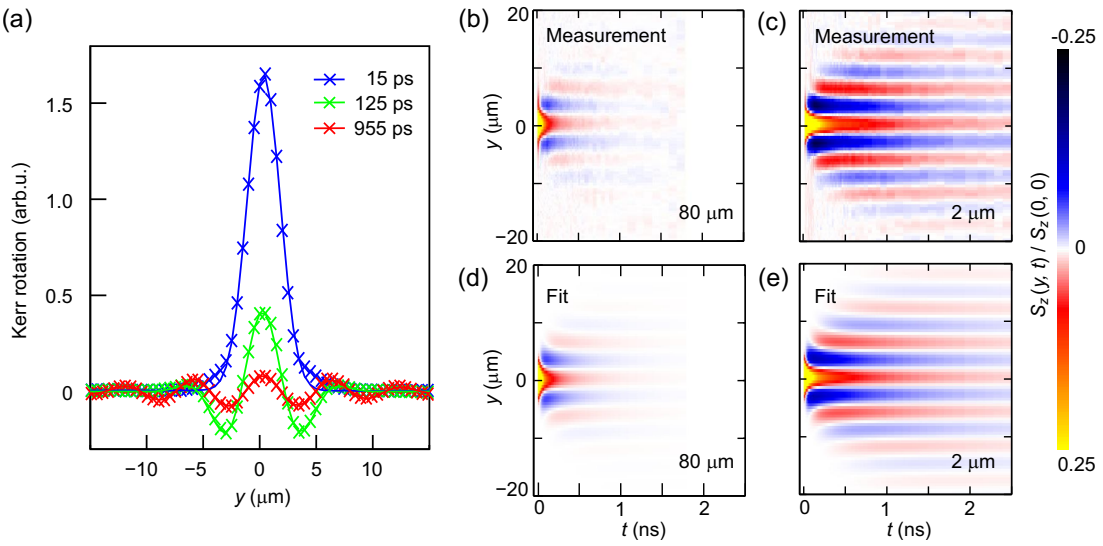

Figure 4.6: Measurements and fits of $S_z(y,t)$. (a) Scans of time-resolved Kerr rotation measured along y on the 2-μm-wide wire (crosses) for 3 different time delays. The oscillations visible at $t = 125$ and 955 ps show the formation of a spin helix mode. Lines are fits with a Gaussian times a cosine function. (b) and (c) show 2D plots of the line scans against the time delay between pump and probe pulse. The widest wire, 80 μm, is shown in (b) and the thinnest, 2 μm, in (c). The color scale codes the out-of-plane spin polarization $S_z(y,t)$ normalized to its maximum value $S_z(0,0)$. (d) and (e) show corresponding fits with the model of Eq. (4.4).

spin polarization. In a 2D system, the diffusive dilution of electrons after local excitation (see Section 2.2) leads to a decay of the local spin density, which is proportional to $(2D_s t)^{-1}$. In one dimension, the solution of the diffusion equation yields a decay, which only goes with $(2D_s t)^{-1/2}$, and, therefore, we expect that wire confinement can further suppress the spin decay in a PSH situation. To distinguish between an enhancement of the lifetime τ_{PSH} of the helical eigenmode and a transition to 1D diffusion, we modify the analytical model of Eq. 3.2 by introducing the dimensionality factor *dim* and fitting it to the data:

$$S_z(y,t) = S_z(0,0) \cdot \cos\left(q_0 y \cdot \frac{2D_s t}{\sigma_0^2 + 2D_s t}\right) \cdot \exp\left(-\frac{y^2}{2(\sigma_0^2 + 2D_s t)}\right) \cdot A_{\mathrm{diff}}(t) \cdot A_{\mathrm{add}}(t) \cdot A_{\mathrm{dec}}(t), \quad (4.4)$$

with

$$A_{\mathrm{diff}}(t) = \left(\frac{\sigma_0}{\sqrt{\sigma_0^2 + 2D_s t}}\right)^{dim}, \quad (4.5)$$

$$A_{\mathrm{add}}(t) = \exp\left(-D_s q_0^2 \frac{\sigma_0^2}{\sigma_0^2 + 2D_s t} t\right), \quad (4.6)$$

$$A_{\mathrm{dec}}(t) = \exp\left(-\frac{t}{\tau_{\mathrm{PSH}}}\right). \quad (4.7)$$

In addition to $A_{\mathrm{dec}}(t)$, describing the exponential decay of the PSH eigenmode, the terms $A_{\mathrm{add}}(t)$ and $A_{\mathrm{diff}}(t)$ contribute to the signal decay. $A_{\mathrm{add}}(t)$ arises because of the finite sized pump and probe spots (see Sections 2.3.2 and 3.4). For $\sigma_0 \to 0$, $A_{\mathrm{add}} \to 1$. For 2D diffusion, $dim = 2$ and for 1D diffusion, $dim = 1$.

Figure 4.6(a) shows Kerr-rotation measurements as a function of the relative distance y along the wire between the pump and probe spots and for different time delays, t, recorded at the transverse center position $x = 0$ on the 2-μm wire. At $t = 15$ ps, $S_z(y)$ resembles the Gaussian intensity profile of the laser spots, although broadened by diffusion. The measurement at $t = 955$ ps exhibits a cosine oscillation of $S_z(y)$, a direct signature of the spin helix. For all times, the data can be very well fitted [solid lines in Fig. 4.6(a)] by a product of a cosine and a Gaussian that broadens in time owing to diffusion.

Figures 4.6(b) and 4.6(c) show color-scale plots of the temporal evolution of line scans along wires of 80 μm and 2 μm width. Both, diffusive broadening as well as spin helix formation can be seen. Whereas for both wires the signal decays with time, the visibility of the PSH in the 2-μm-wide wire is largely enhanced at longer times.

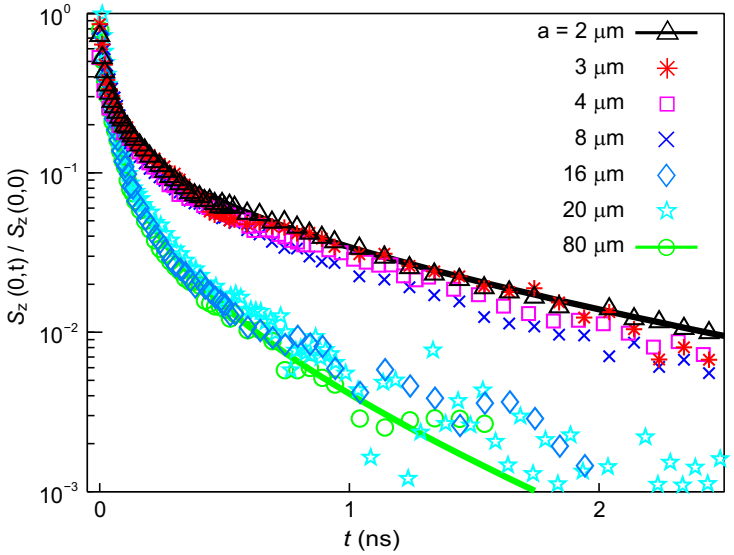

Figure 4.7: Decay of $S_z(0,t)$ for different wire widths a. Symbols show the amplitude of individual fits to line scans [see Fig. 4.6(a)], whereas the solid lines exemplarily show global fits according to Eq. (4.4) for the 80-μm and the 2-μm wires.

We fit Eq. (4.4) to the data $S_z(y,t)$ and show the results for the 80-μm and 2-μm wires in Figs. 4.6(d) and (e). The model reproduces the measurements very well. Fit parameters are the initial distribution width σ_0, the PSH wave number q_0, the diffusion constant D_s, the maximum amplitude $S_z(0,0)$, the PSH lifetime τ_{PSH}, and the dimensionality factor dim. See Section A.4 for details on the fitting procedure. Figure 4.7 shows the temporal evolution of the normalized amplitude, $S_z(0,t)/S_z(0,0)$, for all wire widths. The solid lines are obtained from fits of the full data set, $S_z(y,t)$, with Eq. (4.4). For better readability, we only show the results for the widest and the narrowest wire. The symbols are the results obtained from fitting individual line scans, as depicted in Fig. 4.6(a). As the results of both fitting methods coincide very well for all wires, we conclude that the model of Eq. (4.4) captures all relevant decay mechanisms. For all curves, the decay in the first few hundred picoseconds is dominated by the additional decay terms, Eqs. (4.5) and (4.6). The exponential decay term, which appears linear in the semi-logarithmic plot of Fig. 4.7 dominates for $t > 500$ ps. Two groups of wires can be distinguished: In wires narrower than 8 μm, the Kerr signal decays significantly slower than in the other wires.

Figure 4.8(a) shows the fit parameter dim obtained from Eq. (4.4). A clear transition to 1D diffusion is observed for wires narrower than 8 μm. Comparing with Fig. 4.7, this indeed corresponds to the group of wires with suppressed decay. The transition to 1D diffusion occurs when the width of the spin distribution becomes comparable to w. In the experiment presented, the spin distribution

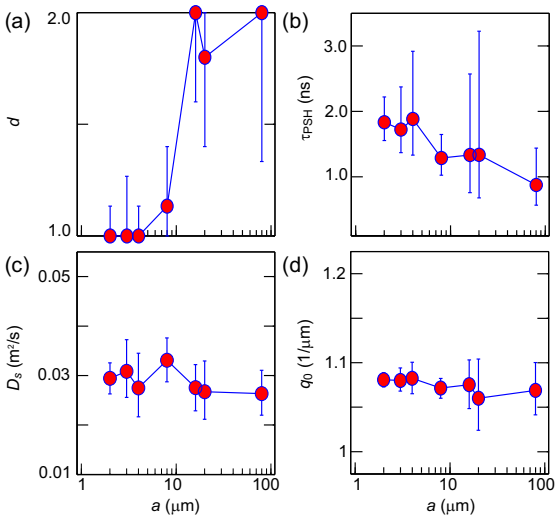

Figure 4.8: Fit parameters plotted against the wire width, w. (a) Wires narrower than 8 μm are identified as 1D. To obtain the parameters shown in (b) to (d), *dim* was fixed to 2 for wires wider than 8 μm and to 1 for the others. (b) The PSH lifetime, τ_{PSH}, increases slightly with decreasing wire width. (c) and (d) show the spin diffusion constant D_{s} and the helix wavenumber q_0, respectively. Both parameters do not change with w.

has an initial sigma width of $\sigma \approx 1.5$ μm (determined by fitting). Accordingly, wires with $w \leq 4$ μm can be expected to show 1D diffusion from the beginning in accordance with the fit results. In addition, in the 8-μm wire, diffusive broadening leads to a transition from 2D to 1D diffusion after $t \approx [(w/2)^2 - \sigma^2]/2D_{\mathrm{s}} \approx 0.25$ ns, making this wire predominantly 1D in our fit. The strong suppression of diffusive spin decay in 1D wires results in one order of magnitude stronger signal after 2 ns [see Fig. 4.7].

For the determination of the other fit parameters [see Figs. 4.8(b)-(d)], *dim* is fixed to 1 (2) for $w \leq 8$ μm ($w \geq 16$ μm). No influence on q_0 can be found, as can be seen from Fig. 4.8(d), meaning that the SOI is unchanged between narrow and wide wires with $q_0 = 1.05$ $\mu\mathrm{m}^{-1}$, corresponding to $l_{\mathrm{SO}} = 6.0$ μm. Furthermore, also D_{s} is unaffected [Fig. 4.8(c)]. Hence, the spin scattering rate is not significantly enhanced by diffusive scattering at the wire edges. At the same time, a significant reduction of n_{s} in narrow wires can be excluded, as this would also affect D_{s} and q_0.

In addition to the strong suppression of spin decay induced by a transition to 1D diffusion, we find that τ_{PSH} slightly increases for decreasing wire width [see Fig. 4.8(b)]. The increase is, however, not as dramatic as for the case of isotropic SOI in Section 4.3. To understand why the observed increase of the spin dephasing time does not scale with $(l_{\mathrm{SO}}/w)^2$, we need to consider that this prediction is the outcome of a correlation of the motion of spin polarization on the Bloch sphere

with the spatial motion of the diffusing electrons [85]. The cubic Dresselhaus term [Eq. (2.11)], which is proportional to β_3, can be decomposed into a contribution that is harmonic in the spherical angle θ of the electron momentum [Eq. (2.12)], and one that is harmonic in 3θ [Eq. (2.13)]. The former can be combined with the linear Dresselhaus contribution into the renormalized parameter $\beta^* = \beta_1 - \beta_3$ and is also suppressed in a laterally confined geometry. The third harmonic component, however, is disturbing the correlation between spin polarization and spatial position. Because of this detrimental effect, channel confinement can not strongly suppress this decay rate in the diffusive limit. In the investigated quantum well without wire confinement, τ_{PSH} is limited to a large extent by the third-harmonic cubic Dresselhaus contribution [37]. Thus, the observed small increase of τ_{PSH} is compatible with a suppression of the decay caused by the imbalance of the linear SOI, $\alpha - \beta^*$. But the lifetime remains limited by the cubic Dresselhaus SOI, β_3.

In this light, the strong increase of the spin lifetime for $w < l_{\mathrm{SO}}$ observed in Refs. [86, 80] must be discussed by taking into account that the laser spot size used in these studies is larger than l_{SO} and the spin diffusion length. Under this condition, the transition to 1D diffusion can not be observed as no significant amount of spins diffuses out of the area sampled by the probe beam. Furthermore, the large beam spots average out the helical precession pattern, leading to a fast decay of the Kerr signal within a timescale defined by the Dyakonov-Perel mechanism [76, 31], which in our sample is on the order of 40 ps. No quadratic dependence of the measured spin decay rate on the wire width is then expected. However, if the wire is oriented perpendicular to the PSH direction, a large spot will see a gradually increasing lifetime for $w < l_{\mathrm{SO}}$ because the wire edges prevent the propagation of a helical spin pattern, and the probe beam only samples spin polarization of the same sign. For $w \ll l_{\mathrm{SO}}$, the measured lifetime will approach τ_{PSH} even for spot sizes larger than l_{SO}, but only for wire directions perpendicular to the helix direction, explaining the anisotropy in the observed spin lifetime [76, 87, 88].

In conclusion, we studied the impact of wire confinement on the decay dynamics of a local spin excitation in a PSH system. A transition to 1D diffusion is observed for wires narrower than 8 μm, with a spin polarization that decays proportionally to $1/\sqrt{t}$ rather than $1/t$ for the 2D case. This leads to a largely enhanced visibility of the PSH at longer times. The spin dephasing time, for the given PSH symmetry, is not significantly enhanced. We observe an increase of τ_{PSH} by about a factor of 2. We argue that this is due to a suppression of imbalance terms $(\alpha - \beta^*)$, but wire confinement can not suppress the decay due to the cubic spin-orbit field of Eq. (2.13) because of its 3θ dependence. After 2 ns, because of the combined benefits of 1D diffusion and suppression of imbalance terms, the spin density is enhanced by a factor of 20 in a 2-μm wire compared with an 80-μm wire.

4.5 The impact of wire confinement for generic spin-orbit interaction

Comparing the results of Sections 4.3 and 4.4, we see that the transition to 1D is accompanied by different signs depending on the symmetry of the SOI. While in the isotropic case, we observe an enhancement of the spin lifetime by an order of magnitude, for PSH symmetry we observe a transition to 1D diffusion. But almost no enhancement of the spin dephasing time is found in the PSH limit. To get a better overview and to understand the impact of wire confinement on the spin dephasing time for generic SOI, we perform numerical simulations of the spin dynamics in a 2D electron gas.

We use a Monte-Carlo method where the positions and spin orientations of 3×10^5 electrons are updated in time steps of 0.1 ps. Electrons are distributed on a Fermi circle and scatter isotropically, with the mean scattering time given by $\tau = 2D/v_\mathrm{F}^2$, where $v_\mathrm{F} = \hbar k_\mathrm{F}/m^*$ is the Fermi velocity. Each electron moves with the Fermi velocity and sees an individual spin-orbit field as defined in Eq. 2.11 that depends on its velocity direction. The real-space coordinates and the corresponding spin dynamics are calculated semiclassically. We initialize the electrons at $t = 0$ all with their spins oriented along the z direction and distribute their coordinates in a Gaussian probability distribution with a center at $x = y = 0$ and a σ-width of 500 nm. Histograms of the electron density and the spin orientations are recorded every 5 ps, and the simulation is run until $t = 5$ ns is reached. We obtain the spin polarization at $x = y = 0$ versus t from the spin-density maps using a convolution with an assumed Gaussian probe spot size of 500 nm. For the data shown in Fig. 4.9, we have used the following parameters: $D_\mathrm{s} = 0.004$ m^2/s, $n_\mathrm{s} = 3.4{\times}10^{15}$ cm^{-2}, $\beta_1 = 4.9 \times 10^{-13}$ eVm and $\beta_3 = 0.6 \times 10^{-13}$ eVm. Lateral confinement was implemented by assuming specular scattering at the channel edges. For the 1D case, $w = 400$ nm was used.

The diffusive dilution of electrons in 2D scales with $1/t$ and in 1D with $1/\sqrt{t}$. We determine the spin lifetimes τ^0 by fitting the transients with a function proportional to $1/t \times \exp -t/\tau^0$ or $1/\sqrt{t} \times \exp -t/\tau^0$ in a window 800 ps $< t <$ 4000 ps, where additional spin decay is negligible because of the small spot sizes [31]. Interestingly, the spins in a 2D system, however, also decay with $1/\sqrt{t}$ for the isotropic SOI case [27, 32].

The lifetime enhancement achievable by wire confinement depends strongly on the ratio α/β^*. Figure 4.9 shows lifetimes determined by Monte-Carlo simulations for $-1.1 < \alpha/\beta^* < 1.1$. The lines are the theoretically expected values of τ^0 for 2D spin modes (τ_PSH, τ_2D), the 1D spin mode (τ_1D), as well as for the DP case (τ_DP). Interestingly, Eq. (2.24) provides a good approximation of the spin lifetime also further away from $\alpha \approx \beta^*$. We find that in a narrow channel (red

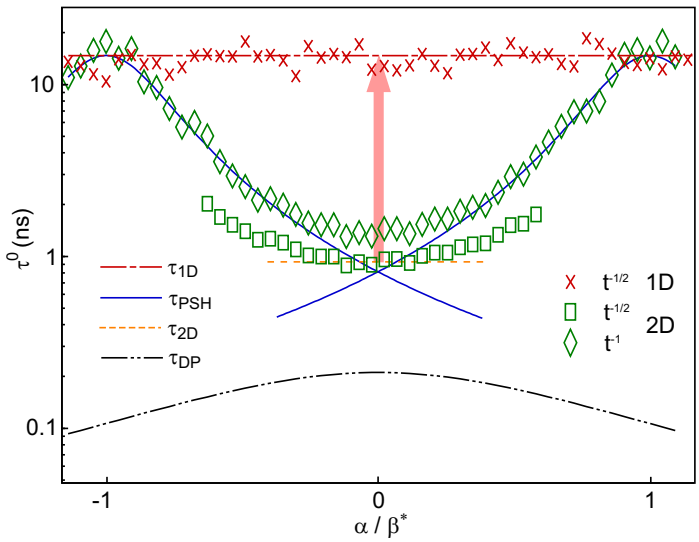

Figure 4.9: Spin lifetimes for the 1D and 2D situation as determined from Monte-Carlo simulations for various ratios of $-1.1 < \alpha/\beta^* < 1.1$. Data is obtained by fitting $S_z(y,t)$ with a model that includes a diffusive dilution proportional to either $1/t$ (diamonds) or $1/\sqrt{t}$ (rectangles and crosses). The red, blue, orange and black lines are theoretical curves for τ_{1D}, τ_{PSH}, τ_{2D} and τ_{DP}, respectively. In the 1D case, the lifetime is limited by the cubic SOI only, as in the 2D case at $|\alpha| = |\beta^*|$.

crosses in Fig. 4.9), τ^0 does not depend on α or β_1 and is limited by cubic SOI only. The same limit is reached in the 2D situation (green symbols in Fig. 4.9) at $|\alpha| = |\beta^*|$, i.e. when the system is tuned to the PSH symmetry. The highest lifetime enhancement under lateral confinement in the diffusive limit occurs for the isotropic case ($\alpha = 0$). As we have seen in Section 4.4, close to $|\alpha| = |\beta^*|$, the lifetime enhancement is small, but a reduction of diffusive dilution was observed.

4.6 Outlook: ballistic and quantized regime

With photo-lithography, as explained in Section 4.2, it is only possible to define wire structures of widths of about 1 μm. Because in our quantum wells the mean-free path is typically on the order of 0.2 μm, electrons can not travel from one sidewall to the opposite sidewall without scattering. The system remains in the diffusive limit and the electrons still equally sample all k-states on the Fermi circle. We argued in the previous section that the cubic Dresselhaus term (Eq. 2.11) has a component that is harmonic in 3θ [15] and that it is this component of the SOI, which is not affected by wire confinement and limits the spin dephasing time in the 1D limit.

However, for the ballistic regime, assuming specular scattering at the sidewall, a

further increase of the spin dephasing time is expected [84, 89]. That is because the k vector component perpendicular to the wire axis then reverses its sign repeatedly as the electron travels along the wire [75]. Also for the symmetry of the 3θ-term, this means the experienced spin-orbit field reverses its sign, such that pro- and counter-rotation of the spin approximately compensate each other. A procedure for the production of narrower wires by e-beam lithography and dry etching in a ICP-RIE is given in Appendix A.1.2.

When the wire width approaches the Fermi wavelength, the electronic system becomes one-dimensionally quantized. It is predicted that the spin dephasing time then depends on the number of conduction channels [89].

Chapter 5

Drift and diffusion of spins in a cubic spin-orbit field

As we know from Section 2.3, a local spin excitation evolves into a spatial precession pattern in the presence of SOI. For isotropic SOI, the intrinsic precession pattern is described by a radial Bessel function and for PSH symmetry it is a cosine oscillation along one spatial direction and no precession along the other direction. In any case, we can associate with this spatial precession a spatial wave number q. For isotropic scattering, the electrons randomly sample all k states on the Fermi circle. The spatial precession patterns are a consequence of the precession of electron spins about the spin-orbit effective magnetic field that is associated with each k vector [cf. Eq. (2.11)]. Until now, we considered only diffusive motion of the electrons.

In this chapter, we will explore the impact of drift motion in addition to diffusive motion. Several research groups concluded that the spatial wavenumber q is not affected by drift [16, 90, 91, 92]. In our experiment[1], we observe an unexpected drift-induced spin precession of quasistationary electrons, i.e. of electrons for which forward drift is compensated by backward diffusion. By an analytical model we will identify this temporal precession as an effect of cubic SOI. Such an experiment provides direct access to the cubic terms of the spin-orbit field, which so far could only be indirectly deduced from related quantities, like from the lifetime of a PSH.

In first order approximation, the temporal precession frequency is found to depend linearly on the drift velocity. But as we will present in Section 5.6, there is evidence of a higher-order regime, where not only the temporal precession frequency depends no longer linearly on the drift velocity, but also the spatial wavenumber of the spin mode starts to be affected. This higher-order regime is the basis for the device proposals presented in Chapter 6.

[1] These results have been published in Ref. [93].

5.1 Prior drift experiments

Before we present our measurements, we will recapitulate what is already known about spin precession of drifting electrons. A very early demonstration that an electrical current is suitable to transport spin polarized electrons was presented by Kikkawa and Awschalom in 1999 [25]. The material system of choice was a n-GaAs layer. SOI did not play an important role in this study. It did play an important role, instead, in an experiment presented by Kato et al. [70], where it was demonstrated that spins can be manipulated without magnetic fields thanks to SOI in strained semiconductors. For such systems, strain is particularly interesting because it induces a SOI which is linear in k, while SOI in bulk GaAs otherwise is cubic in k [cf. Eq. (2.6)]. It was spatially resolved, albeit with laser spots as wide as 14 μm, that drifting electron spins precess in presence of such linear-in-k SOI [70]. An overview and theoretical explanation of imaged spin precession under electric, magnetic and strain fields in n-GaAs was presented by Crooker et al. [5, 16]. An important finding of this work is that the observed spatial precession pattern did not vary with applied drift. An external magnetic field, instead, leads to a spatial precession pattern, which varies with the drift velocity. The reason for the latter is simply that the spin precession phase acquired in an external magnetic field is linear in time. Hence, the precession angle at a given distance from the point of spin injection depends on $t = \Delta x / v_{\mathrm{dr}}$.

Drift also plays an important role in the experimental technique described in Section 3.5.1. This approach allows the determination of the Rashba and Dresselhaus parameters in a quantum well [67, 68, 69] when not having high enough spatial resolution to image the intrinsic precession pattern (cf. Section 3.4).

A rather high spin drift velocity of up to 100 km/s was measured by a transient spin grating technique [21, 92]. It has been found that, although the spin diffusion constant differs significantly from the electron diffusion constant (up to a factor of 500 in these studies), the drift mobility of the spin tracks that of the electrons for a wide temperature range up to 150 K.

Other than previous theoretical treatments [94, 95] of spin precession for drift-diffusion in spin-orbit fields, the random walk approach presented by Yang et al. [91] yields solutions for the isotropic as well as the PSH case including the cubic Dresselhaus term. It also includes the first prediction of a drift-dependent phase acquired in the presence of cubic SOI.

A very recent experiment demonstrated that the PSH symmetry is very well suited for spin transport [40]. The known spin lifetime enhancement achieved by tuning the strength of the Rashba SOI to equal the strength of the Dresselhaus SOI was shown to result in long spin transport lengths of up to 5 precession periods. Because in this study the dynamics of the spin transport was obscured by continuous-wave excitation, the potentially present phase-shift that we will

describe in the coming section could not be seen. Furthermore, the impact of cubic SOI was fully neglected in the discussion of the drift behavior and of the PSH dynamics.

5.2 Quantum well design and mesa fabrication

A GaAs quantum well tuned to the PSH symmetry is the most suited system to study nonlinear effects of the SOI for a few reasons. One is that the spin dephasing time is long, which should help to measure an effect that is small and accumulates in time. Another is that many oscillations of the precession pattern in space allow for a precise determination of the spatial wavenumber, q, which further facilitates the fitting of a temporal precession frequency, ω. The quantum well under study is 12 nm wide and has an electron sheet density of $n_s = 5 \times 10^{15}$ m^{-2} and a transport mobility of 22 m^2(Vs)$^{-1}$ at 5 K. Further details on the sample parameters are found in Appendix A.2. The quantum well is close to the PSH condition characterized by strong spin precession along y and suppressed spin precession along x. The sample is from the same wafer as in Ref. [37] and in Section 4.4.

To apply an in-plane electric field and subject the electrons to drift, we fabricated a cross-shaped mesa structure with an ohmic contact at the ends of each arm [cf. inset of Fig. 5.1(c)]. Each arm has a width of 150 μm and opposite contacts are 800 μm apart. One arm is oriented along $y = [110]$, the other along $x = [1\bar{1}0]$. Further details on the processing can be found in Appendix A.1.

5.3 Current-controlled spin precession of quasi-stationary electrons

We will first study the spin precession for drift along y, the PSH direction. We apply scanning Kerr microscopy as explained in Section 3.2. We position the probe in the center of the mesa arm and scan the pump along the drift direction. Figure 5.1(a) shows data for three different time delays, t, at $E_y = 1.56$ kV/m. The spatially precessing spins are well described by a cosine oscillation in a Gaussian envelope that broadens with time because of diffusion. Its center shifts along $-y$ because the electrons drift in the applied electric field. Figs. 5.1(b) and 5.1(c) show colorscale plots of $S_z(y,t)$ for $E_y = 1.56$ kV/m and $E_y = -1.8$ kV/m, respectively. The motion of the center of the spin packet is marked by a violet dashed line. Remarkably, the position of constant spin precession phase shifts along y in time, as indicated by the solid green lines. This corresponds to a finite temporal precession frequency ω for spins that stay at a constant position y. For a positive E_y [Fig. 5.1(b)], the spin packet moves towards the negative y-axis, and

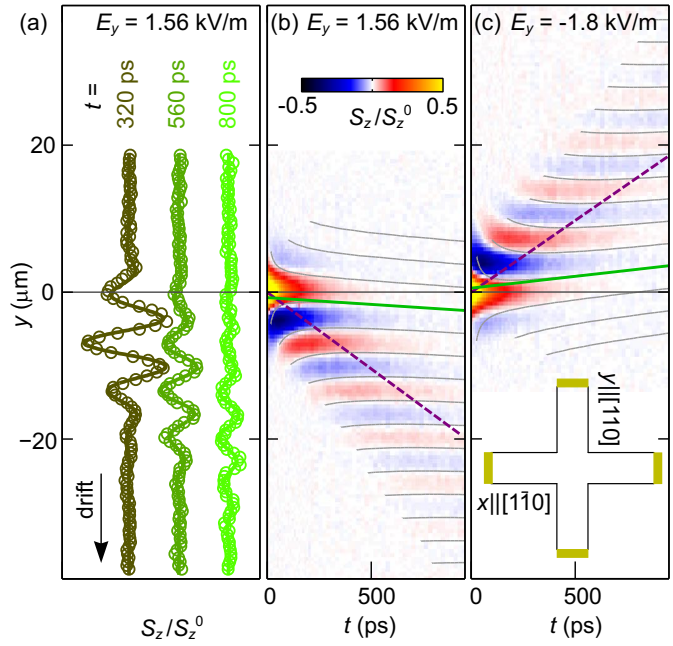

Figure 5.1: Measurement of drifting spins after a local spin excitation at time $t = 0$. (a) Measured spin polarization S_z vs. y for different t at an electric field $E_y = 1.56$ kV/m. The data is offset according to t and normalized to the maximum spin polarization, S_z^0. Circles are experimental data and solid lines are fits with Eq. (5.1). (b) Colorscale plot of $S_z(y,t)$ for $E_y = 1.56$ kV/m. The violet dashed line marks the center of the spin packet. The gray solid lines are contour lines of a global fit as explained in the text. The solid green line indicates the slope of the lines of equal spin phase. It is tilted because spin precession from drift is different from that from diffusion owing to cubic SOI. (c) Colorscale plot of $S_z(y,t)$ for $E_y = -1.8$ kV/m, where the slope of the green line is reversed. Inset: schematic layout of the cross-shaped mesa structure. Four ohmic contacts allow the application of electric fields along the $y||[110]$ and the $x||[1\bar{1}0]$ direction.

the tilt $\partial y/\partial t$ of constant spin phases is negative. Both, the drift direction and the tilt, change their sign when the polarity of E_y is reversed [Fig. 5.1(c)].

We model S_z by multiplying the Gaussian envelope by $\cos(qy+\omega t)$ and a decay factor $\exp(-t/\tau)$, and by introducing the drift velocity v_{dr}:

$$S_z(y,t) = \frac{A_0}{2D_{\mathrm{s}}t} \exp\left[\frac{-(y-v_{\mathrm{dr}}t)^2}{4D_{\mathrm{s}}t}\right] \cos(\omega t + qy) \exp(-t/\tau)\,. \tag{5.1}$$

The amplitude A_0, v_{dr}, the diffusion constant D_{s}, the dephasing time τ, ω and q are treated as fit parameters. The decrease of the spatial precession period in time is a known effect of the finite size of the pump and probe laser spots [31], and is accounted for by convolving Eq. (5.1) with the Gaussian intensity profiles of the

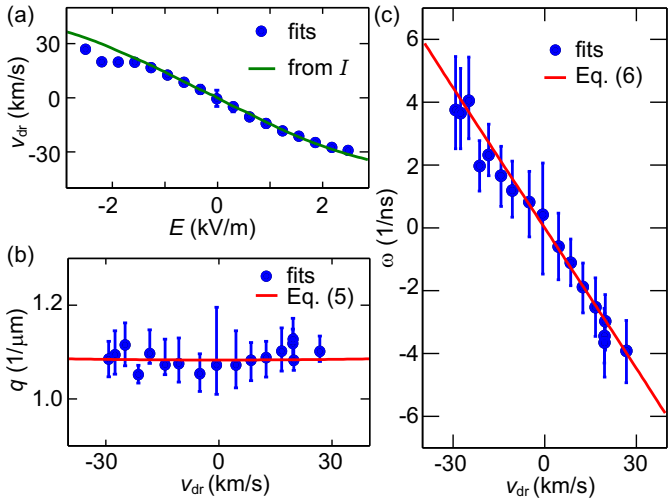

Figure 5.2: Fit results. (a) Drift velocity v_{dr} plotted against the applied electric field. Dots are the fit values obtained from the measured $S_z(y,t)$. The solid line is the drift velocity calculated from the measured current I via $v_{\mathrm{dr}} = I/(en_{\mathrm{s}}w)$. (b) Values for the spatial wavenumber, q. Dots are the fit values and the red line is the model of Eq. (5.8) with $\alpha + \beta^* = 6.2 \times 10^{-13}$ eVm. (c) Values for the precession frequency, ω. Dots are fit values and the red line is the model of Eq. (5.9) with $\beta_3 = 8.5 \times 10^{-14}$ eVm. Confidence intervals in all plots are defined as a 5% increase of the fit error.

laser spots. As explained in Section 3.3.3, a 1D Fourier transformation is only valid in the limit $2D_{\mathrm{s}}t \gg \sigma_0^2$. We fit the data for $t > 300$ ps. Besides that, the experiment is perfectly described by this model, as evident from the good overlap of the symbols (experiment) with the solid lines (fits) in Fig. 5.1(a), and from the fitted gray lines that mark $S_z(y,t) = 0$ in the colorscale plots of Figs. 5.1(b-c).

The fit parameters obtained for different values of E_y are shown in Fig. 5.2. In Fig. 5.2(a), v_{dr} obtained from $S_z(y,t)$ is compared with values deduced from the measured current I using $v_{\mathrm{dr}} = I/(en_{\mathrm{s}}w)$, where e is the elementary electron charge. The good agreement shows that the spin packet follows the stream of drifting electrons in the channel and that no parallel conductance obscures the interpretation of our data. In Figs. 5.2(b-c), we summarize the values obtained for q and ω. While q shows no dependence on v_{dr}, we find a linear dependence of ω on v_{dr} with a negative slope.

5.4 The difference between drift and diffusion

Next, we show that the drift-induced ω is a consequence of cubic SOI. Considering a degenerate 2DEG in a (001)-oriented QW with one occupied subband, the k-dependent spin-orbit field $\mathbf{B}_{\mathrm{SO}}$ is given by Eq. (2.11). Figure 5.3(a) sketches two different diffusive paths of electrons that travel the same distance $\hbar\mathbf{k}_{\mathrm{di}}t/m^*$. On

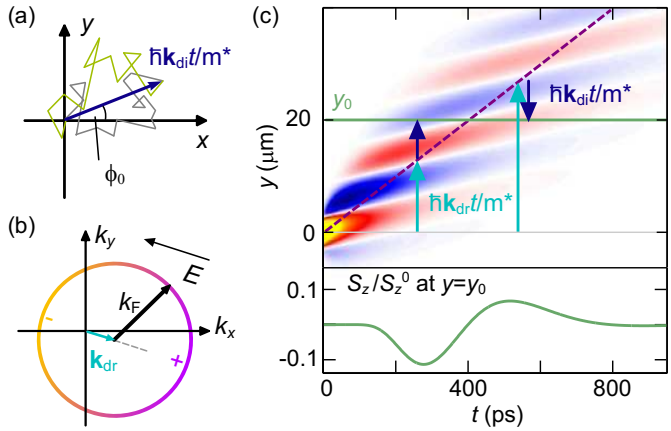

Figure 5.3: Model of drift and diffusion. (a) Scattering events lead to diffusive trajectories of individual electrons. Shown are two trajectories of electrons that travel the same distance $\hbar\mathbf{k}_{\mathrm{di}}t/m^*$. (b) The Fermi circle is shifted by the drift vector $\mathbf{k}_{\mathrm{dr}}$. (c) Exemplary map of $S_z(y,t)$ generated from Eq. (5.1). Electrons with an average $\mathbf{k}_{\mathrm{di}} = 0$ drift along the violet dashed line. Electrons measured away from this line additionally experience a diffusive motion. Because of the unequal contributions of drift and diffusion to spin precession, the phase of quasi-stationary electron spins (for example, those on the solid green line) depends on how the travel is divided between drift and diffusion. This leads to a precession in time, as seen in the lower panel (shown for spins at $y = y_0$).

these paths, the electrons scatter many times and thereby sample different k states. Because we consider electrons that travel along $\mathbf{k}_{\mathrm{di}}$, they occupy states with k vectors along $\mathbf{k}_{\mathrm{di}}$ more often than along the opposite direction. Assuming isotropic scattering, this occupation is modeled by a weighting function

$$f(\theta) = 1 + \frac{2k_{\mathrm{di}}}{k_{\mathrm{F}}}\cos(\theta - \phi_0)\,, \tag{5.2}$$

such that the average momentum is $\hbar/(2\pi)\int_0^{2\pi}\mathbf{k}f(\theta)\,\mathrm{d}\theta = \hbar\mathbf{k}_{\mathrm{di}}$, with $\mathbf{k} = k(\cos\theta, \sin\theta)$ and $\mathbf{k}_{\mathrm{di}} = k_{\mathrm{di}}(\cos\phi_0, \sin\phi_0)$. The drift of the electron gas is accounted for by a shift of the Fermi circle by $\mathbf{k}_{\mathrm{dr}}$ [Fig. 5.3(b)]. Because of its dependence on k, the SOI field changes after each scattering event. Its average is given by $\langle\mathbf{B}_{\mathrm{SO}}\rangle = \int_0^{2\pi} d\theta\,\mathbf{B}_{\mathrm{SO}}(\mathbf{k}+\mathbf{k}_{\mathrm{dr}})\,f(\theta)$, in analogy to Eq. (3.8). Instead of deriving the intrinsic precession pattern of the system [27, 91], we describe the spin dynamics by assuming that spins injected at $t = 0$ and $x = y = 0$ precess about

$$\langle\mathbf{B}_{\mathrm{SO}}\rangle = \langle\mathbf{B}_{\mathrm{SO},1}\rangle + \langle\mathbf{B}_{\mathrm{SO},3}\rangle\,, \tag{5.3}$$

with a term proportional to β_1:

$$\langle\mathbf{B}_{\mathrm{SO},1}\rangle = \frac{2\beta_1}{g\mu_{\mathrm{B}}}\begin{pmatrix} k_{\mathrm{di},y} + k_{\mathrm{dr},y} \\ k_{\mathrm{di},x} + k_{\mathrm{dr},x}\end{pmatrix}\,, \tag{5.4}$$

and one proportional to β_3:

$$\langle \mathbf{B}_{\mathrm{SO},3} \rangle = \frac{2\beta_3}{g\mu_\mathrm{B}} \begin{pmatrix} -k_{\mathrm{di},y} - 2k_{\mathrm{dr},y} + \frac{2}{k_\mathrm{F}^2}\left[k_{\mathrm{di},x}k_{\mathrm{dr},x}^2 + 2k_{\mathrm{di},x}k_{\mathrm{dr},x}k_{\mathrm{dr},y} + k_{\mathrm{dr},x}^2 k_{\mathrm{dr},y} - 3k_{\mathrm{di},y}k_{\mathrm{dr},y}^2 - k_{\mathrm{dr},y}^3\right] \\ -k_{\mathrm{di},x} - 2k_{\mathrm{dr},x} + \frac{2}{k_\mathrm{F}^2}\left[k_{\mathrm{di},x}k_{\mathrm{dr},y}^2 + 2k_{\mathrm{di},y}k_{\mathrm{dr},y}k_{\mathrm{dr},x} + k_{\mathrm{dr},y}^2 k_{\mathrm{dr},x} - 3k_{\mathrm{di},x}k_{\mathrm{dr},x}^2 - k_{\mathrm{dr},x}^3\right] \end{pmatrix}. \tag{5.5}$$

For simplicity, we assumed $\alpha = 0$ in the above expressions. We now move to the special case where the electric field is applied along the y direction, such that $k_{\mathrm{dr},x} = 0$, and obtain

$$\langle \mathbf{B}_{\mathrm{SO},3} \rangle = -\frac{2\beta_3}{g\mu_\mathrm{B}} \begin{pmatrix} k_{\mathrm{di},y}\left[1 + 6\left(\frac{k_{\mathrm{dr},y}}{k_\mathrm{F}}\right)^2\right] + 2k_{\mathrm{dr},y}\left[1 + \left(\frac{k_{\mathrm{dr},y}}{k_\mathrm{F}}\right)^2\right] \\ k_{\mathrm{di},x}\left[1 - \left(\frac{2k_{\mathrm{dr},y}}{k_\mathrm{F}}\right)^2\right] \end{pmatrix}. \tag{5.6}$$

To describe a measurement where spins are tracked along the drift direction y and at $x = 0$, we additionally set $k_{\mathrm{di},x} = 0$. It is easy to show that the Rashba field and the Dresselhaus field for this drift direction add up, such that we obtain

$$\langle \mathbf{B}_{\mathrm{SO}} \rangle = \frac{2(\alpha+\beta_1)}{g\mu_\mathrm{B}} \begin{pmatrix} k_{\mathrm{di},y} + k_{\mathrm{dr},y} \\ 0 \end{pmatrix} - \frac{2\beta_3}{\hbar} \begin{pmatrix} k_{\mathrm{di},y}\left[1 + 6\left(\frac{k_{\mathrm{dr},y}}{k_\mathrm{F}}\right)^2\right] + 2k_{\mathrm{dr},y}\left[1 + \left(\frac{k_{\mathrm{dr},y}}{k_\mathrm{F}}\right)^2\right] \\ 0 \end{pmatrix}. \tag{5.7}$$

This is a surprising result, because in the last term, which is proportional to β_3, drift ($k_{\mathrm{dr},y}$) leads to a spin precession angle twice as large as that induced by diffusion ($k_{\mathrm{di},y}$). As illustrated in Fig. 5.3(c), this leads to a precession in time for spins located at a constant position y_0. Without diffusion, the electrons follow $y = \hbar k_{\mathrm{dr},y} t/m^*$ (violet dashed line) and reach $y = y_0$ at a given time. Spins that reach y_0 earlier (later) will in addition diffuse along (against) $\mathbf{k}_\mathrm{dr}$ and therefore acquire a different precession phase. To calculate the corresponding frequency ω, we insert $y = \frac{\hbar}{m^*}(k_{\mathrm{dr},y} + k_{\mathrm{di},y})t$ into Eq. (5.7) and obtain $S_z(y,t) = \cos\left(\frac{g\mu_\mathrm{B}}{\hbar}\langle \mathbf{B}_{\mathrm{SO}} \rangle t\right) = \cos\left(\omega t + qy\right)$, with

$$q = \frac{2m^*}{\hbar^2}\left(\alpha + \beta_1 - \beta_3\left[1 + 6\left(\frac{k_{\mathrm{dr},y}}{k_\mathrm{F}}\right)^2\right]\right) \approx \frac{2m^*}{\hbar^2}(\alpha + \beta^*) \tag{5.8}$$

and

$$\omega = -\frac{2m^*}{\hbar^2} v_{\mathrm{dr}} \beta_3 \left[1 - 4 \left(\frac{k_{\mathrm{dr},y}}{k_{\mathrm{F}}} \right)^2 \right] \approx -\frac{2m^*}{\hbar^2} v_{\mathrm{dr}} \beta_3 \,. \tag{5.9}$$

Higher order terms are not observed in this experiment and we will stick to the first order approximation. They will be discussed in Section 5.6. The wavenumber q is not modified by drift to first order. In contrast, the precession frequency ω depends linearly on v_{dr} and is proportional to the cubic Dresselhaus coefficient, β_3. This induces a temporal precession for quasi-stationary electrons [cf. lower panel in Fig. 5.3(c)]. The tilt of the green solid lines in Figs. 5.1(b-c) therefore directly visualizes the unequal contributions of drift and diffusion to the spin precession for nonlinear SOI. We note that spins that follow $y = v_{\mathrm{dr}} t$ precess with a frequency $\omega = \frac{2m^*}{\hbar^2} v_{\mathrm{dr}} (\alpha + \beta_1 - 2\beta_3)$, recovering the result of Ref. [68], which is valid for measurements that do not spatially resolve the spin distribution (cf. Section 3.5).

We find a remarkable agreement between Eqs. (5.8) and (5.9) and the measured values for q and ω [Figs. 5.2(b-c)]. From q, we obtain $\alpha + \beta^* = 6.2 \times 10^{-13}$ eVm, which is equal to previous results from a similar sample [31]. The slope of ω vs. v_{dr} is directly proportional to β_3. We get $\beta_3 = 8.5 \times 10^{-14}$ eVm, which agrees perfectly with the measured sheet electron density of $n_{\mathrm{s}} = 5 \times 10^{15}$ m^{-2} and a bulk Dresselhaus coefficient of $\gamma = -11 \times 10^{-30}$ eVm^3 [69], by considering that $\beta_3 = -\gamma \pi n_{\mathrm{s}}/2$.

5.5 Spin drift from the isotropic limit to the PSH symmetry

In the previous section we have seen that the model of Eqs. (5.8-5.9) matches perfectly our experimental observation for drift along the PSH direction. In this section, we want to see if this is still true for drift perpendicular to the helix direction and/or when we tune the SOI from the PSH symmetry towards the isotropic limit.

We compare the measured and modeled spin dynamics with numerical Monte-Carlo simulations. We set $\beta^* = 3 \times 10^{-13}$ eVm and vary α such that we cover the full range between the isotropic case and the PSH symmetry. Using Eq. (5.3), we calculate, in small time steps of 0.1 ps, the traces of 500,000 electron spins that isotropically scatter on a Fermi circle (scattering time $\tau = 0.7$ ps, $k_{\mathrm{F}} = 1.6 \times 10^8$ m^{-1}) displaced by $k_{\mathrm{dr}} = 2.2 \times 10^7$ m^{-1}. In Fig. 5.4, we show simulation data obtained for drift along y. The spin precession is correctly described by Eqs. (5.8) and (5.9) for the entire range between the isotropic and the PSH case.

Equations (5.8) and (5.9) were derived assuming spin precession about an averaged $\langle \mathbf{B}_{\mathrm{SO}} \rangle$. This is appropriate for the PSH situation ($\alpha = \beta^*$), where

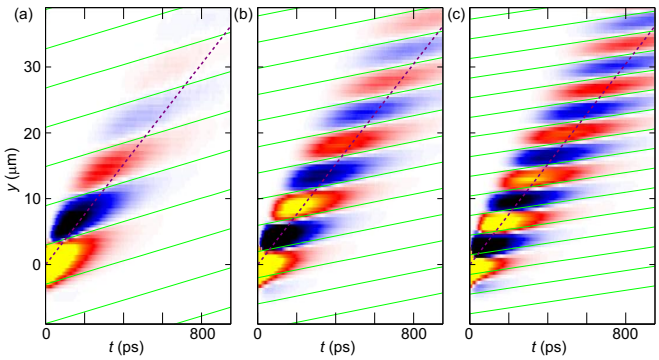

Figure 5.4: Validity of the model for drift along y. (a) to (c) Simulation data of $S_z(y,t)$ for $\alpha = 0$ eVm, $\alpha = 1.5 \times 10^{-13}$ eVm and $\alpha = 3 \times 10^{-13}$ eVm, respectively. In all cases, $\beta^* = 3 \times 10^{-13}$ eVm and $v_{\mathrm{dr}} = 38$ km/s (violet dashed line). We find good agreement between the simulation and the model (green solid lines) for the entire parameter range.

SOI is large for $\mathbf{k}||y$ and small for $\mathbf{k}||x$ [cf. Eq. (2.11)]. The spin helix is described by a strong spatial spin precession along y and no precession along x [34, 31]. The investigated sample slightly deviates from the PSH symmetry, because $\beta^* - \alpha \neq 0$ as determined from measurements in an external magnetic field [37, 31, 73]: 3×10^{-14} eVm $< (\beta^* - \alpha) < 7 \times 10^{-14}$ eVm. For drift along x, the model predicts a finite spatial spin precession with $q_x = 2m^*(\beta^* - \alpha)/\hbar^2$.

In a measurement of $S_z(x,t)$, however, for drift along x no precession is visible [Fig. 5.5(a)]. The absence of precession can be explained by the large anisotropy of the SOI. The small SOI field induced by drift along x can not destabilize the spin helix along y, which leads to the suppression of q_x. A similar effect has been predicted in a purely diffusive situation [27, 28]. It is not accounted for in our simple model, where for drift along x, the fields for $\mathbf{k}||y$ average to zero and the fields induced by drift along x appear dominant, even though electrons tracked at $y = 0$ also occupy states with $\mathbf{k}||y$.

The Monte-Carlo simulation takes the precession about all axes into account correctly and the corresponding result is shown in Fig. 5.5(b). As in the experiment, spin precession is absent. In Fig. 5.5(c), the simulation data is shown for $\alpha = 0.5$ and $\beta^* = 5.5 \times 10^{-13}$ eVm. For this almost isotropic SOI, model and simulation agree (green lines) as before in Fig. 5.4. The transition from isotropic SOI to a PSH situation, for drift along x, is summarized in Fig. 5.5(d). It shows the wavenumber q_x obtained from Monte-Carlo simulations as a function of α. The value of β^* was varied to keep $\alpha + \beta^*$ constant at 6×10^{-13} eVm. The PSH situation is realized at $\alpha = 3 \times 10^{-13}$ eVm, where the model correctly predicts $q_x = 0$. Between there and $\alpha = 2 \times 10^{-13}$ eVm, spin precession along x is completely suppressed, in contrast to the linearly increasing q_x of the simple model

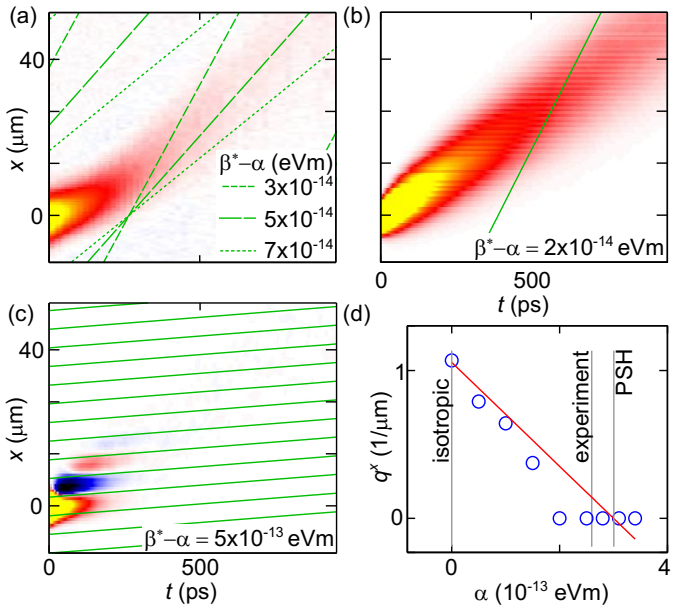

Figure 5.5: Drift along x. (a) Measured $S_z(x,t)$ for $E_x = -3$ kV/m. No precession is visible, although for our sample we expect 3×10^{-14} eVm $< \beta^* - \alpha < 7\times10^{-14}$ eVm, for which our model predicts a precession (green dashed lines mark $S_z = 0$). (b) Numerical Monte-Carlo simulation data of $S_z(x,t)$ for $\alpha = 2.9\times10^{-13}$ eVm and $\beta^* = 3.1\times10^{-13}$ eVm. As in (a), no precession pattern is observed although it is predicted by the model (green solid line). (c) Numerical Monte-Carlo simulation data of $S_z(x,t)$ for $\alpha = 0.5\times10^{-13}$ eVm and $\beta^* = 5.5\times10^{-13}$ eVm. Here, the SOI is almost isotropic and the model (green solid lines) describes the precession pattern well. (d) When α is gradually increased from zero, the q_x observed in the simulation (blue circles) initially follows $q_x = 2m^*(\beta^*-\alpha)/\hbar^2$ (red line). In a finite range around $\alpha = \beta^*$ (PSH), precession along x is suppressed ($q_x = 0$). The total strength of SOI in all simulations [(b)-(d)] is kept constant at $\alpha + \beta^* = 6\times10^{-13}$ eVm.

(red solid line). At smaller values of α, towards the isotropic case, the simulated q_x gradually approaches the model's prediction.

Note that in wire structures narrower than the SOI length, spin precession perpendicular to the wire is suppressed (see Chapter 4), and we expect drift-induced spin precession to occur along the wire in any crystallographic direction for generic SOI.

5.6 Outlook: higher-order regime

Until now, we have not observed and consequently neglected the higher-order terms in Eqs. (5.8) and (5.9). For drift along x, we found that spin precession is absent although the SOI in this sample is nonzero for k along x. In Fig. 5.6 we present a set of measurements for drift along x that clearly deviates from the data shown

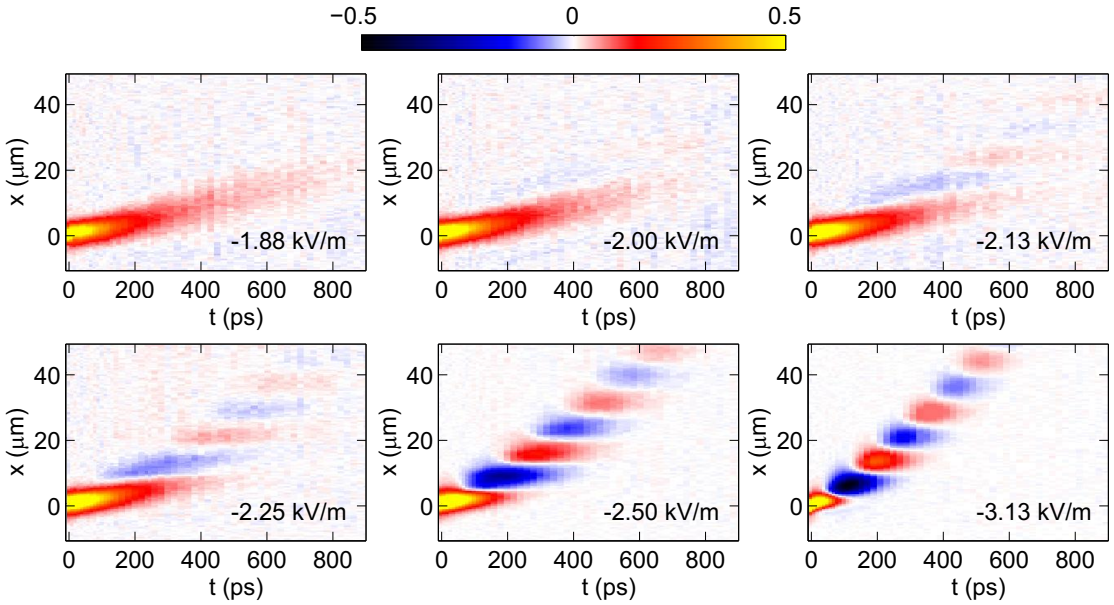

Figure 5.6: Higher-order regime for drift along x. Although the applied E fields are in the same range as for the data in Fig. 5.5, significantly higher drift velocities are reached. This is accompanied by a transition to spin dynamics that is described by a strong precession pattern.

in Fig. 5.5. In the data presented here, we observe a transition to spin dynamics that is described by a strong precession pattern. The difference in experimental conditions between the two sets of data is an elevated temperature of $T = 40$ K and reduced laser powers: 50 μW (pump) and 25 μW (probe).

For -2 kV/m ¡ E ¡ 0, spin precession is suppressed as discussed in Fig. 5.5. For more negative E fields a distinct spin precession pattern arises. This transition coincides with a sudden increase of the drift velocity (see Fig. 5.7). As in Fig. 5.2(a), we compare the fitted v_{dr} to the corresponding IV-curve. They deviate strongly from each other for negative E-fields. This indicates that there,a electrons do not follow the drifting sea of background electrons, but they are accelerated more strongly by the electric field. The drift velocity is also higher than for the data in Fig. 5.5 although the applied electric field is in the same range (see Fig. 5.7). But it is still smaller than the Fermi velocity which is $v_{\mathrm{F}} \approx 300$ km/s assuming $n_{\mathrm{s}} = 5 \times 10^{15}$ m^{-2}. For reversed E-fields, the effect did not show up and the system behaved as in Fig. 5.5. Also for drift along the y axis, such higher-order regime could not be reached.

Additional work is needed, both theoretical and experimental, to explain this finding. In a future experiment, the distance between the contacts could be reduced to, for instance, 100 μm. Then, the voltage necessary to apply an E-field of 3 kV/m is reduced to 1/8 compared to the current mesa design. This could ensure that

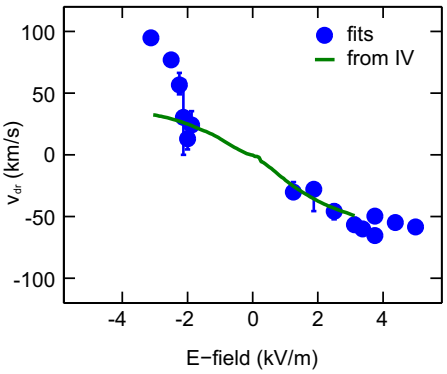

Figure 5.7: Fitted drift velocity for the data shown in Fig 5.6. The solid line is the drift velocity calculated from the measured current I via $v_{\mathrm{dr}} = I/(en_{\mathrm{s}}w)$.

one can work in the linear regime of the IV-characteristic.

All the data presented in this chapter, so far, were recorded using a quantum well in which the SOI is close to the PSH symmetry. In Fig. 5.8 we present data of drifting spins in a sample consisting of 15 nominally identical 20 nm quantum wells that are close to the isotropic limit ($\alpha \to 0$). The observed physics is very rich. At $E = 0$ kV/m the spatial precession pattern is well described by a Bessel function, as one would expect for isotropic SOI (Section 2.3.1). For $E < 0$, the spin ensemble starts to drift as in the other quantum well. But surprisingly the signature of the static Bessel function remains, albeit weakened in amplitude. It appears that two species of spins separate into one species that is affected by the electric field and starts to drift and into another species that does not drift in the electric field. For $E > 0$, even a third species appears, which does drift, but with smaller drift velocity. The origin and character of these three spin species are not identified. Excitons and trions are candidates, but additional experiments are required to test this hypothesis. Another explanation could be that the different spin species originate in quantum wells that are either not grown identically or that are not contacted identically. The separation into different spin species under drift has also been observed in a single quantum well sample, however.[2]

For the moment, we will set aside the inert species and have a look at the spins that do drift as expected. Figure 5.9 displays values for q and ω that were obtained by fitting the model of Eq. (5.1) to the data in a range of t and the spatial distance r, where the fast drifting species is sufficiently separated from the others. In both, q and ω, we see a strong change as a function of v_{dr}. The value of q shows an almost quadratic dependence with a negative prefactor, as it is anticipated by Eq. (5.8) [red line in Fig. 5.9(a)]. But we see a significant quantitative disagreement. It appears that the higher-order terms play a role already for $v_{\mathrm{dr}} < v_{\mathrm{F}}$. The Fermi

[2]Data not shown.

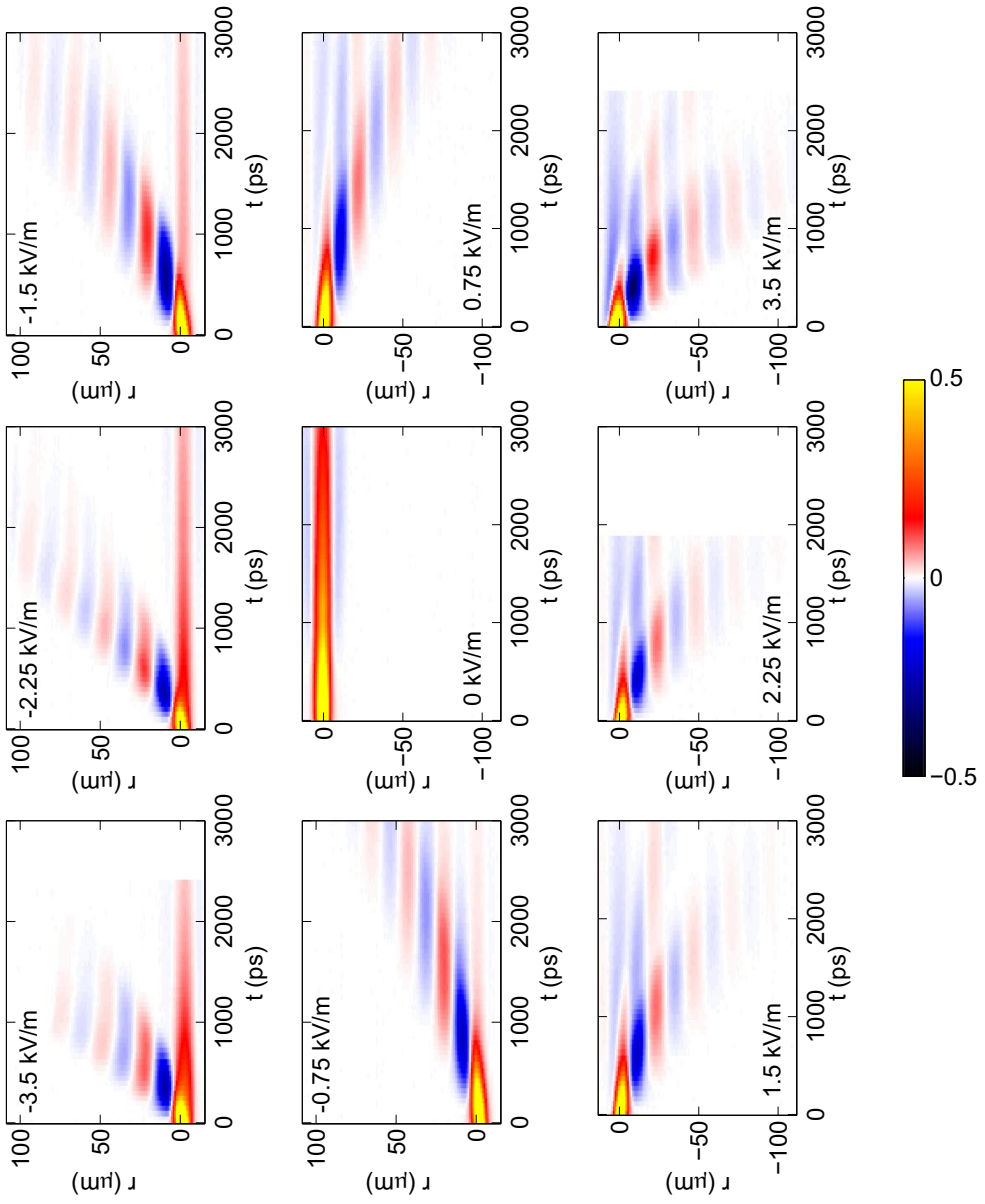

Figure 5.8: Spatially resolved spin dynamics under drift in a quantum well with almost isotropic SOI. The labeled voltage is applied to two contacts that are 200 μm apart. Besides a change in q and ω (cf. Fig. 5.9), we observe a separation into up to three spin species under drift.

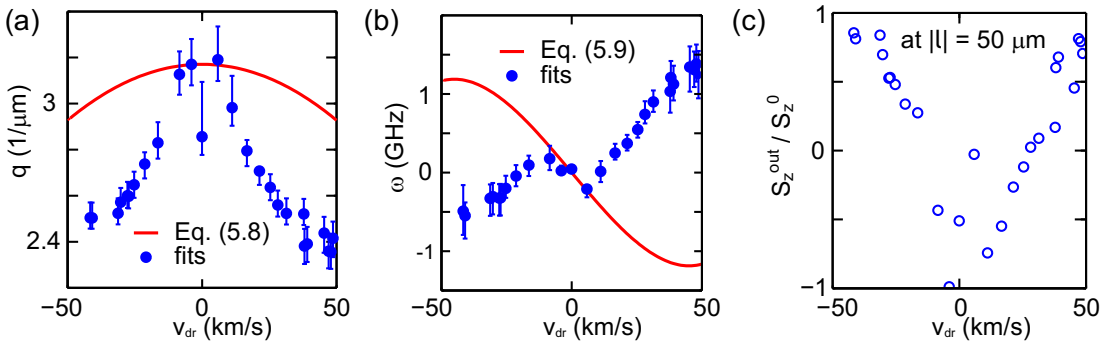

Figure 5.9: Higher-order regime of drift-induced spin precession in a symmetric 20 nm quantum well. (a) $q(v_{\mathrm{dr}})$ and (b) $\omega(v_{\mathrm{dr}})$ depend nonlinearly on v_{dr}. The red lines in (a) and (b) correspond to Eqs. (5.8) and (5.9), respectively. (c) Hypothetical orientation of S_z defined by $\cos\left[(q+\omega/v_{\mathrm{dr}})x\right]$ at a distance $x = 50$ μm from the point of injection. It appears that the orientation of the spins at $x = 50$ μm is tunable by the drift velocity over a 2π period.

velocity is estimated from the electron sheet density to be $v_{\mathrm{F}} \approx 156$ km/s. Another interesting finding is that the value at $v_{\mathrm{dr}} = 0$ is reduced compared to those at small drift velocities. Remembering that the spatial precession pattern for isotropic SOI is defined by a Bessel function (Section 2.3.1), this might indicate a transition of the precession pattern to a cosine oscillation under drift. When one fits a Bessel function with a cosine function, the obtained value of q is about 0.7 times the nominal wave vector of the Bessel function. The factor we observe in Fig. 5.9(a) is 0.87. Such a transition was not observed in the studies presented by Yang et al. [21, 92]. There, the quantum well is also symmetric (Dresselhaus only). They measure the spin dynamics by the transient spin grating technique, where standing a wave pattern of the out-of-plane spin density with a defined wave vector is excited. The standing wave pattern is very well suited to excite a PSH state [35], but it has the disadvantage that the Bessel-type precession pattern can not be directly observed and we can not judge if the precession pattern, under drift, undergoes a transition to a cosine oscillation.

Also the dependence of ω on v_{dr} is very interesting [Fig. 5.9(b)]. As for q, we observe a behavior that is qualitatively in agreement with Eq. (5.9) (red line), but the transition to the higher-order regime occurs much earlier than anticipated by the equation.

This unexpectedly strong influence of drift on the precession dynamics motivates the following consideration. In a hypothetical device in which spins are injected at a point A and then drift to a point B, is it possible to manipulate the spin orientation at point B by changing the drift velocity? Neglecting spin dephasing and spin diffusion, the following equation describes the value of S_z that

can be expected, if l is the distance between points A and B.

$$S_z^{\mathrm{out}}(l) = S_z^0 \cos[(q + \omega/v_{\mathrm{dr}})l] \tag{5.10}$$

We plot this function using the fitted values for q, ω and v_{dr} in Fig. 5.9(c) for $|l| = 50$ μm. Indeed, it seems possible to rotate the spins by a full period for the experimental data obtained from the measurements in Fig. 5.8. Motivated by this experimental result and based on the qualitative agreement between the data and Eqs. (5.8) and (5.9), we will develop novel ideas for spin amplification in the following chapter.

In conclusion, we experimentally observed and theoretically explained that, for quasi-stationary electrons, current induces a temporal spin-precession frequency that is directly proportional to the drift velocity and the strength of cubic SOI. The origin of this effect is that drift motion in a cubic SOI system leads to a precession angle twice as large as that induced by diffusive motion. Further work is needed to analytically describe the spin precession for drift along the axis of weak SOI in an anisotropic situation. The occupation of a second subband or anisotropic scattering could modify the proportionality constant between ω and β_3. The temporal precession observed should hold universally for cubic SOI, e.g., also in hole gases in group IV [96] and III-V semiconductors [22, 97, 9, 98, 99], or charge layers in oxides like perovskites [100, 101]. Moreover, the effect demonstrated must be considered when designing spintronic devices based on such systems. For readout schemes with finite-sized contacts, it may lead to a temporal smearing of the spin packet and by that to signal reduction. This can be suppressed by designing a small diffusion constant. The effect itself presents a means to manipulate quasi-stationary spins via SOI and to directly quantify the strength of the cubic Dresselhaus SOI.

In the outlook section, we presented data which suggests that, for higher drift velocities and/or for symmetries of the SOI other than the PSH symmetry, higher-order regimes are accessible which deviate from the presented model [Eqs. (5.8) and (5.9)]. Additional theoretical work is needed to explain the observed spin dynamics. In the following section, we will present an idea for spin amplification based on the observation that q and ω can depend nonlinearly on v_{dr}.

Chapter 6

Spin amplification by nonlinear spin-orbit interaction in wires

After two decades of intensive research, semiconductor spintronics still faces severe obstacles. Inspired by the iconic Datta-Das spin modulator [102], many research groups worked on the three important ingredients for such a technology: spin injection, spin manipulation and spin detection. On all three topics we have seen important breakthroughs that slowly bring this field towards realistic proof-of-principle devices [78, 103]. Implicitly these three ingredients also call for two additional requirements: long spin lifetimes and spin amplification. With persistent spin structures [29] as they are realized by balanced SOI or wire confinement (Chapters 2 and 4), the spin lifetime can be significantly enhanced although these studies must be extended to room temperature. But the lack of a convincing concept for spin amplification remains a major hurdle. For practicable logic applications it is indispensable to compensate losses, which occur during the process of one logic unit, by suitable spin amplification before passing the spin information on to the next logic unit. This is particularly important for the concept of majority-logic [104, 105], where mixing of spin states always results in a reduced spin polarization even if spin decay is completely suppressed.

In the following chapter, we will think of possible consequences of the findings presented in Chapters 4 and 5 and try to sketch device schemes that might overcome mentioned issues. We have learned that wire confinement is an excellent ingredient for device design, because it provides long spin dephasing times even for generic SOI. This brings a lot of flexibility to the conceptualization of devices. To address the point of deficient spin amplification, we will develop a novel device concept based on nonlinear spin precession under drift (cf. Section 5.6).

6.1 Quest for a spin amplifier

The earliest proposals for semiconductor-based spin amplification adapted classical electronic concepts to magnetic semiconductors, like a magnetic tunnel junction [106], a magnetic pn-junction [107] and a magnetic bipolar transistor [108]. Also a spin gain transistor was proposed that should work at the Curie temperature of a magnetic semiconductor [109]. The constraint in temperature makes the proposal difficult to realize. Further, the possibility of spin-based logic operations was pointed out [110], but a lack for spin amplification remained a major obstacle. All proposals cited in this paragraph suffer from the lack of room temperature magnetic semiconductors.

In the recent years the focus lay almost solely on metallic spintronic approaches [111]. The main idea how to implement spin amplification in metals is to switch a nanomagnet by a small spin polarized current into a direction along the polarization of that current. The nanomagnet is further used for spin injection into a subsequent nonmagnetic channel with the magnitude of spin polarization being defined by the spin injection efficiency. The orientation of the injected spin is defined by the input spin polarized current. To make the magnetization of the nanomagnet sensitive to the spin polarization of a current, it was proposed to work at bifurcation points [112] that should be reached by magnetic field pulses, which need to be synchronized by a clock signal to the spin current. The need for magnetic field pulses complicates the implementation of this idea. Ways to overcome this issue were sought and it was argued that one nanomagnet could switch another nanomagnet also without the intermediate step of setting the magnet to a bifurcation point. That might be accomplished by unequal coupling of both nanomagnets to the spin channel that connects both contacts. Asymmetric overlap and unequal tunnel interfaces were proposed [104, 113]. Based on these ideas the concept of all-spin logic has developed [104, 105, 114]. In recent years, material parameters and circuit design are being investigated and the performance tested against CMOS technology [115, 116, 117, 113].

While the field of all-spin logic has seen strong activity, concepts for spin amplification in semiconductors are very rare. It was proposed to utilize spin diffusion to induce a spin current [118]. For vanishing charge current, this leads to a large current polarization, defined as $(I_{\mathrm{up}} - I_{\mathrm{down}})/(I_{\mathrm{up}} + I_{\mathrm{down}})$. We believe that it would be more suitable to look at the local spin density, which would be significantly smaller than the current polarization. Furthermore, the local spin density would not experience amplification in the proposed scheme. Another proposal builds on a three-terminal nonlocal spin valve [119]. It is argued that under certain conditions on the magnetization orientations of the three ferromagnetic contacts, the spin current in the middle contact can be higher than the spin current in the channel. The enhanced spin current flows into the middle contact, but it can not be

extracted from there because of very small spin diffusion lengths in ferromagnetic metals. Thus, the concept may not be practicable for spin amplification.

6.2 Proposal for a spin amplifier

The main result of Chapter 5 is that for cubic SOI, spins experience a temporal precession frequency, which is linearly proportional to the drift velocity. The presented model reproduces this linear dependence, but Eq. (5.9) predicts deviations from the linear dependence scaling with $\left(\frac{k_{\mathrm{dr}}}{k_{\mathrm{F}}}\right)^2$. In Section 5.6, data were presented which proves that for high drift velocities and/or symmetries of the SOI away from the PSH symmetry, a regime of spin dynamics is accessible in which the spatial wavenumber q and the temporal frequency ω depend nonlinearly on the drift velocity v_{dr}. This confirms the prediction of the model, albeit a valid theoretical model for those cases is yet to be developed. Judging from the data seen in Fig. 5.9, this regime can be reached already for drift velocities smaller than the Fermi velocity. We will restrict the following discussion to an introduction of the conceptual idea for spin amplification based on the phenomenon of nonlinear spin precession under drift. We will refer to Eq. (5.8) and (5.9) for illustration purposes.

The proposal is based on a 1D semiconductor channel as it was discussed in Chapter 4. This ensures long spin dephasing times and a reduced diffusive dilution.

For linear SOI, the spin precession angle that is acquired by an electron traveling a certain distance l is independent of the velocity with which it traveled. This is different for cubic SOI. For the moment, we will neglect diffusion. Then it follows from Eqs. (5.8), Eq. (5.9) and $t = l/v_{\mathrm{dr}}$, that this precession angle is

$$\begin{aligned}\phi = ql + \omega t &= \frac{2m^*}{\hbar^2}\left(\alpha + \beta_1 - \beta_3\left[2 + 2\left(\frac{k_{\mathrm{dr}}}{k_{\mathrm{F}}}\right)^2\right]\right) l \\ &= \text{const.} - \frac{4m^*\beta_3}{\hbar^2}\left(\frac{v_{\mathrm{dr}}}{v_{\mathrm{F}}}\right)^2 l\,. \end{aligned} \tag{6.1}$$

The precession angle explicitly depends on the drift velocity. The constant factor depends on the strength of the linear SOI and on l. It can, thus, be adjusted to a desired constant phase factor that we set to zero for the rest of the discussion. It should be noted that ϕ does not depend on the Fermi velocity, because $\beta_3 = -\frac{\gamma m^{*2}}{4\hbar^2} v_F^2$, so that[1]

[1] Note that γ is negative.

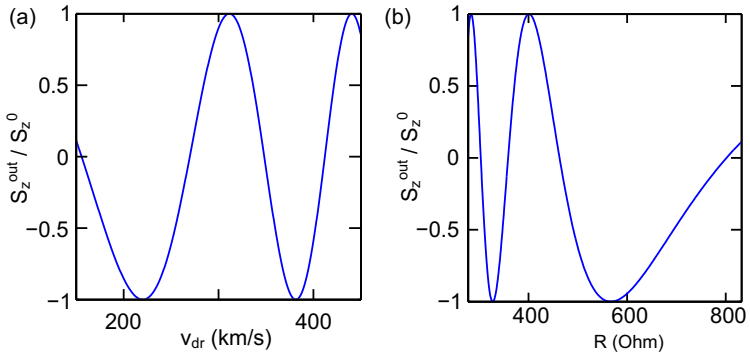

Figure 6.1: (a) Plot of $\cos(\phi)$ vs. v_{dr} with ϕ according to Eq. (6.2). Material parameters are for GaAs and $l = 20$ μm. (b) Plot of $\cos(\phi)$ vs. R with ϕ according to Eq. (6.4). Exemplarily, we chose $V = 20$ mV, $n_{\mathrm{s}} = 1 \times 10^{15}$ m^{-2} and $b = 1$ μm.

$$\phi = \gamma \frac{m^{*3}}{\hbar^4} l v_{dr}^2 \,. \tag{6.2}$$

This equation describes the precession angle of spins that are injected at point A and travel the distance l to point B with velocity v_{dr}. Assuming that spins at point A are oriented along z with the amplitude S_z^0, the spin polarization at point B is given by $S_z^{\mathrm{out}} = S_z^0 \cos(\phi)$. Figure 6.1(a) plots this relation vs. v_{dr}. We use the material parameters for GaAs ($m^* = 0.067 m_e$ and $\gamma = -11 \times 10^{-30}$ eV m^3) and set l to 20 μm, as an example. The velocities in this example are a factor 2 to 4 higher than what was observed in the previous chapter (see Fig. 5.7) and it is not clear if these high velocities can be reached easily. But we have seen in Section 5.6 that in some cases the nonlinear regime is reached already for $v_{\mathrm{dr}} < v_{\mathrm{F}}$. In the following subsection, we will present device concepts that are based on the dependence of S_z^{out} on v_{dr}.

6.2.1 Spin amplifier in linear regime

Equation (6.2) states that there is the possibility to orient spins by tuning the drift velocity. We propose to combine this behavior with a spin-selective interface, by this leading to a dependence of the spin orientation on an input spin signal. Figure 6.2 visualizes the device proposal. We imagine an input spin polarization that might stem from a preceding spintronic element. A spin-selective interface (yellow) between the semiconductor channel and a ferromagnet encodes the z component of the input spin polarization S_z^{in} in a resistance [120]. We model the total device resistance between the ground and the applied voltage V at point B by

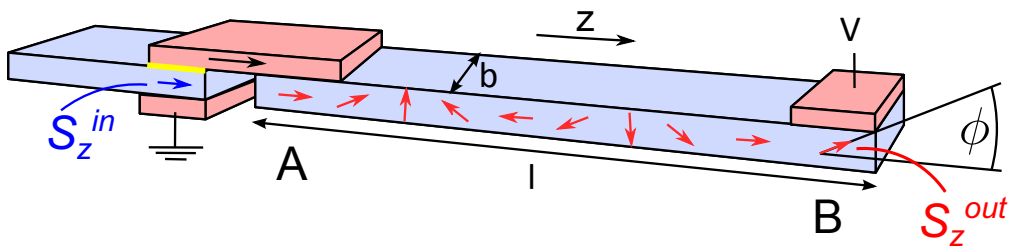

Figure 6.2: Possible realization scheme for the proposed devices. The input of the device, denoted as S_z^{in}, is the output of a previous spintronic device and is translated by a spin-selective interface (yellow) into a device resistance, R, which is given by Eq. (6.3). A ferromagnet injects spins with maximum amplitude (limited by the injection efficiency) at point A. Those spins then drift with $v_{\text{dr}} = V/(en_{\text{s}}bR)$ to point B. The output of the device, S_z^{out}, is a function of S_z^{in}.

$$R(S_z^{\text{in}}) = R_1(1 - \eta S_z^{\text{in}}) + R_2 = R_0(1 - \zeta S_z^{\text{in}})\,, \tag{6.3}$$

where η is the selectivity of the interface, R_1 is the interface resistance for unpolarized input and R_2 is the total non spin-dependent resistance between the grounded contact and the contact at point B. η has a value between -1 and 1. This equation is simplified by the introduction of $R_0 = R_1 + R_2$ and $\zeta = \eta \frac{R_1}{R_1+R_2}$. The ferromagnetic contact injects spins at point A with a maximum amplitude of S_z^0 and $\phi = 0$ into a semiconductor channel in which Eq. (6.2) is valid. This channel might also be a 2D electron gas [121]. The drift velocity between points A and B is $v_{\text{dr}} = V/(en_{\text{s}}bR)$, where e is the electron charge, n_{s} is the sheet electron density in the 2D electron system in the channel, b is the width of the channel and R is given by Eq. (6.3). This leads to a dependence of the orientation of the spins at point B on the device resistance and by that on S_z^{in}.

$$\phi = \gamma \frac{m^{*3}}{\hbar^4} l \left[\frac{V}{en_{\text{s}}bR(S_z^{\text{in}})}\right]^2 \tag{6.4}$$

We show $S_z^{\text{out}} = S_z^0 \cos(\phi)$ vs. R in Fig. 6.1(b) for the same range of drift velocities as in Fig. 6.1(a).

For a suitable choice of material parameters, the device can be tuned to a working point close to a zero transition of the characteristics plotted in Fig. 6.1. Close to this point, the device functions as a spin amplifier due to an approximately linear input-output characteristic, for example, as plotted in Fig. 6.3.

Steeper slopes and by this higher amplification factors can be realized by tuning the parameters. Materials with stronger SOI, i.e. larger values for γ, yield larger amplification factors. A large value of γ is, for instance, expected for InSb [9]. In the example of Fig. 6.3, an input spin signal that has dropped to 5 % of S_z^0 is amplified to about 50 % S_z^0.

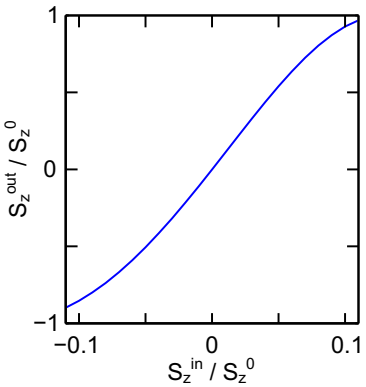

Figure 6.3: Input-Output characteristics of a spin amplifier for a selectivity of the interface of $\zeta = 0.5$. The other parameters are $R_0 = 303$ Ohm, $l = 20$ μm, $V = 20$ mV, $b = 1$ μm and $n_s = 1 \times 10^{15}$ m^{-2}. In this example, a spin input signal, which has dropped to 5 % of S^0, is amplified by about an order of magnitude.

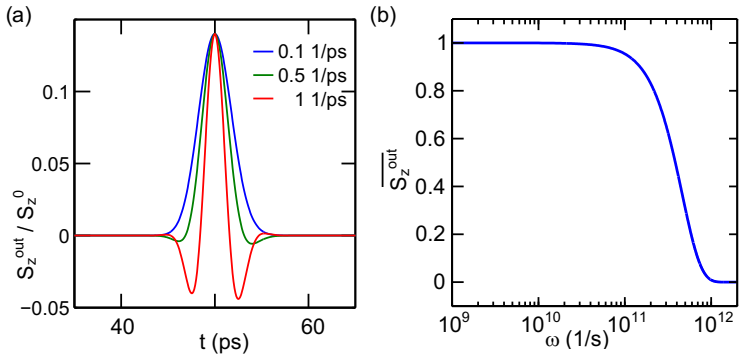

Figure 6.4: (a) Temporally resolved signal at point B taking into account diffusion. Diffusion leads to a spread of the effective velocities with which electrons reach contact B. Assuming spins are injected at A at $t = 0$, we get the plotted spin signal following Eq. (6.5) and assuming $D_s = 5 \times 10^{-3}$ m^2/s and a spatial width of the injection contact of $\sigma_0 = 100$ nm. We show the relation for three different values of ω as given in the legend. (b) Amplitude reduction according to Eq. (6.6). When time-averaging over a signal as in (a), the amplitude gets reduced for high ω.

In this example, we have neglected spin decay in the semiconductor channel itself. In Chapter 4, we have experimentally demonstrated a spin lifetime in wire structures of approximately 10 ns. This value may well be exceeded for reduced electron sheet densities, because the decay rate is proportional to n_s^2 [cf. Eq. (4.3)]. For the range of parameters in Fig. 6.3, the time it takes an electron to travel from point A to point B is about 100 ps. Taking $\tau_0 = 10$ ns, the decay of the amplitude is less than 1 %. The diffusive spread of the electrons is more critical. The discussion until now is only valid for $D_\mathrm{s} \to 0$. Diffusion leads to a spread of the effective velocities with which the electrons reach point B. We adapt Eqs. (4.4) and (5.1) to obtain

$$S_z^\mathrm{out}(q,\omega,l,t) = S_z^0 \frac{\sigma_0}{\sigma(t)} \exp\left[\frac{-(l-v_\mathrm{dr}t)^2}{2\sigma^2(t)}\right] \cos(\omega t + ql)\,, \tag{6.5}$$

neglecting the exponential decay to see the influence of diffusion only. The combined width of the injection and detection contact is denoted by σ_0 and $\sigma^2(t) = \sigma_0^2 + 2D_\mathrm{s}t$. We further neglected the decay term which accounts for the signal reduction due to large injection and detection areas [cf. Eq. (4.6)]. This is justified because it should be possible to design injection and detection contacts with widths that are much smaller than the spin precession length, i.e. $\sigma_0 \ll 2\pi/q$. Figure 6.4(a) shows the temporal evolution of S_z^out/S_z^0 assuming that spins are injected at point A at $t = 0$. Because the proposed device has no time resolution, at point B, the time average of the this curve is measured. To emulate this, we need to integrate Eq. (6.5) over t. The averaging over the oscillations of S_z^out in time leads to a signal reduction similar to the one for large laser spots (cf. Section 3.3). To calculate the time integration of Eq. (6.5), we have to assume that $\sigma^2(t) = \sigma_0^2 + 2D_\mathrm{s}{}^l/_{v_\mathrm{dr}}$ and we get

$$\begin{aligned}\overline{S_z^\mathrm{out}}(q,\omega,l) &= \int_{-\infty}^{+\infty} S_z^\mathrm{out}(q,\omega,l,t)\,\mathrm{d}t \Big/ \int_{-\infty}^{+\infty} S_z^\mathrm{out}(q,\omega=0,l,t)\,\mathrm{d}t \\ &= \exp\left[-\frac{\omega^2}{2v_\mathrm{dr}^2}\left(\sigma_0^2 + 2D_\mathrm{s}\frac{l}{v_\mathrm{dr}}\right)\right] \cos\left(\frac{\omega l}{v_\mathrm{dr}} + ql\right)\,. \end{aligned} \tag{6.6}$$

The prefactor $\sigma(t)^{-1}$, which describes diffusive dilution, does not play a role in a measurement without time resolution. The value of q is adjustable to make the cosine equal to one. Under this assumption, we plot Eq. (6.6) in Fig. 6.4(b). We see that, unless the frequency gets too high, the loss of spin polarization at point B is negligible. The performance of the proposed spin amplifier will in consequence depend on how exactly q and ω scale with v_dr. It is preferable to have a strong dependence for q and a weak dependence for ω.

Figure 6.5 explains how the device proposal might be combined with spintronic

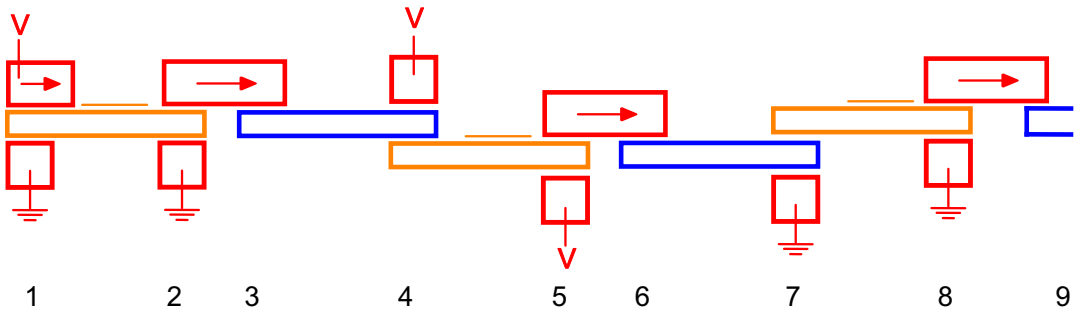

Figure 6.5: Possible realization scheme for a cascade of spintronic elements. Red color stands for metallic contacts. An arrow indicates the magnetization direction of a magnetic contact. Orange denotes a spintronic element, possibly a logic unit. Blue denotes the spin amplifier. The arrangement is such that the voltage V always drops over the spin amplifier where a drift current of spins is demanded. There is no voltage drop over the spintronic device that may, hence, work with diffusive spin currents. Point 9 is identical to point 3.

units to a cascade of elements. At point 1, spins are injected into a spintronic unit (orange), possibly a logic unit. The sketch of Fig. 6.2 starts at point 2 and goes to point 4. The spin signal that might have degraded between point 1 and point 2 is, thus, enhanced by the spin amplifier and an amplified spin signal is available at point 4, where it is used as an input for a following spintronic unit. The output of this unit is again fed into a spin amplifier between points 5 and 7. The voltage V alternates with a ground such that there is always a potential gradient over the spin amplifying channel (blue) and no potential difference over the spintronic device, which may thus work with diffusive spin currents. After point 9, the sequence can be continued like after point 3. Thus, a cascade of elements is realized.

6.2.2 Majority vote in oscillatory regime

We consider a majority logic [104, 113] where the output spin polarization is a logic operation of the spin polarization of a number of individual input electrodes. Each input might either be $+S_z^{\text{in}}$ or $-S_z^{\text{in}}$. We refer to these states as ($\uparrow$) and ($\downarrow$), respectively. For three input channels, the possible input states are ($\downarrow\downarrow\downarrow$), ($\downarrow\downarrow\uparrow$), ($\downarrow\uparrow\uparrow$) and ($\uparrow\uparrow\uparrow$). Mixing of these three input channels results in the amplitudes $-S_z^{\text{in}}$, $-S_z^{\text{in}}/3$, $+S_z^{\text{in}}/3$ and $+S_z^{\text{in}}$, respectively.

Often in majority logic gates, only three out of the four input states occur. The following table illustrates a NAND gate, where one of the three inputs is constantly set to $\downarrow$ (control bit). Only the input states ($\downarrow\downarrow\downarrow$), ($\downarrow\downarrow\uparrow$) and ($\downarrow\uparrow\uparrow$) occur.

Concepts for the realization of such majority logic gates exist that rely on the switching of the magnetization axis of a ferromagnetic contact by spin transfer

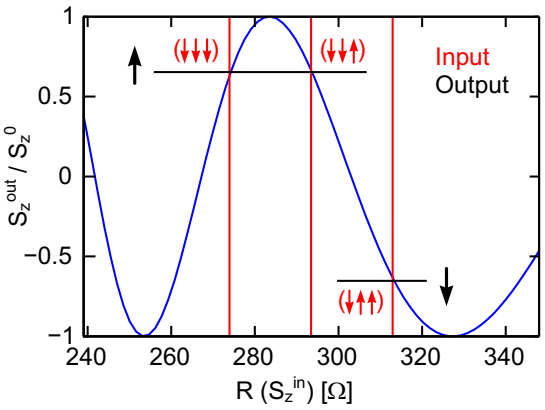

Figure 6.6: An implementation of a majority logic NAND gate in the nonlinear regime of the spin amplifier. We use $R_0 = 303$ Ohm, $\zeta = 0.1$ and the other parameters are as in Fig. 6.3. The red lines mark from right to left the input states (↓↓↓), (↓↓↑) and (↓↑↑), respectively.

Control bit	Bit 1	Bit 2	Input	Output
↓	↑	↑	(↓↑↑)	↓
↓	↑	↓	(↓↓↑)	↑
↓	↓	↑	(↓↓↑)	↑
↓	↓	↓	(↓↓↓)	↑

Table 6.1: Table for a majority logic NAND gate.

torque [104, 113]. The spin amplifier proposed here provides an alternative to such a method and does not require the switching of a magnetization axis. It builds on the oscillatory behavior observed in Fig. 6.1(b). The goal is to realize the connection between the output (fifth column) and the input states (forth column) as defined in Table 6.1.

Figure 6.6 plots how we envision the realization of a NAND gate in the oscillatory regime of the spin amplifier. The device is tuned such, that it delivers the output state ↑ for the input states (↓↓↓) and (↓↓↑), and the output state ↓ for the input state (↓↑↑). The maximum amplitude of the output in this example is $0.65\, S_z^0$.

The intention here is to present a general concept and we hope that further engineering, experimental and theoretical efforts will eventually lead to a realization of that idea.

A

Appendix

A.1 Recipes for sample processing

A.1.1 Photo lithography and wet chemical etching

After every bath in acetone, the sample is directly put into a bath of isopropanol and afterwards dry blown with a nitrogen pistol.

Cleaning after cleaving:

1. Clean sample from GaAs dust in ultra-sonic bath in acetone.
2. Removal of liquid gallium on the backside. Slide over a warm dummy wafer until the backside is sufficiently even. If required the following recipe will clean the backside from gallium more thoroughly. Coat the front side by resist AZ6612 for protection. Etch the gallium in H_2O : HCl = 1:1 for 1 to 2 minutes until the gallium is removed. Stop in DI water. Clean the sample in acetone and isopropanol.
3. Oxygen plasma: Put sample on a watch glass to reduce the contact to the massive metal slide of the oxygen oven. This makes the conditions more reproducible, because the temperature of the slide is either room temperature or up to several ten °C depending on which and when another process was running in the machine. I recommend 400 W for which an resist etch rate of 38 nm/min was determined. For this step, 20 s are recommended. It is advisable to repeat this step before lithography or etching.

Photo lithography (positive resist):

1. Spin on AZ1505 resist with 4000 rpm.
2. Bake at 110 °C for 1 min.
3. Use mask aligner in soft-contact mode. Exposure time has to be adapted to the intensity of the UV lamp.

4. Developer AZ400K 1:4 for 40 s. Observe how the structure is developing.
5. Stop in DI water and blow dry.

Photo lithography (negative resist):

1. Spin on N415 resist with 4000 rpm.
2. Bake at 85 °C for 3 min.
3. Use mask aligner in soft-contact mode. Exposure time has to be adapted to the intensity of the UV lamp.
4. Developer ma-D332s for 80 s. Observe if the structure is developing.
5. Stop in DI water and blow dry.

Wet-chemical etching:

1. Prepare the etching solution: $H_2O : H_2SO_4 : H_2O_2 = 100 : 3 : 1$, for instance, 200 ml : 6 ml : 2 ml. Always water first.
2. Etch the sample while holding it with tweezers and moving it around: etch rate = 70-80 nm/min.
3. Stop in DI water.

Lift-off:

1. Put sample in acetone and let the resist be dissolved. Elevated temperatures help, but attention: not too high otherwise the acetone will start smoking. Recommended temperature: 30 °C.
2. Hold the sample with the tweezers and use a plastic pipette to flush it with acetone until all metal came off where it should.
3. For fine structures it can help to look at the sample in an optical microscope before taking it out of the acetone. After taking the sample out of the acetone, it is not recommended to continue the lift-off process.
4. Clean in another acetone bath.

Annealing:

1. Annealing in inert gas at 425 °C for 30 s.

A.1.2 E-beam lithography and inductively-coupled plasma etching

Sample preparation: ultrasonic bath, oxygen plasma (400 W, 2 min), dehydration bake (180 °C, 2 min).

PMMA coating

- PMMA 950k / AR-P 672.05 (360 nm @ 4000 rpm)
- Use 6000 rpm for 60 s to get 250 nm resist height. The higher the rotation frequency of the spinner, the more homogeneous the resist, particularly on small samples.
- Bake at 180 °C for 2 mins.

E-beam settings (Raith)

- 10 μm aperture, 10 kV acceleration voltage and 200 μm write field size
- Area: step: 0.01 μm, dwell time: 0.001016 ms, Dose: 30 μC/cm^2, speed: 9.84 mm/s
- Curves: step: 0.015 μm, dwell time: 0.099 ms, dose: 1300 μC/cm^2, speed: 0.15 mm/s
- Lines: step: 0.01 μm, dwell time: 0.0061 ms, dose: 1800 pC/cm, speed: 1.64 mm/s

These setting were used when a current of 0.02952 nA was measured at the Faraday cup. It is recommended to write several single-pixel lines as a separation between two wires. The developed PMMA resist can directly be used as a mask for ICP etching.

PMMA development

- Isopropanol : $H_2O = 21 : 9$
- Put into ultrasonic bath at low power setting (9 o'clock)
- Develop for 40 s and check under optical microscope. Stop by blow drying. If it is not sufficiently developed it is possible to continue developing.
- Directly before the ICP: remove remaining resist by 16-20 s in the oxygen plasma at 400 W. Always use a watch glass.

ICP-RIE settings

- Helium backing: 10
- Gas Out HBr: 40
- RF Power: 80 W
- ICP RF Power: 800 W
- No passivation gas
- Chuck temperature: 80 °C
- Etching time: 40 s for 500-600 nm

Put the sample on a Quartz wafer in the ICP. TEM wax can be used for gluing the sample on the wafer. This ensures better thermal contact. But the risk that the wax destroys the chemistry is very high and it is recommended to just lye the sample on top of the wafer. Always run a test run for 5 to 10 mins with the dummy wafer but without the sample to see if ICP is stable.

A.2 List of measured samples

Sample name	D110831 stripes S2
Description	PSH wires
Quantum well width	12 nm
Processing steps	Photo-lithography of wire structures; wet-chemical etching
Presented in	Section 4.4
Sheet electron density (@40K)	$4 - 5 \times 10^{15}$ m^{-2}
Mobility (@40K)	22 m^2 (Vs)$^{-1}$

Sample name	F140206A_6
Description	Dresselhaus wires
Quantum well width	12 nm
Processing steps	Photo-lithography of wire structures; wet-chemical etching
Presented in	Section 4.3
Sheet electron density (@4K)	3.5×10^{15} m^{-2}
Mobility (@4K)	70 m^2 (Vs)$^{-1}$

Sample name	D110831A_A2b
Description	PSH drift
Quantum well width	12 nm
Processing steps	Photo-lithography of mesa structure; wet-chemical etching. Photo-lithography of contact pads; Evaporation of AuGeNi; Lift-off; Annealing.
Presented in	Section 5.3
Sheet electron density (@40K)	$4 - 5 \times 10^{15}$ m^{-2}
Mobility (@40K)	22 m^2 (Vs)$^{-1}$

Sample name	D090908B_5
Description	Multi-quantum well, isotropic drift
Quantum well width	20 nm
Processing steps	Photo-lithography of mesa structure; wet-chemical etching. Photo-lithography of contact pads; Evaporation of AuGeNi; Lift-off; Annealing.
Presented in	Section 5.6
Sheet electron density (@20K)	1.3×10^{15} m^{-2}
Mobility (@20K)	46 m^2 (Vs)$^{-1}$

A.3 Solid immersion lens

The spatial resolution of the setup (described in Section 3.2) can be enhanced by using a solid immersion lens (SIL). Figure A.1(a) shows an optical micrograph of a zirconia half-sphere on a gold checkerboard. The SIL has a diameter of 3 mm and the checkerboard has an edge length of 20 μm. The pattern is magnified through the SIL by a factor n, which corresponds to the refractive index of zirconia ($n = 2.13$). When focusing the pump and probe spots through a SIL, one can achieve sigma-widths of the intensity profiles which are $1/n$-times smaller compared with the situation without a SIL [see Fig. A.1(b)]. The width is determined from overlap scans of the Kerr signal at $t = 0$ assuming that pump and probe have the same spot size σ and that the overlap is given by $\sqrt{2}\sigma$. The data shown in Fig. A.1(c) are taken on the same sample as the data shown in Fig. 4.2 for a 0.7 μm-wide wire

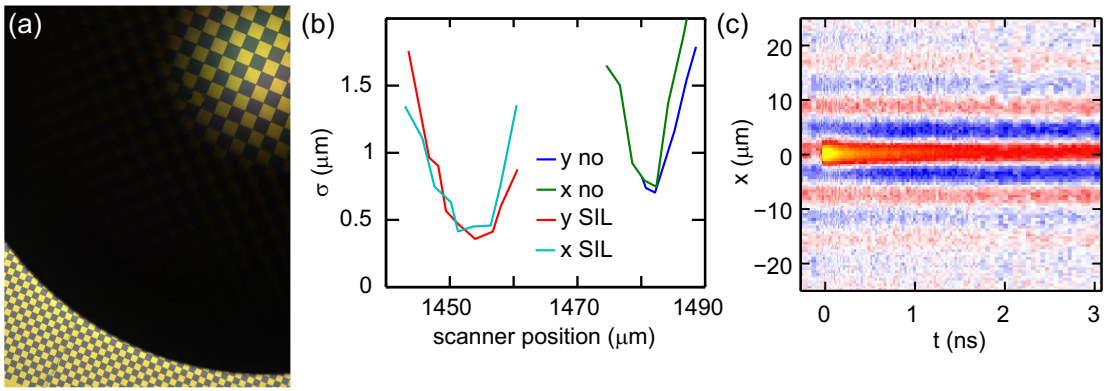

Figure A.1: (a) Optical micrograph of a SIL on a checkerboard where each edge length is 20 μm. (b) Sigma widths of the pump and probe spots against the scanner position, which is related to the distance between the sample surface and the focusing lens. σ is determined by fitting an overlap scan of the Kerr signal at $t = 0$ considering that this scan's width is given by $\sqrt{2}\sigma$. (c) Map of $S_z(x,t)$ measured through a SIL. The data are taken from a 0.7 μm-wide wire along the x direction of the same sample as in Fig. 4.2.

along the x direction. Because of diffraction on the surface of the half-sphere, only an area of about 1 mm width is accessible as can be judged also from the dark area in Fig. A.1(a).

A.4 Fitting – determination of the confidence intervals

The discussion in this section follows the description in the book on data analysis by D. S. Sivia [122].

When we measure the spatio-temporal evolution of a local spin excitation as we will explain in Section 3.2, we obtain data of the local spin polarization along a spatial axis at different time steps. This 2D data set is then evaluated by fitting to it a model function that must be suitable to the experimental setting. The physical quantities of interest are parameters of this function. In the following, we will explain how we obtain these parameters and how we define confidence intervals to give an estimate of their reliability. But first, we want to develop an understanding for the impact of noise.

Assume a measurement, where we directly measure a physical quantity, say the current flowing through a 2D electron gas, and we read the value every 100 ms. Due to noise, the value will fluctuate around its actual value, x_0, and the distribution of measured values follows an approximately Gaussian distribution. The probability P to measure the value x is then given by

$$P(x) = \frac{1}{\sigma\sqrt{2\pi}} \exp\left[-\frac{(x-x_0)^2}{2\sigma^2}\right] . \tag{A.1}$$

We are interested to know the values of x_0 and σ, which is a measure of how well x_0 is defined. To find x_0, we can determine the value with the maximum probability by

$$\left.\frac{\partial P}{\partial x}\right|_{x_0} = 0 \tag{A.2}$$

$$\left.\frac{\partial^2 P}{\partial x^2}\right|_{x_0} < 0 . \tag{A.3}$$

In fact, we can also determine σ from this. We define L as the logarithm of P and make a Taylor expansion of it around x_0.

$$L = \ln(P) = L(x_0) + \frac{1}{2}\left.\frac{\partial^2 L}{\partial x^2}\right|_{x_0} (x-x_0)^2 + \dots \tag{A.4}$$

The first derivative is zero at an extremum. Going back to P, we obtain

$$P \approx A \exp\left(\frac{1}{2}\left.\frac{\partial^2 L}{\partial x^2}\right|_{x_0}(x-x_0)^2\right), \tag{A.5}$$

with A an amplitude. Comparing with Eq. (A.1), we see that

$$\sigma = \left(-\left.\frac{\partial^2 L}{\partial x^2}\right|_{x_0}\right)^{-1}. \tag{A.6}$$

The meaning of σ can be interpreted as follows. The probability that x lies withing the interval $x = x_0 \pm \sigma$ is given by $\int_{x_0-\sigma}^{x_0+\sigma} P(x)\mathrm{d}x = 67\%$. The probability that x lies withing $x_0 \pm 2\sigma$ is already 95 %. It can further be shown that

$$\sigma^2 = \sqrt{\langle (x-x_0)^2 \rangle} =: \mathrm{RMS}\,. \tag{A.7}$$

The latter is known as the root-mean-squared error.

From this simple example, we now move on to a more complex situation as we encounter it in our experiments. Instead of a single quantity that we measure several times, we collect a 2D array of data points $\mathbf{D}$ with n steps in time and m steps in a spatial direction (cf. Section 3.2). This gives $N = n \cdot m$ data points. $\mathbf{D}$ shall now be fitted by a model function f($\mathbf{X}$), where $\mathbf{X}$ is a set of parameters. We define the squared error by

$$\mathrm{SE} = \sum_{n,m} (f(\mathbf{X}, n, m) - \mathbf{D}_{n,m})^2\,. \tag{A.8}$$

Then it can be shown that the covariance between two parameters is

$$\langle (X_i - X_{0,i})(X_j - X_{0,j}) \rangle = \frac{2}{N}\left[\left(\nabla\nabla \mathrm{SE}|_{\mathbf{X}_0}\right)^{-1}\right]_{i,j} \mathrm{SE}\,. \tag{A.9}$$

The indices i and j each denote one of the parameters in $\mathbf{X}$. This, together with Eq. (A.7), gives

$$\sigma_{i,i}^2 = \left\langle (X_i - X_{i,0})^2 \right\rangle = \frac{2}{N}\left(\left.\frac{\partial^2 \mathrm{SE}}{\partial X_i^2}\right|_{\mathbf{X}_0}\right)^{-1} \mathrm{SE}(\mathbf{X}_0)\,. \tag{A.10}$$

This means that, if we want to determine the confidence interval for a fit parameter X_i, we need to determine $\mathrm{SE}(X_i)$. We do this by varying X_i through a suitable range in small steps. At each step, we optimize all other parameters of $f(\mathbf{X})$ to minimize SE. In most cases, this function can be well approximated by a parabola with a curvature c. Under this assumption, the second derivative is $2c$ and above formula simplifies to

$$\sigma_{i,i}^2 = \frac{\mathrm{SE}}{cN}\,. \tag{A.11}$$

The parabolic approximation of SE(X_i) is not always a good approximation. In reality, we often encounter asymmetric increases of SE(X_i) to either side. This is often the case for the spin dephasing time τ, for which it is regularly found that the fit error increases steeply towards smaller values of τ and slowly towards larger values. In the worst case, we encounter a complicated landscape of SE($\mathbf{X}$) with several minima. Another minimum in the vicinity of the global minimum is not accounted for if only the global minimum is approximated by a parabola.

In the publications, which resulted from the work presented in Chapters 4 and 5, we chose a definition of the confidence intervals that can deal with both, asymmetric increases of the fit error and several nearby minima. The indicated confidence interval of each parameter is defined as a maximum 5% increase of SE(X_i) from its minimum. During the course of writing this thesis we realized, however, that, considering the upper formalism, a more suitable definition would be an increase of SE or MSE by $1/N$. On the one hand, for typical values of $N = 2000$ to 10000, the definition applied in the publications leads to an overestimation of the confidence intervals of $\sqrt{0.05N}$ ranging from 10 to 22. On the other hand, any systematic errors must be considered in addition to the statistical errors discussed above. Thus, the overestimation is less severe.

Bibliography

[1] G. Dresselhaus. *Spin-Orbit Coupling Effects in Zinc Blende Structures*. Phys. Rev., **100**, 580 (1955). URL http://dx.doi.org/10.1103/PhysRev.100.580.

[2] F. T. Vasko. JETP Lett., **30**, 541 (1979).

[3] Y. U. Bychkov, E. I. Rashba. *Oscillatory effects and the magnetic susceptibility of carriers in inversion layers*. J. Phys. C, **17**, 6039 (1984).

[4] J. H. Davies. *The physics of low-dimensional semiconductors*. Cambridge University Press (2006).

[5] S. A. Crooker, D. L. Smith. *Imaging spin flows in semiconductors subject to electric, magnetic, and strain fields*. Phys. Rev. Lett., **94**, 236601 (2005). URL http://dx.doi.org/10.1103/PhysRevLett.94.236601.

[6] T. Ihn. *Semiconductor nanostructures*. Oxford University Press (2010).

[7] A. Einstein. *Zur Elektrodynamik bewegter Körper*. Annalen der Physik, **322**, 891 (1905). ISSN 1521-3889. URL http://dx.doi.org/10.1002/andp.19053221004.

[8] H. Lorentz. *Electromagnetic phenomena in a system moving with any velocity smaller than that of light*. Proceedings of the Royal Netherlands Academy of Arts and Sciences, **6**, 809 (1904). URL https://archive.org/details/proceedingsofsec06akad.

[9] R. Winkler. *Spin-Orbit Coupling Effects in Two-Dimensional Electron and Hole Systems*. Springer (2003).

[10] R. Winkler, U. Rössler. *General approach to the envelope-function approximation based on a quadrature method*. Phys. Rev. B, **48**, 8918 (1993). URL http://dx.doi.org/10.1103/PhysRevB.48.8918.

[11] M. Studer, G. Salis, K. Ensslin, D. C. Driscoll, A. C. Gossard. *Gate-Controlled Spin-Orbit Interaction in a Parabolic* GaAs/AlGaAs *Quantum*

Well. Phys. Rev. Lett., **103**, 027201 (2009). URL http://dx.doi.org/10.1103/PhysRevLett.103.027201.

[12] M. Q. Weng, M. W. Wu, H. L. Cui. *Spin relaxation in n-type GaAs quantum wells with transient spin grating*. J. Appl. Phys., **103**, 063714 (2008). URL http://scitation.aip.org/content/aip/journal/jap/103/6/10.1063/1.2899962.

[13] M. C. Lüffe, J. Kailasvuori, T. S. Nunner. *Relaxation mechanisms of the persistent spin helix*. Phys. Rev. B, **84**, 075326 (2011). URL http://dx.doi.org/10.1103/PhysRevB.84.075326.

[14] J. Kainz, U. Rössler, R. Winkler. *Anisotropic spin-splitting and spin-relaxation in asymmetric zinc blende semiconductor quantum structures*. Phys. Rev. B, **68**, 075322 (2003). URL http://dx.doi.org/10.1103/PhysRevB.68.075322.

[15] W. Knap, C. Skierbiszewski, A. Zduniak, E. Litwin-Staszewska, D. Bertho, F. Kobbi, J. L. Robert, G. E. Pikus, F. G. Pikus, S. V. Iordanskii, V. Mosser, K. Zekentes, Y. B. Lyanda-Geller. *Weak antilocalization and spin precession in quantum wells*. Phys. Rev. B, **53**, 3912 (1996). URL http://dx.doi.org/10.1103/PhysRevB.53.3912.

[16] M. Hruška, v. Kos, S. A. Crooker, A. Saxena, D. L. Smith. *Effects of strain, electric, and magnetic fields on lateral electron-spin transport in semiconductor epilayers*. Phys. Rev. B, **73**, 075306 (2006). URL http://dx.doi.org/10.1103/PhysRevB.73.075306.

[17] M. M. Glazov, E. L. Ivchenko. *Precession spin relaxation mechanism caused by frequent electron-electron collisions*. JETP Lett., **75**, 403 (2002). URL http://dx.doi.org/10.1134/1.1490009.

[18] M. A. Brand, A. Malinowski, O. Z. Karimov, P. A. Marsden, R. T. Harley, A. J. Shields, D. Sanvitto, D. A. Ritchie, M. Y. Simmons. *Precession and motional slowing of spin evolution in a high mobility two-dimensional electron gas*. Phys. Rev. Lett., **89**, 236601 (2002). URL http://dx.doi.org/10.1103/PhysRevLett.89.236601.

[19] I. D'Amico, G. Vignale. *Theory of spin Coulomb drag in spin-polarized transport*. Phys. Rev. B, **62**, 4853 (2000). URL http://dx.doi.org/10.1103/PhysRevB.62.4853.

[20] C. P. Weber, N. Gedik, J. E. Moore, J. Orenstein, J. Stephens, D. D. Awschalom. *Observation of the spin Coulomb drag in a two-dimensional*

electron gas. Nature, **437**, 1330 (2005). URL http://www.nature.com/nature/journal/v437/n7063/full/nature04206.html.

[21] L. Yang, J. D. Koralek, J. Orenstein, D. R. Tibbetts, J. L. Reno, M. P. Lilly. *Doppler velocimetry of spin propagation in a two-dimensional electron gas*. Nat. Phys., **8**, 153 (2012). URL http://www.nature.com/nphys/journal/v8/n2/full/nphys2157.html.

[22] M. I. Dyakonov, V. I. Perel'. Sov. Phys. Solid State, **13**, 3023 (1972).

[23] X. Liu, J. Sinova. *Unified theory of spin dynamics in a two-dimensional electron gas with arbitrary spin-orbit coupling strength at finite temperature*. Phys. Rev. B, **86**, 174301 (2012). URL http://dx.doi.org/10.1103/PhysRevB.86.174301.

[24] M. C. Lüffe, J. Danon, T. S. Nunner. *Evolution of the persistent spin helix in the presence of Hartree-Fock fields*. Phys. Rev. B, **87**, 125416 (2013). URL http://dx.doi.org/10.1103/PhysRevB.87.125416.

[25] J. M. Kikkawa, D. D. Awschalom. *Lateral drag of spin coherence in gallium arsenide*. Nature, **397**, 139 (1999). URL http://www.nature.com/nature/journal/v397/n6715/abs/397139a0.html.

[26] V. A. Froltsov. *Diffusion of inhomogeneous spin distribution in a magnetic field parallel to interfaces of a III-V semiconductor quantum well*. Phys. Rev. B, **64**, 045311 (2001). URL http://dx.doi.org/10.1103/PhysRevB.64.045311.

[27] T. D. Stanescu, V. Galitski. *Spin relaxation in a generic two-dimensional spin-orbit coupled system*. Phys. Rev. B, **75**, 125307 (2007). URL http://dx.doi.org/10.1103/PhysRevB.75.125307.

[28] A. V. Poshakinskiy, S. A. Tarasenko. *Spatiotemporal spin fluctuations caused by spin-orbit-coupled Brownian motion*. Phys. Rev. B, **92**, 045308 (2015). URL http://dx.doi.org/10.1103/PhysRevB.92.045308.

[29] J. Schliemann. *Persistent Spin Textures in Semiconductor Nanostructures*. arXiv:1604.02026 (2016). URL http://arxiv.org/abs/1604.02026.

[30] A. A. Burkov, A. S. Núñez, A. H. MacDonald. *Theory of spin-charge-coupled transport in a two-dimensional electron gas with Rashba spin-orbit interactions*. Phys. Rev. B, **70**, 155308 (2004). URL http://dx.doi.org/10.1103/PhysRevB.70.155308.

[31] G. Salis, M. P. Walser, P. Altmann, C. Reichl, W. Wegscheider. *Dynamics of a localized spin excitation close to the spin-helix regime*. Phys. Rev. B, **89**, 045304 (2014). URL http://dx.doi.org/10.1103/PhysRevB.89.045304.

[32] M. M. Glazov, E. Y. Sherman. *Theory of spin noise in nanowires*. Phys. Rev. Lett., **107**, 156602 (2011). URL http://dx.doi.org/10.1103/PhysRevLett.107.156602.

[33] J. Schliemann, J. C. Egues, D. Loss. *Nonballistic spin-field-effect transistor*. Phys. Rev. Lett., **90**, 146801 (2003). URL http://dx.doi.org/10.1103/PhysRevLett.90.146801.

[34] B. A. Bernevig, J. Orenstein, S.-C. Zhang. *Exact SU(2) Symmetry and Persistent Spin Helix in a Spin-Orbit Coupled System*. Phys. Rev. Lett., **97**, 236601 (2006). URL http://dx.doi.org/10.1103/PhysRevLett.97.236601.

[35] J. D. Koralek, C. P. Weber, J. Orenstein, B. A. Bernevig, Shou-Cheng Zhang, S. Mack, D. D. Awschalom. *Emergence of the persistent spin helix in semiconductor quantum wells*. Nature, **458**, 610 (2009). URL http://www.nature.com/nature/journal/v458/n7238/abs/nature07871.html.

[36] M. Kohda, V. Lechner, Y. Kunihashi, T. Dollinger, P. Olbrich, C. Schönhuber, I. Caspers, V. V. Bel'kov, L. E. Golub, D. Weiss, K. Richter, J. Nitta, S. D. Ganichev. *Gate-controlled persistent spin helix state in (In,Ga)As quantum wells*. Phys. Rev. B, **86**, 081306 (2012). URL http://dx.doi.org/10.1103/PhysRevB.86.081306.

[37] M. P. Walser, C. Reichl, W. Wegscheider, G. Salis. *Direct mapping of the formation of a persistent spin helix*. Nat. Phys., **8**, 757 (2012). URL http://www.nature.com/nphys/journal/v8/n10/abs/nphys2383.html.

[38] J. Ishihara, Y. Ohno, H. Ohno. *Direct imaging of gate-controlled persistent spin helix state in a modulation-doped GaAs/AlGaAs quantum well*. Appl. Phys. Exp., **7**, 013001 (2014). URL http://stacks.iop.org/1882-0786/7/i=1/a=013001.

[39] K. Yoshizumi, A. Sasaki, M. Kohda, J. Nitta. *Gate-controlled switching between persistent and inverse persistent spin helix states*. Appl. Phys. Lett., **108**, 132402 (2016). URL http://dx.doi.org/10.1063/1.4944931.

[40] Y. Kunihashi, H. Sanada, H. Gotoh, K. Onomitsu, M. Kohda, J. Nitta, T. Sogawa. *Drift transport of helical spin coherence with tailored spin-orbit interactions*. Nat. Commun., **7**, 10722 (2016). URL http://www.nature.com/ncomms/2016/160308/ncomms10722/full/ncomms10722.html.

[41] M. Faraday. *Experimental Researches in Electricity. Nineteenth Series.* Phil. Trans. R. Soc. Lond., **136**, 1 (1846). URL http://rstl.royalsocietypublishing.org/content/136.toc.

[42] J. C. Maxwell. *A Dynamical Theory of the Electromagnetic Field.* Phil. Trans. R. Soc. Lond., **155**, 459 (1865). URL http://dx.doi.org/10.1098/rstl.1865.0008.

[43] W. Weber, R. Kohlrausch. *Ueber die Elektricitätsmenge, welche bei galvanischen Strömen durch den Querschnitt der Kette fliesst.* Annalen der Physik und Chemie, **99**, 10 (1856). URL http://gallica.bnf.fr/ark:/12148/bpt6k15184h.langDE.

[44] J. L. Foucault. *Détermination expérimentale de la vitesse de la lumiére: parallaxe du Soleil.* Comptes reduns. de l'Académie des sciences, **55**, 501 (1862).

[45] J. Kerr. *On rotation of the plane of polarization by reflection from the pole of a magnet.* Philosophic Magazine Series 5, **3**, 321 (1877).

[46] H. S. Bennett, E. A. Stern. *Faraday effect in solids.* Phys. Rev., **137**, A448 (1965). URL http://dx.doi.org/10.1103/PhysRev.137.A448.

[47] J. Halpern, B. Lax, Y. Nishina. *Quantum Theory of Interband Faraday and Voigt Effects.* Phys. Rev., **134**, A140 (1964). URL http://dx.doi.org/10.1103/PhysRev.134.A140.

[48] M. Cardona. *Electron Effective Masses of InAs and GaAs as a Function of Temperature and Doping.* Phys. Rev., **121**, 752 (1961). URL http://dx.doi.org/10.1103/PhysRev.121.752.

[49] T. H. Lee, H. Y. Fan. *Faraday rotation in p-type semiconductors.* Phys. Rev., **165**, 927 (1968). URL http://dx.doi.org/10.1103/PhysRev.165.927.

[50] H. J. Jiménez-González, R. L. Aggarwal, G. Favrot. *Infrared Faraday rotation of n -type InSb.* Phys. Rev. B, **49**, 4571 (1994). URL http://dx.doi.org/10.1103/PhysRevB.49.4571.

[51] H. Feil, C. Haas. *Magneto-Optical Kerr Effect, Enhanced by the Plasma Resonance of Charge Carriers.* Phys. Rev. Lett., **58**, 65 (1987). URL http://dx.doi.org/10.1103/PhysRevLett.58.65.

[52] R. L. Aggarwal, R. F. Lucey, D. P. Ryan Howard. *Faraday rotation in the 10 μm region in InSb at liquid helium temperature.* Appl. Phys. Lett., **53**, 2656 (1988). URL http://scitation.aip.org/content/aip/journal/apl/53/26/10.1063/1.100185.

[53] W. Cho, S. A. Kivelson. *Necessity of Time-Reversal Symmetry Breaking for the Polar Kerr Effect in Linear Response.* Phys. Rev. Lett., **116**, 093903 (2016). URL http://dx.doi.org/10.1103/PhysRevLett.116.093903.

[54] D. T. Pierce, F. Meier. *Photoemission of spin-polarized electrons from GaAs.* Phys. Rev. B, **13**, 5484 (1976). URL http://dx.doi.org/10.1103/PhysRevB.13.5484.

[55] G. Lampel. *Nuclear dynamic polarization by optical electronic saturation and optical pumping in semiconductors.* Phys. Rev. Lett., **20**, 491 (1968). URL http://dx.doi.org/10.1103/PhysRevLett.20.491.

[56] F. Meier, B. P. Zakharchenya. *Optical Orientation.* North-Holland Physics Publishing (1984).

[57] T. Elsaesser, J. Shah, L. Rota, P. Lugli. *Initial thermalization of photoexcited carriers in GaAs studied by femtosecond luminescence spectroscopy.* Phys. Rev. Lett., **66**, 1757 (1991). URL http://dx.doi.org/10.1103/PhysRevLett.66.1757.

[58] J. J. Baumberg, S. A. Crooker, D. D. Awschalom, N. Samarth, H. Luo, J. K. Furdyna. *Ultrafast Faraday spectroscopy in magnetic semiconductor quantum structures.* Phys. Rev. B, **50**, 7689 (1994). URL http://dx.doi.org/10.1103/PhysRevB.50.7689.

[59] A. V. Kimel, F. Bentivegna, V. N. Gridnev, V. V. Pavlov, R. V. Pisarev, T. Rasing. *Room-temperature ultrafast carrier and spin dynamics in GaAs probed by the photoinduced magneto-optical Kerr effect.* Phys. Rev. B, **63**, 235201 (2001). URL http://dx.doi.org/10.1103/PhysRevB.63.235201.

[60] A. V. Kimel, V. V. Pavlov, R. V. Pisarev, V. N. Gridnev, F. Bentivegna, T. Rasing. *Ultrafast dynamics of the photo-induced magneto-optical Kerr effect in CdTe at room temperature.* Phys. Rev. B, **62**, R10610 (2000). URL http://dx.doi.org/10.1103/PhysRevB.62.R10610.

[61] M. P. Walser. *Spin-orbit interaction and the persistent spin helix in two-dimensional electron gases.* Ph.D. thesis, Eidgenössische Technische Hochschule Zürich (2013).

[62] R. d. L. Kronig. *On the theory of dispersion of x-rays.* J. Opt. Soc. Am., **12**, 547 (1926).

[63] H. A. Kramers. *La diffusion de la lumiere par les atomes.* Atti del Congresso Internationale dei Fisici, Como, **2**, 545 (1927).

[64] J. M. Kikkawa, I. P. Smorchkova, N. Samarth, D. D. Awschalom. *Room-Temperature Spin Memory in Two-Dimensional Electron Gas*. Science, **277**, 1284 (1997). URL http://science.sciencemag.org/content/277/5330/1284.

[65] B. Baylac, X. Marie, T. Amand, M. Brousseau, J. Barrau, S. Y. *Hole spin relaxation in intrinsic quantum wells*. Surface Science, **326**, 161 (1995). URL http://www.sciencedirect.com/science/article/pii/0039602894007438.

[66] T. A. Kennedy, A. Shabaev, M. Scheibner, A. L. Efros, A. S. Bracker, D. Gammon. *Optical initialization and dynamics of spin in a remotely doped quantum well*. Phys. Rev. B, **73**, 045307 (2006). URL http://dx.doi.org/10.1103/PhysRevB.73.045307.

[67] L. Meier, G. Salis, I. Shorubalko, E. Gini, S. Schön, K. Ensslin. *Measurement of Rashba and Dresselhaus spin-orbit magnetic fields*. Nature Phys., **3**, 650 (2007). URL http://www.nature.com/nphys/journal/v3/n9/full/nphys675.html.

[68] M. Studer, M. P. Walser, S. Baer, H. Rusterholz, S. Schön, D. Schuh, W. Wegscheider, K. Ensslin, G. Salis. *Role of linear and cubic terms for drift-induced Dresselhaus spin-orbit splitting in a two-dimensional electron gas*. Phys. Rev. B, **82**, 235320 (2010). URL http://dx.doi.org/10.1103/PhysRevB.82.235320.

[69] M. P. Walser, U. Siegenthaler, V. Lechner, D. Schuh, S. D. Ganichev, W. Wegscheider, G. Salis. *Dependence of the Dresselhaus spin-orbit interaction on the quantum well width*. Phys. Rev. B, **86**, 195309 (2012). URL http://dx.doi.org/10.1103/PhysRevB.86.195309.

[70] Y. Kato, R. C. Myers, A. C. Gossard, D. D. Awschalom. *Coherent spin manipulation without magnetic fields in strained semiconductors*. Nature, **427**, 50 (2004). URL http://www.nature.com/nature/journal/v427/n6969/abs/nature02202.html.

[71] M. Kohda, P. Altmann, D. Schuh, S. D. Ganichev, W. Wegscheider, G. Salis. *All-optical evaluation of spin-orbit interaction based on diffusive spin motion in a two-dimensional electron gas*. Applied Physics Letters, **107**, 172402 (2015). URL http://scitation.aip.org/content/aip/journal/apl/107/17/10.1063/1.4934671.

[72] P. Altmann, M. Kohda, C. Reichl, W. Wegscheider, G. Salis. *Transition of a two-dimensional spin mode to a helical state by lateral confinement*. Phys.

Rev. B, **92**, 235304 (2015). URL http://dx.doi.org/10.1103/PhysRevB.92.235304.

[73] P. Altmann, M. P. Walser, C. Reichl, W. Wegscheider, G. Salis. *Suppressed decay of a laterally confined persistent spin helix*. Phys. Rev. B, **90**, 201306 (2014). URL http://dx.doi.org/10.1103/PhysRevB.90.201306.

[74] A. G. Mal'shukov, K. A. Chao. *Waveguide diffusion modes and slowdown of D'yakonov-Perel' spin relaxation in narrow two-dimensional semiconductor channels*. Phys. Rev. B, **61**, R2413 (2000). URL http://dx.doi.org/10.1103/PhysRevB.61.R2413.

[75] C.-H. Chang, J. Tsai, H.-F. Lo, A. G. Mal'shukov. *Semiclassical path integral approach for spin relaxations in narrow wires*. Phys. Rev. B, **79**, 125310 (2009). URL http://dx.doi.org/10.1103/PhysRevB.79.125310.

[76] A. A. Kiselev, K. W. Kim. *Progressive suppression of spin relaxation in two-dimensional channels of finite width*. Phys. Rev. B, **61**, 13115 (2000). URL http://dx.doi.org/10.1103/PhysRevB.61.13115.

[77] A. W. Holleitner, V. Sih, R. C. Myers, A. C. Gossard, D. D. Awschalom. *Suppression of Spin Relaxation in Submicron InGaAs Wires*. Phys. Rev. Lett., **97**, 036805 (2006). URL http://dx.doi.org/10.1103/PhysRevLett.97.036805.

[78] J. Wunderlich, B.-G. Park, A. C. Irvine, L. P. Zarbo, E. Rozkotov, P. Nemec, V. Novk, J. Sinova, T. Jungwirth. *Spin Hall Effect Transistor*. Science, **330**, 1801 (2010). URL http://dx.doi.org/10.1126/science.1195816.

[79] L. P. Zârbo, J. Sinova, I. Knezevic, J. Wunderlich, T. Jungwirth. *Modeling of diffusion of injected electron spins in spin-orbit coupled microchannels*. Phys. Rev. B, **82**, 205320 (2010). URL http://dx.doi.org/10.1103/PhysRevB.82.205320.

[80] J. Ishihara, M. Ono, Y. Ohno, H. Ohno. *A strong anisotropy of spin dephasing time of quasi-one dimensional electron gas in modulation-doped GaAs/AlGaAs wires*. Appl. Phys. Lett., **102**, 212402 (2013). URL http://scitation.aip.org/content/aip/journal/apl/102/21/10.1063/1.4807171.

[81] J. Ishihara, Y. Ohno, H. Ohno. *Direct mapping of photoexcited local spins in a modulation-doped GaAs/AlGaAs wires*. Jpn. J. Appl. Phys., **53**, 04EM04 (2014). URL http://stacks.iop.org/1347-4065/53/i=4S/a=04EM04.

[82] R. E. Williams. *Modern GaAs processing methods*. Artech House (1990).

[83] Y. Kunihashi, M. Kohda, J. Nitta. *Enhancement of Spin Lifetime in Gate-Fitted InGaAs Narrow Wires*. Phys. Rev. Lett., **102**, 226601 (2009). URL http://dx.doi.org/10.1103/PhysRevLett.102.226601.

[84] S. Kettemann. *Dimensional control of antilocalization and spin relaxation in quantum wires*. Phys. Rev. Lett., **98**, 176808 (2007). URL http://dx.doi.org/10.1103/PhysRevLett.98.176808.

[85] C.-H. Chang, A. G. Mal'shukov, K. A. Chao. *Spin relaxation dynamics of quasiclassical electrons in ballistic quantum dots with strong spin-orbit coupling*. Phys. Rev. B, **70**, 245309 (2004). URL http://dx.doi.org/10.1103/PhysRevB.70.245309.

[86] S. Z. Denega, T. Last, J. Liu, A. Slachter, P. J. Rizo, P. H. M. van Loosdrecht, B. J. van Wees, D. Reuter, A. D. Wieck, C. H. van der Wal. *Suppressed spin dephasing for two-dimensional and bulk electrons in GaAs wires due to engineered cancellation of spin-orbit interaction terms*. Phys. Rev. B, **81**, 153302 (2010). URL http://dx.doi.org/10.1103/PhysRevB.81.153302.

[87] J. Liu, T. Last, E. J. Koop, S. Denega, B. J. van Wees, C. H. van der Wal. *Spin-Dephasing Anisotropy for Electrons in a Diffusive Quasi-1D GaAs Wire*. J. Supercond. Nov. Magn., **23**, 11 (2009). ISSN 1557-1947. URL http://dx.doi.org/10.1007/s10948-009-0525-2.

[88] Y. Kunihashi, M. Kohda, J. Nitta. *Semiclassical approach for spin dephasing in a quasi-one-dimensional channel*. Phys. Rev. B, **85**, 035321 (2012). URL http://dx.doi.org/10.1103/PhysRevB.85.035321.

[89] P. Wenk, S. Kettemann. *Direction dependence of spin relaxation in confined two-dimensional systems*. Phys. Rev. B, **83**, 115301 (2011). URL http://dx.doi.org/10.1103/PhysRevB.83.115301.

[90] J. L. Cheng, M. W. Wu. *Spin diffusion/transport in n-type GaAs quantum wells*. J. Appl. Phys., **101**, 073702 (2007). URL http://scitation.aip.org/content/aip/journal/jap/101/7/10.1063/1.2717526.

[91] L. Yang, J. Orenstein, D.-H. Lee. *Random walk approach to spin dynamics in a two-dimensional electron gas with spin-orbit coupling*. Phys. Rev. B, **82**, 155324 (2010). URL http://dx.doi.org/10.1103/PhysRevB.82.155324.

[92] L. Yang, J. D. Koralek, J. Orenstein, D. R. Tibbetts, J. L. Reno, M. P. Lilly. *Coherent propagation of spin helices in a quantum-well confined electron gas*. Phys. Rev. Lett., **109**, 246603 (2012). URL http://dx.doi.org/10.1103/PhysRevLett.109.246603.

[93] P. Altmann, F. G. G. Hernandez, G. J. Ferreira, M. Kohda, C. Reichl, W. Wegscheider, G. Salis. *Current-Controlled Spin Precession of Quasistationary Electrons in a Cubic Spin-Orbit Field*. Phys. Rev. Lett., **116**, 196802 (2016). URL http://dx.doi.org/10.1103/PhysRevLett.116.196802.

[94] V. V. Bryksin, P. Kleinert. *Coupled spin-charge drift-diffusion approach for a two-dimensional electron gas with Rashba spin-orbit coupling*. Phys. Rev. B, **75**, 205317 (2007). URL http://dx.doi.org/10.1103/PhysRevB.75.205317.

[95] P. Kleinert, V. V. Bryksin. *Spin polarization in biased Rashba-Dresselhaus two-dimensional electron systems*. Phys. Rev. B, **76**, 205326 (2007). URL http://dx.doi.org/10.1103/PhysRevB.76.205326.

[96] R. Moriya, K. Sawano, Y. Hoshi, S. Masubuchi, Y. Shiraki, A. Wild, C. Neumann, G. Abstreiter, D. Bougeard, T. Koga, T. Machida. *Cubic Rashba Spin-Orbit Interaction of a Two-Dimensional Hole Gas in a Strained*-Ge/SiGe *Quantum Well*. Phys. Rev. Lett., **113**, 086601 (2014). URL http://dx.doi.org/10.1103/PhysRevLett.113.086601.

[97] R. Winkler, H. Noh, E. Tutuc, M. Shayegan. *Anomalous Rashba spin splitting in two-dimensional hole systems*. Phys. Rev. B, **65**, 155303 (2002). URL http://dx.doi.org/10.1103/PhysRevB.65.155303.

[98] G. M. Minkov, A. A. Sherstobitov, A. V. Germanenko, O. E. Rut, V. A. Larionova, B. N. Zvonkov. *Antilocalization and spin-orbit coupling in the hole gas in strained* GaAs/$In_xGa_{1-x}As$/GaAs *quantum well heterostructures*. Phys. Rev. B, **71**, 165312 (2005). URL http://dx.doi.org/10.1103/PhysRevB.71.165312.

[99] Y. H. Park, S.-H. Shin, J. D. Song, J. Chang, S. H. Han, H.-J. Choi, H. C. Koo. *Gate voltage control of the Rashba effect in a p-type GaSb quantum well and application in a complementary device* . Solid-State Electronics, **82**, 34 (2013). ISSN 0038-1101. URL http://www.sciencedirect.com/science/article/pii/S0038110113000294.

[100] H. Nakamura, T. Koga, T. Kimura. *Experimental Evidence of Cubic Rashba Effect in an Inversion-Symmetric Oxide*. Phys. Rev. Lett., **108**, 206601 (2012). URL http://dx.doi.org/10.1103/PhysRevLett.108.206601.

[101] M. Kepenekian, R. Robles, C. Katan, D. Sapori, L. Pedesseau, J. Even. *Rashba and Dresselhaus Effects in Hybrid Organic-Inorganic Perovskites: From Basics to Devices*. ACS Nano, **9**, 11557 (2015). URL http://dx.doi.org/10.1021/acsnano.5b04409.

[102] S. Datta, B. Das. *Electronic analog of the electro-optic modulator*. Appl. Phys. Lett., **56**, 665 (1990). URL http://scitation.aip.org/content/aip/journal/apl/56/7/10.1063/1.102730.

[103] P. Chuang, S.-C. Ho, L. W. Smith, F. Sfigakis, M. Pepper, C.-H. Chen, J.-C. Fan, J. P. Griffiths, I. Farrer, H. E. Beere, G. A. C. Jones, D. A. Ritchie, T.-M. Chen. *All-electric all-semiconductor spin field-effect transistors*. Nat. Nanotech., **10**, 35 (2014). URL http://www.nature.com/nnano/journal/v10/n1/full/nnano.2014.296.html.

[104] B. Behin-Aein, D. Datta, S. Sayeef, S. Datta. *Proposal for an all-spin logic device with built-in memory*. Nat. Nanotech., **5**, 266 (2010). URL http://www.nature.com/nnano/journal/v5/n4/abs/nnano.2010.31.html.

[105] D. E. Nikonov, G. I. Bourianoff, T. Ghani. *Proposal of a spin torque majority gate logic*. IEEE Electron Device Letters, **32**, 1128 (2011). ISSN 0741-3106. URL http://dx.doi.org/10.1109/LED.2011.2156379.

[106] M. E. Flatté, G. Vignale. *Unipolar spin diodes and transistors*. Appl. Phys. Lett., **78**, 1273 (2001). URL http://scitation.aip.org/content/aip/journal/apl/78/9/10.1063/1.1348317.

[107] J. Fabian, I. Žutić, S. Das Sarma. *Theory of spin-polarized bipolar transport in magnetic $p-n$ junctions*. Phys. Rev. B, **66**, 165301 (2002). URL http://dx.doi.org/10.1103/PhysRevB.66.165301.

[108] M. E. Flatté, Z. G. Yu, E. Johnston-Halperin, D. D. Awschalom. *Theory of semiconductor magnetic bipolar transistors*. Appl. Phys. Lett., **82**, 4740 (2003). URL http://scitation.aip.org/content/aip/journal/apl/82/26/10.1063/1.1586996.

[109] D. E. Nikonov, G. I. Bourianoff. *Spin gain transistor in ferromagnetic semiconductors-the semiconductor Bloch-equations approach*. IEEE Transactions on Nanotechnology, **4**, 206 (2005). ISSN 1536-125X. URL http://dx.doi.org/10.1109/TNANO.2004.837847.

[110] H. Dery, P. Dalal, L. Cywiński, L. J. Sham. *Spin-based logic in semiconductors for reconfigurable large-scale circuits*. Nature, **447**, 573 (2007). URL http://www.nature.com/nature/journal/v447/n7144/full/nature05833.html.

[111] C. Chappert, A. Fert, F. Nguyen van Dau. *The emergence of spin electronics in data storage*. Nat. Mat., **6**, 813 (2007). URL http://www.nature.com/nmat/journal/v6/n11/full/nmat2024.html.

[112] Y. Acremann, X. W. Yu, A. A. Tulapurkar, A. Scherz, V. Chembrolu, J. A. Katine, M. J. Carey, H. C. Siegmann, J. Sthr. *An amplifier concept for spintronics*. Appl. Phys. Lett., **93**, 102513 (2008). URL http://scitation.aip.org/content/aip/journal/apl/93/10/10.1063/1.2977964.

[113] S. Manipatruni, D. E. Nikonov, I. A. Young. *Material targets for scaling all-spin logic*. Phys. Rev. Applied, **5**, 014002 (2016). URL http://dx.doi.org/10.1103/PhysRevApplied.5.014002.

[114] E. Y. Vedmedenko, D. Altwein. *Topologically protected magnetic helix for all-spin-based applications*. Phys. Rev. Lett., **112**, 017206 (2014). URL http://dx.doi.org/10.1103/PhysRevLett.112.017206.

[115] B. Behin-Aein, A. Sarkar, S. Srinivasan, S. Datta. *Switching energy-delay of all spin logic devices*. Appl. Phys. Lett., **98**, 123510 (2011). URL http://scitation.aip.org/content/aip/journal/apl/98/12/10.1063/1.3567772.

[116] V. Calayir, D. E. Nikonov, S. Manipatruni, I. A. Young. *Static and clocked spintronic circuit design and simulation with performance analysis relative to cmos*. IEEE Transactions on Circuits and Systems I: Regular Papers, **61**, 393 (2014). ISSN 1549-8328. URL http://dx.doi.org/10.1109/TCSI.2013.2268375.

[117] P. Bonhomme, S. Manipatruni, R. M. Iraei, S. Rakheja, S. C. Chang, D. E. Nikonov, I. A. Young, A. Naeemi. *Circuit simulation of magnetization dynamics and spin transport*. IEEE Transactions on Electron Devices, **61**, 1553 (2014). ISSN 0018-9383. URL http://dx.doi.org/10.1109/TED.2014.2305987.

[118] S.-W. Jung, H.-W. Lee. *Spin polarization amplification within nonmagnetic semiconductors at room temperature*. Phys. Rev. B, **73**, 165302 (2006). URL http://dx.doi.org/10.1103/PhysRevB.73.165302.

[119] D. Saha, M. Holub, P. Bhattacharya. *Amplification of spin-current polarization*. Appl. Phys. Lett., **91**, 072513 (2007). URL http://scitation.aip.org/content/aip/journal/apl/91/7/10.1063/1.2772660.

[120] I. Žutić, J. Fabian, S. Das Sarma. *Spintronics: Fundamentals and applications*. Rev. Mod. Phys., **76**, 323 (2004). URL http://dx.doi.org/10.1103/RevModPhys.76.323.

[121] M. Oltscher, M. Ciorga, M. Utz, D. Schuh, D. Bougeard, D. Weiss. *Electrical Spin Injection into High Mobility 2D Systems*. Phys. Rev. Lett., **113**, 236602 (2014). URL http://dx.doi.org/10.1103/PhysRevLett.113.236602.

[122] D. S. Sivia, J. Skilling. *Data Analysis – A Bayesian Tutorial*. Oxford Science Publications (2011).

Acknowledgments

I thank Gian Salis for his guidance and supervision. He was always available for discussions, carefully read all manuscripts and his patient introduction into the measurement technique is not forgotten. Further, he performed the Monte-Carlo simulations. I want to thank him deeply for all of that and for what I have learned. Those three years were important and formative for my future life. Special thanks also go to Richard Warburton from the University of Basel, who kindly accepted to be my academic supervisor and who regularly made sure that I was on the right track. I always looked forward to our discussions and meetings. This PhD project put me into a position in which I could study some of the world's highest quality semiconductor quantum wells. The supply of this material is based on the collaboration with the group of Werner Wegscheider at ETHZ. I thank him and his team, primarily Christian Reichl, for enabling our work by sharing their wafers with us. In the laboratory, I profited tremendously from the work of my predecessor, Matthias Walser. He built with Gian Salis maybe the best scanning Kerr microscopy that one will find. Particularly for the construction of the cryostat insert I am very thankful. It was a pleasure for me to share the office and the laboratory with Makoto Kohda during his one-year sabbatical in our group. I am very happy he chose IBM, so we could get to know each other. For initiating a collaboration and taking the effort to come to Zurich, I want to thank Felix Hernandez. I am happy that our project was finished successfully and I want to thank also Gerson Ferreira to whom he introduced us. Also Yuansen Chen, who was a PostDoc in the group when I arrived, will be kept in good memory. I am very happy that our measurements of the spin helix in a (110) quantum well resulted in a publication. I wish him all the best for his own group in China. A special thank you goes to Daniel Riedel from the University of Basel who spent a mini-sabbatical with us exploring the possibilities to enhance the spatial resolution in our setup by the use of a solid immersion lens. To Rolf Allenspach I am grateful for always having an open door and giving advice when I needed one. I thank him also for promptly acting on my clearance requests and for proof-reading all manuscripts. Also Charlotte Bolliger's editing of our texts was strongly appreciated. I enjoyed the evening chats with Walter Riess and also to him I am thankful for that he quickly cleared my publication requests. In general, I appreciated the good atmosphere and I thank the whole team for creating a pleasurable environment. Technical assistance on e-beam lithography by Nikola Pascher and Emanuel Lörtscher, on general clean-room issues and in particular on the ICP-RIE by Ute Drechsler are greatly acknowledged. Finally, I thank the NCCR QSIT of the Swiss National Fond, as well as IBM for funding.

Publications

First author

Current-controlled spin precession of quasistationary electrons in a cubic spin-orbit field
P. Altmann, F. G. G. Hernandez, G. J. Ferreira, M. Kohda, C. Reichl, W. Wegscheider, G. Salis
Phys. Rev. Lett. **116**, 196802 (2016)

Transition of a two-dimensional spin mode to a helical state by lateral confinement
P. Altmann, M. Kohda, C. Reichl. W. Wegscheider, G. Salis
Phys. Rev. B **92**, 235304 (2015)

Suppressed decay of a laterally confined persistent spin helix
P. Altmann, M. P. Walser, C. Reichl, W. Wegscheider, G. Salis
Phys. Rev. B **90**, 201306(R) (2014)

Co-author

All-optical evaluation of spin-orbit interaction based on diffusive spin motion in a two-dimensional electron gas
M. Kohda, P. Altmann, D. Schuh, W. Wegscheider, S. Ganichev, G. Salis
Appl. Phys. Lett. **107**, 1724042 (2015)

Dynamics of a localized spin excitation close to the spin-helix regime
G. Salis, M. P. Walser, P. Altmann, C. Reichl, W. Wegscheider
Phys. Rev. B **89**, 045304 (2014)

Submitted

Spin drift and diffusion in one- and two-subband helical systems
G. J. Ferreira, F. G. G. Hernandez, P. Altmann, G. Salis
arXiv:1608.05437